UNIVERSITÉ DE MONTRÉAL

CONTRIBUTION TO THE DESIGN AND IMPLEMENTATION OF A MICROWAVE TOMOGRAPHY SYSTEM FOR BREAST CANCER DETECTION

ALVARO DIAZ BOLADO
DÉPARTEMENT DE GÉNIE ÉLECTRIQUE
ÉCOLE POLYTECHNIQUE DE MONTRÉAL

THÈSE PRÉSENTÉE EN VUE DE L'OBTENTION
DU DIPLÔME DE PHILOSOPHIÆ DOCTOR
(GÉNIE ÉLECTRIQUE)
DÉCEMBRE 2012

UNIVERSITÉ DE MONTRÉAL

ÉCOLE POLYTECHNIQUE DE MONTRÉAL

Cette thèse intitulée :

CONTRIBUTION TO THE DESIGN AND IMPLEMENTATION OF A MICROWAVE TOMOGRAPHY SYSTEM FOR BREAST CANCER DETECTION

présentée par : DIAZ BOLADO Alvaro
en vue de l'obtention du diplôme de : Philosophiæ Doctor
a été dûment acceptée par le jury d'examen constitué de :

M. GOUSSARD Yves, Ph.D., président
M. LAURIN Jean-Jacques, Ph.D., membre et directeur de recherche
M. LOVETRI Joe, Ph.D., membre
M. AKYEL Cevdet, Ph.D., membre

"*La paciencia es la madre de la ciencia*",
Sagesse populaire

ACKNOWLEDGEMENTS

In this section I would like to thank all the persons that helped me through this journey that took me far away from home and now ends up in the form of this thesis.

First of all, I would like to thank the members of the jury, Prof. Cevdet Akyel and Prof. Yves Goussard from Ecole Polytechnique de Montreal and Prof. Joe Lo Vetri from University of Manitoba for accepting reading this thesis and being part of this jury.

I would like to thank my director Prof. Jean-Jacques Laurin for giving me the opportunity to join his research group and for being my mentor during this thesis. His passion and ability to transmit his scientific knowledge, his attention to details, as well as, his human qualities have helped me through this path of becoming a researcher. I would also like to thank him for his availability and the fruitful discussions that solve all the experimental problems encountered during this work.

I would also like to to thank Dr. Bernard Duchêne and Prof. Jean-Charles Bolomey for the opportunity of carrying a four month research internship at the Laboratoire des Signaux et Systèmes in Supélec. Not to forget the always interesting scientific and non-scientific discussions with the rest of the people I met during my stay, Dr. Sandor Biliçz, Christophe Conessa, Dr. Nadine Joachimowicz, Dr. Alain Joisel, Dr. Marc Lambert and Prof. David Lesselier.

I would also like to thank all the staff from Poly-Grames research center at Ecole Polytechnique de Montreal, beginning by Ginette Desparois for her availability and support during my whole stay, continuing with Jean-Sebastien Decarie for his kindness, hard work and been always available for solving our computer problems and last but not least, Traian Antonescu, Steve Dubé, Jules Gaulthier and Maxime Thibault for his invaluable help during the different prototypes development, as well as, our always interesting discussions during lunch time.

Now I stand up, to express my special gratitude to two of my colleagues Dr. Paul-André Barrière and Dr. Hamidreza Memarzadeh Tehran, who in addition to the great times passed inside and outside Poly-Grames, have greatly contributed to the results of this thesis. I would also like to thank all my colleagues from Poly-Grames that I have known during my stay and that contributed to create a great work atmosphere, Tarek Djerafi, Maxime Daigle, Leandro Rufail, Hoda Nematollahi, Olivier Kramer, Shulav Avdikhari, Marc-André Joyal, Rachid el Hani, Patrick Deschênes, David Dousset and all the others that I forget but they are not less important.

Finalmente me gustaría agradecer a mi familia todo su cariño y comprensiòn y todas las

charlas a través de Internet en estos años que hicieron que no me sintiera demasiado lejos de casa. Un último pensamiento va para mi abuelo Pedro, que introdujo en mí la curiosidad por la electricidad y la propagación de ondas, seguro que allá donde esté estará orgulloso de este trabajo.

RÉSUMÉ

Cette thèse représente une contribution à la conception et mise en œuvre d'un système de tomographie micro-onde pour la détection du cancer du sein. La tomographie micro-onde est une technique d'imagerie donc le but est de reconstruire la permittivité et la conductivité d'un objet inconnu à partir des mesures du champ diffusé par l'objet. Cette technique a été utilisé dans une variété d'applications comme le control non-destructif, la géophysique et l'imagerie biomédicale. Dans cette thèse, l'emphase sera mise sur la détection du cancer du sein, où cette technique a reçu énormément d'attention dans les années précédentes.

Un système de tomographie micro-onde est normalement composé de deux parties séparées ; un système de mesures capable de fournir des mesures précises du champ diffusé et une série d'algorithmes capable de retrouver la distribution spatial de la permittivité et la conductivité de l'objet inconnu à partir des mesures du champ diffusé. Ce problème inverse est particulièrement difficile à résoudre, puisqu'il est non-linéaire et mal posé. Dans le but d'obtenir une bonne reconstruction de l'objet, il est nécessaire d'illuminer l'objet sous une série de conditions independantes, comme différentes positions d'antenne, des fréquences ou des polarisations. Dans cette thèse, l'emphase sera mise sur la conception d'une configuration d'illumination efficace qui essaie de maximiser la qualité des images reconstruites.

Après une revue de littérature, on observe que la plupart des systèmes de mesures partagent une configuration commune où les antennes sont placées sur une configuration cylindrique ou hémisphérique pour maximiser le confort de la patiente. D'un autre coté, la méthode la plus populaire pour le dépistage du cancer du sein est la mammographie, où on utilise une image à rayons X du sein compressé en deux projections. En prenant compte de ce fait, on propose deux configurations alternatives basées sur la compression du sein, les configurations caméra et guide d'onde. L'hypothèse derrière cette proposition est que la compression du sein permet de placer les capteurs très près de ce dernier donc il est possible de mesurer la composante évanescente du champ diffusé, ce qui pourrait permettre l'amélioration de la qualité des images reconstruites. Afin de prouver cette hypothèse, une étude rigoureuse des configurations proposées et sa comparaison avec une configuration classique de tomographie circulaire est réalisée. Grace à cette étude on détermine les conditions qui permettent d'améliorer les images reconstruites.

Le placement des capteurs très proche de l'objet sous test représente un défi pour une mesure précise des champs diffusés, puisque le capteur lui-même peut perturber le signal à mesurer. Pour cette raison, une version améliorée d'une sonde de mesure en champ proche basé sur la technique de diffusion modulée est conçue et validée. La sonde est utilisée pour la mise

en œuvre de la configuration guide d'onde proposée. Un réseau d'antennes est développé pour l'excitation de différents modes avec différentes polarisations à l'intérieur du guide d'onde. La sonde modulée est utilisée pour la mesure du champ diffuse produit par des objets cylindriques placés à l'intérieur du guide et un bon accord entre les résultats mesurés et simulés est obtenu.

Finalement, des images quantitatives des objets allongés pour les deux configurations sont présentées. Une formulation 2D TM est utilisée pour la solution du problème inverse. Premièrement, pour le cas de la configuration guide d'onde, des images quantitatives d'un cylindre placé à différents endroits à l'intérieur du guide sont présentées. Deuxièmement, l'effet de la compression du sein sur un fantôme simplifié est étudié pour une configuration caméra. Dans ce cas, deux fantômes qui représentent deux niveaux de compression sont fabriqués et les résultats sont comparés au niveau de la qualité des mesures et des images quantitatives reconstruites. Ces résultats permettent de prouver expérimentalement l'amélioration due à l'effet de la compression, puisque il y a une amélioration qualitative et quantitative des images obtenues pour un plus grand niveau de compression. Finalement, la qualité des images reconstruites est fortement affectée par la construction du fantôme et par la quantité limitée d'information dans la configuration caméra où seulement la transmission à travers l'objet est disponible

ABSTRACT

This thesis represents a contribution to the design and implementation of a microwave tomography system applied to breast cancer detection. Microwave tomography is an imaging technique that aims to reconstruct the permittivity and conductivity of an unknown object from measurements of its scattered field. This technique has been used in a variety of applications such as non-destructive testing, geophysical surveys and biomedical imaging. Here, we will concentrate in the breast cancer detection, where this technique have received a lot of attention in the recent years.

A microwave tomography system usually involves two separate parts, a measurement system capable of performing accurate measurements of the scattered field and a set of algorithms for solving the inverse problem of retrieving the permittivity and conductivity spatial distribution of the unknown object from the scattered field measurements. This inverse problem is particularly difficult to solve, since it is non-linear and ill posed. In order to achieve a good reconstruction of the object, we need to illuminate it under several independent conditions, such as different antenna positions, frequencies or polarizations. In this thesis, we concentrate in the design of an efficient illumination configuration that tries to maximize the quality of the reconstructed images.

After a litterature review, it is observed that most of the proposed measurement systems share a common configuration, where in order to maximize the comfort of the patient, the antennas are arranged in a cylindrical or hemi-spherical configuration. On the other hand, the most popular method for breast cancer detection is mammography, where a X-ray image of the compressed breast at two different projections is performed. Taking this into account, two alternative configurations based on a compression of the breast are proposed, the camera and waveguide configurations. The main hypothesis behind this proposition is that a compression of the breast will allow to place the receivers very close to the breast where it is possible to measure the evanescent component of the scattered field and thus allow an enhancement of the quality of the reconstructed images. In order to prove this hypothesis, a rigorous study of the proposed configurations against a classical circular tomography setup is performed, and we determine under what conditions the reconstructed images can be enhanced.

Next, the placement of the receiving antennas very close to the object under test, poses some challenges for an accurate measurement of the scattered fields, since the measurement probe itself can distort the quantity to be measured. For this purpose, an enhanced version of a previously designed near-field probe based on the modulated scattering technique is designed and validated. The probe is then used in the practical implementation of the

proposed waveguide configuration. An array of antennas is designed to excite the different modes of different polarizations in the waveguide, and the modulated probe is used to measure the scattered field produced by cylindrical objects placed inside the waveguide, where a good agreement between the measured and simulated results is obtained.

Finally, quantitative images of elongated objects in the two proposed configurations, using a 2D TM formulation for the solution of the inverse scattering problem are presented. First, for the case of the waveguide configuration, quantitative images of a cylinder at different positions inside the waveguide are presented. Second, the effect of breast compression in a simplified phantom is studied for the camera configuration. In this case, two phantoms representing two different levels of compression are constructed and the results are compared in terms of the quality of the measurements and quantitative reconstructed images. These results are an experimental proof of the image enhancement due to compression, because both a qualitative and quantitative enhancement of the obtained image quality are obtained for the higher level of compression. Finally, the quality of the reconstructed images is affected by the phantom structure and the limited available information in the camera configuration where only transmission through the object is available.

TABLE OF CONTENTS

LIST OF TABLES

LIST OF FIGURES

LIST OF ACRONYMS

2D	Two Dimensional
3D	Three Dimensional
AMI	Active Microwave Imaging
CG	Conjugate Gradien
CMI	Confocal Microwave Imaging
CSI	Contrast Source Inversion
CT	Computerized Tomography
DBI	Distorted Born Iterative method
DC	Direct Current
DW	Dielectric Waveguide
EFIE	Electric Field Integral Equation
E-field	Electric Field
EM field	Electromagnetic field
FDFD	Finite Differences Frequency Domain
GF	Green's Function
LIA	Lock-in-Amplifier
LNA	Low Noise Amplifier
MHMIC	Miniature Hybrid Microwave Integrated Circuit
MoM	Method of Moments
MRI	Magnetic Resonance Imaging
MSE	Mean Square Error
MR-CSI	Multiplicative Regularization Contrast Source Inversion
MST	Modulated Scattering Technique
MT	Microwave Tomography
NF	Near-Field
OMS	Optically Modulated Scatterer
OUT	Object Under Test
RF	Radio-Frequency
Rx	Receiver
SMA	SubMiniature version A connector
SNR	Signal to Noise Ratio
SVD	Singular Value Decomposition
SWL	Surface Wave Launcher

TE	Transverse Electrical
TM	Transverse Magnetical
Tx	Transmitter
VNA	Vector Network Analyzer

CHAPTER 1

Introduction

1.1 Breast Cancer Detection

Breast cancer is an important health problem. This type of cancer is one of the most prevalent form of cancer in Canada, and statistics suggests that one of every nine women is expected to develop a breast cancer and one in 29 will die because of it (CCS (2011)). The current procedure for early stage breast cancer detection includes three steps : a screening mammography, a detection mammography and a biopsy. In the screening mammography, X-ray images of the compressed breast in two orthogonal planes are taken, that is, Craniocaudal (head to toe) and Medio Lateral Oblique (lateral side view). An illustration of a mammography test configuration can be seen in Figure 1.1. It is usually recommended to have a mammography screening every two years for women between 40 and 70 years old or, women considered to have a high risk of developing a breast cancer (NCRP (2004)). In the case of a suspicious result in the screening mammography, the patient is called for a detection mammography. In this case, a more exhaustive study is done, including X ray images taken from different angles or focusing in suspicious zones. The study can be completed using alternative modalities such as ultrasound imaging, or making a biopsy of the potential cancerous tissue to be examined by a pathologist (NCRP (2004)). However this procedure presents some drawbacks (Fear *et al.* (2002) ; Fear *et al.* (2003)) such as :

- The high rate of false positives, which require further testing and generates anxiety to the patients ;
- The high rate of false negatives, which represents missing up to 15% of breast tumors ;
- Difficulty in imaging dense breasts, which can represent up to 25% of the population ;
- Usage of ionizing radiation and discomfort produced by the strong breast compression ;

Other imaging methods have been proposed as an alternative to mammography and are currently used in clinic (NCRP (2004)). Among the different techniques we can cite, ultrasound, which is used as a tool for differentiation between cysts and solid masses or evaluate complications in patients with breast implants. However its use as a screening technique has been found to be less effective than mammography, except for the case of patients with dense breasts (NCRP (2004)). Thermography and trans illumination, have been also tested as screening and differentiation tools, however screening mammography has shown a superior performance to these techniques. Computed tomography (CT), magnetic resonance and posi-

Figure 1.1 Representation of a mammography in craniocaudal view. Image source Wikipedia.

tron emission tomography scans present very interesting properties as imaging tools and have been applied to breast imaging. Their ability to create 3D images, as a succession of planar images or a whole volumetric reconstruction is a great advantage compared to mammography where the images represent the integration of the X-ray attenuation through the breast. In all the cases, the procedure requires the use of a contrast agent in order to enhance the quality of the obtained images (NCRP (2004)). The need for these contrast agents, combined with the high cost of these techniques and the higher radiation dose in the case of a CT scan, make them not the most suitable techniques for large campaigns of preventive breast screening. These facts, have motivated a lot of research efforts for finding new alternative imaging techniques.

To date, a great number of techniques have been investigated, among these alternatives we can cite electrical impedance tomography (Choi *et al.* (2007); Barber et Brown (1984); Adler et Guardo (1996)), diffuse optical tomography (Fang *et al.* (2009); Boas *et al.* (2001); Soubret *et al.* (2005)), elastography (Sinkus *et al.* (2008); Parker *et al.* (1996); Fatemi *et al.* (2003)) and active microwave imaging (Fear *et al.* (2003); Craddock *et al.* (2006); Grzegorczyk *et al.* (2012)). All of them take advantage of physical parameters that have different values from

normal and malignant tissues.

1.2 Microwave Imaging

1.2.1 Classification of Microwave Imaging modalities

Microwave imaging is a technique to obtain an image of an unknown object under test (OUT) or scene using electromagnetic radiation in the RF/Microwave frequency regime. It can be divided in three types : passive, hybrid and active microwave imaging (AMI). In passive microwave imaging a radiometer is used to detect the different temperature regions in an OUT (Bardati et Iudicello (2008); Abdul-Razzak *et al.* (1987); Carr (1989)). Hybrid techniques normally use a series of very short, high powered microwave pulses that heat certain parts of the OUT, in this process mechanical expansion inside the OUT generates acoustic waves that are detected using an ultrasound transducer (Xu et Wang (2002, 2003)). Finally, in AMI the OUT is illuminated using a series of transmitting antennas and the response of the object (scattered field) is collected at the same or different positions.

A general scheme of an AMI system is depicted in Figure 1.2. It can be seen that the OUT is illuminated using a series of independent sources (identified as Tx in the picture). The raw data are then captured at different positions surrounding the object (positions identified with Rx antennas in the picture) and finally a series of algorithms are used to create an image of the object. The ability of microwave radiation to penetrate into dielectric materials make it appropriate for a lot of applications. For instance, it has been extensively used in civil and industrial engineering (Kim *et al.* (2003)), non-destructive testing of materials (Ghasr *et al.* (2008)), geophysical exploration (Tarnus *et al.* (2004)) and biomedical engineering (Meaney *et al.* (1998b)).

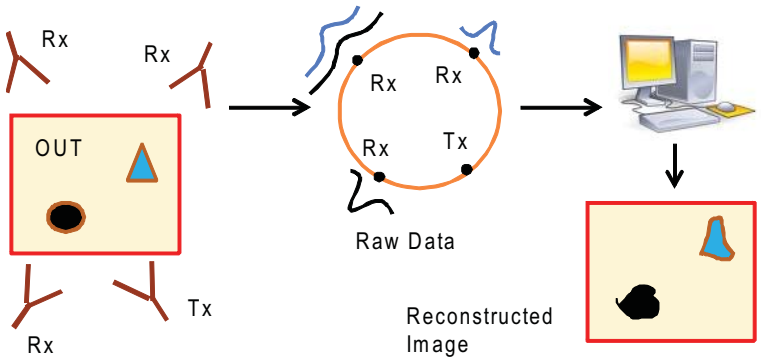

Figure 1.2 General scheme of an active microwave imaging system.

There are many different implementations of AMI that can generally be classified into

qualitative or *quantitative* techniques. Qualitative techniques aim to obtain a reconstruction of the shape of significant scatterers inside the object. On the other hand, quantitative techniques aim at reconstructing the spatial distribution of the complex permittivity of a region where the OUT is present. This approach allows both to have information about the shape and electrical characteristics of the object at the expense of solving a more complicated inverse problem.

1.2.2 Active Microwave Imaging for Breast Cancer Detection

Based on the potential of taking advantage of the contrast in permittivity and conductivity between normal and cancerous breast tissues, AMI has emerged as an interesting alternative or complement to mammography (Fear *et al.* (2002)). Different implementations of AMI for breast cancer detection have been proposed, which can be again classified into qualitative and quantitative techniques. Among the qualitative techniques we can cite microwave holography (Amineh *et al.* (2011b)) and confocal microwave imaging (CMI). CMI has generated a lot of attention due to the apparently ease of implementation and good reconstructed results (Fear *et al.* (2002)).

CMI consists in illuminating the OUT with a series of broadband pulses. The reflected signals are collected and then combined using a delay and sum algorithm to create an image of significant scatterers present inside the OUT. However, this technique presents some major difficulties, such as the strong reflections from the skin and the need to estimate the pulse velocity inside the heterogeneous breast to apply the simple reconstruction algorithm (Sill et Fear (2005) ;Williams *et al.* (2011) ;Winters *et al.* (2006)). On the other hand, microwave tomography (MT) is used to estimate the complex permittivity distribution inside the OUT, by solving an inverse scattering problem. In this case, the OUT is illuminated under several different conditions and the scattered field produced by the OUT is measured at different locations. In the particular case of breast cancer detection, a full 3D reconstruction of the breast volume can have a prohibitive computational cost, however recent developments have shown that it is possible to obtain 3D images of a patient's breast in under 20 minutes (Grzegorczyk *et al.* (2012)). Moreover, besides the inherent difficulties of this technique, the inexpensive cost of the microwave equipment, compared to other imaging techniques and the additional information provided by MT make it an important potential candidate as a breast screening tool.

1.3 Thesis

1.3.1 Thesis Justification and Previous work

This thesis is part of a research effort on microwave tomography for breast cancer detection at Ecole Polytechnique de Montreal. The objective of the project is to establish the basis for constructing a clinical prototype using this technique. Previous work on this topic included two MASc thesis (Truchetti (2005)) and (Omrane (2005)) and two PhD thesis (Barriere (2008)) and (Memarzadeh-Tehran (2010)). In (Omrane *et al.* (2011)), MT technique is applied to the characterization of dielectric plates, and very good results were obtained from experimental results. In (Truchetti (2005)), a preliminary study for the implementation of a MT system for breast cancer detection was done. More recently, work in (Barriere (2008)) studied the implementation of fast algorithms for the solution of the inverse problem arising in MT leading to a significant advancement in this field. Finally in (Memarzadeh-Tehran (2010)), the implementation of a near-field measurement system based on the modulated scattering technique (MST) was studied and very good measurement results were obtained.

From this preliminary work, and after a review of the state-of-the-art, which will be detailed in the next chapter, it was identified that most of the previous work in MT was concentrated in developing prototypes that all share a common configuration, without examining other alternatives that could improve the quality of the reconstructed images. From this fact, the objectives of this work were the study of different configurations for the MT measurement system applied to breast cancer detection, the implementation of transmitting antennas for illuminating the test fixture and the experimental validation of the proposed configurations using phantoms.

1.3.2 Thesis Structure

This thesis is divided in the following chapters :

- **Chapter 2** is a literature review of the previous work in the field of Microwave Imaging applied to breast cancer detection.
- **Chapter 3** includes a rigorous study of different configurations for the MT measurement system based on breast compression. The different configurations are compared to a classical MT system without breast compression.
- **Chapter 4** presents a developed probe based on the MST and its application in the practical implementation of a waveguide configuration for the MT problem.
- **Chapter 5** includes the experimental imaging results on the different MT configurations, as well as, the developed phantoms and calibration techniques used in the process.

– **Chapter 6** includes the conclusions of this study and proposes directions for future work.

CHAPTER 2

Literature review

2.1 Scattering of electromagnetic waves by biological bodies

2.1.1 Formulation based on the Electric Field Integral Equation (EFIE)

Microwave Tomography (MT) is based in the phenomena of electromagnetic scattering. An object illuminated by an electromagnetic wave will re-radiate or *scatter* part of this energy. The electromagnetic field in presence of the object is the sum of incident and scattered fields :

$$\mathbf{E} = \mathbf{E_{inc}} + \mathbf{E_s} \tag{2.1}$$

$$\mathbf{H} = \mathbf{H_{inc}} + \mathbf{H_s} \tag{2.2}$$

where a harmonic time dependence, $\mathcal{E}(\mathbf{r}, t) = \Re[\mathbf{E}(\mathbf{r})e^{j\omega t}]$, is assumed through this chapter.

The problem of electromagnetic scattering by a dielectric object can be modeled using the volume equivalence theorem (Balanis (1989)). This theorem states that the scattered field produced by the presence of an object, can be generated replacing the object by a set of equivalent electric and magnetic currents. The general configuration shown in figure 2.1 is assumed and the biological media is supposed to be non-magnetic ($\mu = \mu_0$). Taking into account these two assumptions, the equivalent currents generated inside the material are equal to :

$$\mathbf{J_{eq}}(\mathbf{r}) = j\omega\varepsilon_b\chi(\mathbf{r})\mathbf{E}(\mathbf{r}) \tag{2.3}$$

Where $\omega = 2\pi f$ is the angular frequency, ε_b is the permittivity of the background media,$\mathbf{E}$ is the total field inside the object and χ is the contrast function, which is defined as the normalized difference between the electrical properties of the object and those of the background media :

$$\chi(\mathbf{r}) = \frac{\varepsilon(\mathbf{r}) - \varepsilon_b}{\varepsilon_b} \tag{2.4}$$

The electrical permittivity of a biological body is complex and equal to :

$$\varepsilon = \varepsilon^{'} - j\varepsilon^{''} = \varepsilon_0 \left(\varepsilon_r - j\frac{\sigma_{eff}}{\omega\varepsilon_0} \right) \tag{2.5}$$

where σ_{eff} is an effective conductivity taking in consideration all the loss mechanisms in the dielectric material and ε_r is the real part of the relative permittivity.

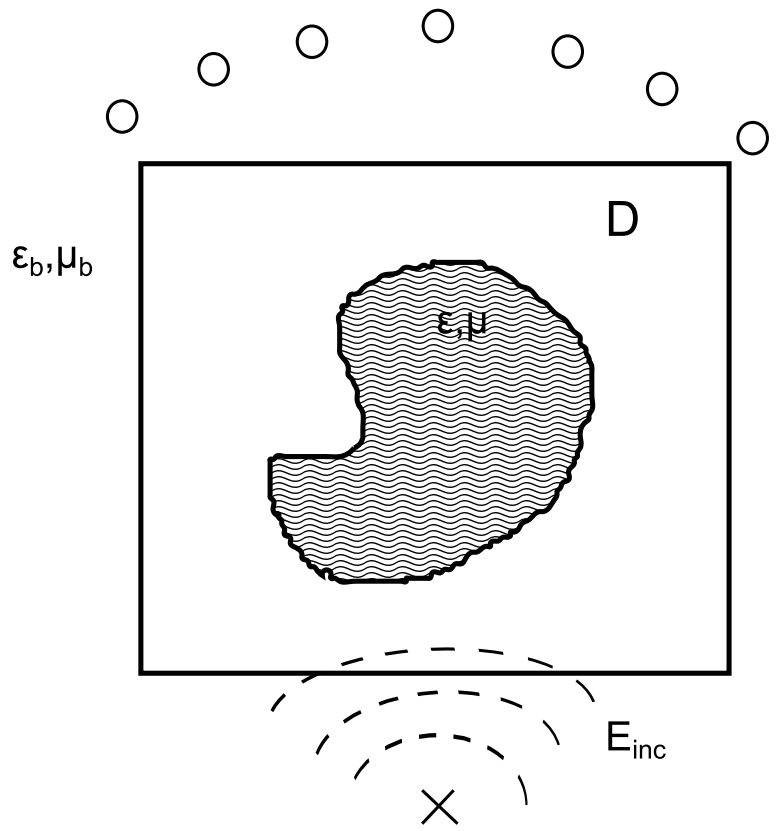

Figure 2.1 General geometry for a scattering, where the object is illuminated by one transmitting source (Symbol X) and the scattered field measured at a series of receivers positions (Symbol O).

The scattered field can then be computed from the equivalent currents ($\mathbf{J_{eq}}$) using the procedure described in (Balanis (1989)) :

$$\mathbf{E^s}(\mathbf{r}) = (k_b^2 + \nabla\nabla\cdot) \int_D \chi(\mathbf{r}')\mathbf{E}(\mathbf{r}')G(\mathbf{r},\mathbf{r}')dr' \tag{2.6}$$

where $k_b = \omega\sqrt{\mu_0\epsilon_b}$, D is the test volume which completely encloses the region of interest and $G(\mathbf{r},\mathbf{r}')$ is the Green's function for the background media. This Green's function is the solution to the wave equation for a point source, in the case of an homogeneous background, it can be expressed as :

$$G(\mathbf{r},\mathbf{r}') = \frac{1}{4\pi}\frac{e^{-jk_b|\mathbf{r}-\mathbf{r}'|}}{|\mathbf{r}-\mathbf{r}'|} \tag{2.7}$$

Equation 2.6 is the well known EFIE for computing the scattered field by a dielectric

body. In this case, the scattered field is a vectorial quantity and solving this equation for χ is not trivial. An interesting simplification happens when a 2D case is considered, i.e. assuming that the OUT is infinite and uniform along a given direction, for a uniform excitation along the infinite axis of the object. In that situation, two different problems can be faced depending on the orientation of the incident electromagnetic field. When the electric field polarization is perpendicular to the infinite dimension of the object, the problem is said to be transverse electric (TE), in that case we reduce the complexity from 3D to 2D, however the problem remains vectorial since two components of the electric field still exists. On the other hand, when the electric field is polarized parallel to the infinite dimension of the object the problem is denoted as transverse magnetic (TM) and we have a scalar problem. The gradient divergence term ($\nabla\nabla\cdot$) in equation 2.6 vanishes and the EFIE equation simply becomes :

$$E^s(\mathbf{r}) = k_b^2 \int_D \chi(\mathbf{r}')E(\mathbf{r}')G_{2D}(\mathbf{r},\mathbf{r}')dr' \tag{2.8}$$

Where in this case, the Green function now is the solution to the wave equation for an infinite current source :

$$G_{2D}(\mathbf{r},\mathbf{r}') = \frac{j}{4}H_0^{(2)}(k_b|\mathbf{r}-\mathbf{r}'|) \tag{2.9}$$

2.1.2 Discretization of the EFIE

The calculation of the scattered field produced by an arbitrary object generally requires spatial discretization of equation 2.6 or 2.8 over D. Analytical solution for some canonical targets is possible (Pastorino (2010)), but for arbitrary geometries this equation has to be discretized and solved using a suitable numerical method. A lot of different numerical methods are available for the solution of scattering problems, among them we can cite the Finite Element Method (FEM) (Chatterjee *et al.* (1998)), the Finite Differences both in time domain (FDTD) (Taflove et Hagness (2005)) and in frequency domain (FDFD) (Dong *et al.* (2007)) or the Method of Moments (MoM) (Harrington (1968)).

The MoM is generally preferred due to the efficiency of the method. The scattered field at any point of the solution domain can be calculated from only the discretization of the region of interest (region D referring to figure 2.1) provided the Green's function of the background media is known. When an homogeneous media is present, expressions 2.7 to 2.9 can be used to compute the scattered field. However for the case of an inhomogeneous media, the procedure is more complicated and requires some cumbersome computations (Chew (1999); Michalski et Mosig (1997)).

For a 2D TM case, the discretization of the EFIE using the MoM is quite straightforward.

The objective is to compute the scattered field at a series of receiver positions, as it can be seen in figure 2.1. The scattered field can be computed using equation 2.8, provided the total field inside the domain D is known. In order to compute it, an auxiliary equation is needed, for this purpose we will use equation 2.1. Now we have a system of equations to compute the scattered field at the required positions $\mathbf{r_k}$:

$$\mathbf{E^s}(\mathbf{r_k}) = k_b^2 \int_D \chi(\mathbf{r}')\mathbf{E}(\mathbf{r}')G(\mathbf{r_k}, \mathbf{r}')dr' \tag{2.10}$$

$$\mathbf{E}(\mathbf{r}) = \mathbf{E^{inc}} + k_b^2 \int_D \chi(\mathbf{r}')\mathbf{E}(\mathbf{r}')G(\mathbf{r}, \mathbf{r}')dr' \tag{2.11}$$

where equation 2.10 is an integral equation of first kind and 2.11 is an integral equation of second kind.

First, the region of interest is divided in n small cells and both the electric field and the contrast are assumed constant in each cell. The implementation of the MoM technique requires to expand the unknowns in a set of basis functions. A simple choice is to use pulse basis functions and the point matching technique which involves the use of delta-dirac functions as test functions. Using this procedure, the discretized version of equations 2.10 and 2.11 is now :

$$\mathbf{E^s} = \mathbf{G_o}\mathbf{X}\mathbf{E} \tag{2.12}$$

$$\mathbf{E} = \mathbf{E^{inc}} + \mathbf{G_c}\mathbf{X}\mathbf{E} \tag{2.13}$$

In this system of equations we have :
- $\mathbf{E^s}$, a vector containing the scattered field values at the N measurement points ;
- $\mathbf{E^{inc}}$, a vector containing the incident field values at the n discretization points ;
- $\mathbf{E}$, a vector containing the total field values at the n discretization points ;
- $\mathbf{X}$, a diagonal matrix containing the contrast at the n discretization points ;
- $\mathbf{G_o}$ and $\mathbf{G_c}$, two matrices of size $N \times n$ and $n \times n$ respectively ;

The matrices $\mathbf{G_o}$ and $\mathbf{G_c}$ have to be computed numerically, integrating the Green's function $G_{uv} = k_b^2 \int_i G(\mathbf{r}, \mathbf{r}')dr'$, where i refers to the i-th discretization cell in the region D. A lot of different techniques exists in the literature to perform numerical integration (Press *et al.* (1988)). However an efficient implementation can be obtained following the development proposed in (Richmond (1965)). The integral on the rectangular or square cells is approximated by the integral of circular cells of the same area, which has an analytical expression :

$$G_{uv} = \frac{jk_b^2}{4}\int_u H_0^{(2)}(k_b|\mathbf{r_u}-\mathbf{r_v}|)dr' = \begin{cases}(j/2)[\pi k_b a H_1^{(2)}(k_b a)], & \text{if } u = v\\ (j\pi k_b a/2)J_1(k_b a)H_0^{(2)}(k_b|\mathbf{r_u}-\mathbf{r_v}|), & \text{if } u \neq v\end{cases} \quad (2.14)$$

Where a_u is the equivalent radius of the $u-th$ cell, $a = \sqrt{\Delta/\pi}$, where Δ is the size of the discretization cell on a cartesian square meshing. This discretization is quite simple but it gives very good results and it is widely used in the microwave imaging literature. Other discretization techniques are possible, depending on the choice of the basis and test functions for the MoM implementations. In a 3D or 2D TE cases, discretization is more difficult since we have to take into account the gradient divergence term in 2.6. A detailed derivation of this more complicated cases can be found in (Zwamborn (1991); Pastorino (2010)).

2.2 Breast tissue characterization

2.2.1 Electrical properties of breast constituent tissues

The major challenge in characterizing breast tissue is its heterogeneity. Human breast is composed of several different types of tissue, an illustration of the breast anatomy can be seen in figure 2.2. However, for electrical characterization purposes, we will consider that the breast is composed of skin, muscle, fat tissue and glandular or fibroconnective tissue.

A complete characterization of the dielectric properties of several tissue types (including dry and wet skin as well as muscle) was performed and presented in a series of articles (Gabriel *et al.* (1996a,b,c)). In these papers, the dielectric properties of 17 tissue types are fully analyzed using an open-ended coaxial probe, in the frequency range 10Hz-20GHz. These values are commonly used in the interaction of electromagnetic fields and human body and are found in the material database of commercial electromagnetic codes such as CST Microwave Studio (CST (2011)).

Breast tissue characterization has been an active field of research. Previous studies using ex-vivo measurements suggested the existence of a large contrast between normal and malignant tissues for the case of breast cancer, compared to other organs such as colon, kidney and lung (Joines *et al.* (1994)). However, further studies using in vivo measurements (Meaney *et al.* (2000)), showed that this contrast was smaller than originally expected. The most complete available study is a joint research effort from the University of Calgary and the University of Wisconsin-Madison (Lazebnik *et al.* (2007c,b)). The first paper focuses on the analysis of normal breast tissue samples obtained from reduction surgeries and the second paper, considers normal, malignant and benign tissue samples obtained from cancer surgeries.

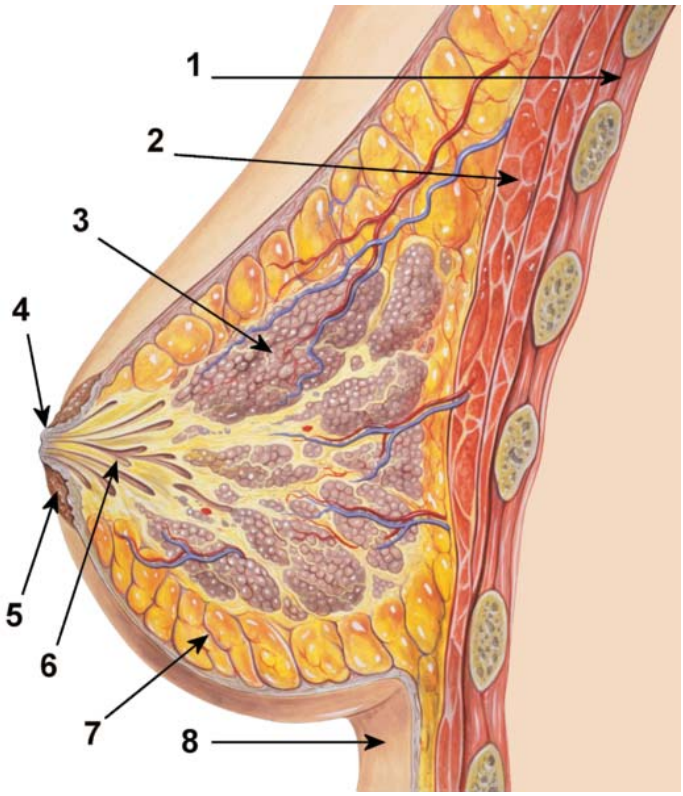

Figure 2.2 Breast tissue structure. 1-Chest Wall. 2-Pectorals muscles. 3-Lobules. 4-Nipple. 5-Areola. 6-Duct. 7-Fat tissue. 8-Skin. Image obtained from Wikipedia.

Normal breast tissue is divided in three categories in this study. These categories are defined based on the percentage adipose tissue content (Group I : 0-30%, Group II : 30-85%, Group III : 85-100%) in the measured sample, as determined by a pathologist. Whenever possible, several tissue types of the same patient were measured. Normal, benign and malignant tissue samples were also obtained from cancer surgeries. The number of benign tissue samples was not sufficient to make a fair comparison with the other groups and it was not fully analyzed. However, their dielectric properties were found to be similar to those of the low-adipose-content group (group I).

Measurements of the breast tissue were done in the frequency range 0.5-20 GHz. A precision open-ended coaxial probe was used for the measurement. The probe was custom designed for this particular application, and it is described in (Popovic *et al.* (2005)). The insertion point of the probe tip was marked with ink, and a 2D section was performed at this point in order to perform a histological analysis in order to determine the tissue group that the sample belongs to.

The measured data are then fitted to a single pole Cole-Cole model. This provided a good fit in the 0.5-20 GHz range. The Cole-Cole one pole model expression is :

$$\varepsilon^*(\omega) = \varepsilon^{'}(\omega) - j\varepsilon^{''}(\omega) = \varepsilon_\infty + \frac{\Delta\varepsilon}{1 + (j\omega\tau)^{1-\alpha}} + \frac{\sigma_s}{j\omega\varepsilon_o} \tag{2.15}$$

Where ω is the angular frequency, $\varepsilon^{'}(\omega)$ is the frequency-dependent dielectric constant, $\varepsilon^{''}(\omega)$ is the frequency-dependent dielectric loss (which can be converted into the effective conductivity $\sigma_{eff}(\omega) = \omega\varepsilon_o\varepsilon^{''}(\omega)$) and ε_∞, $\Delta\varepsilon$, τ, σ_s and α are the Cole-Cole parameters which are estimated from the experimental data. The complex permitivitties of both normal and malignant breast tissue are plotted in figure 2.3

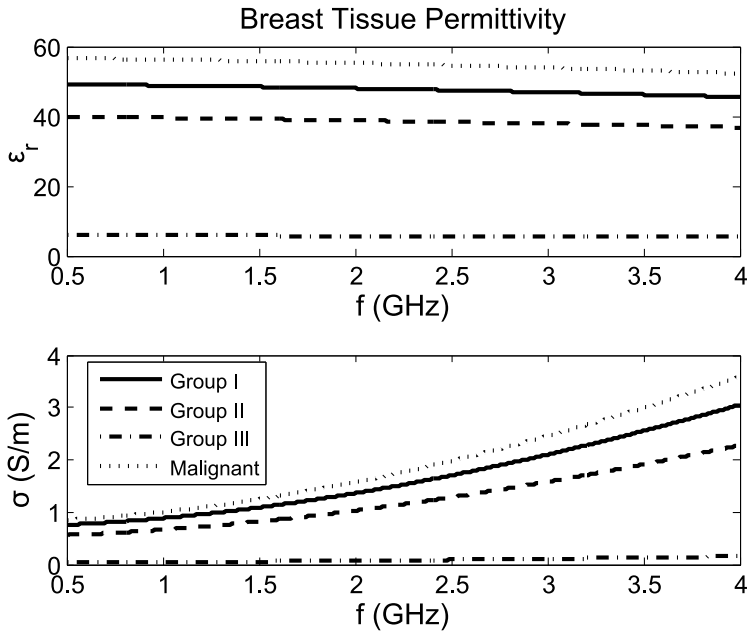

Figure 2.3 Variation of the electrical properties of breast tissue types as a function of frequency, based on Cole-Cole parameters given in (Lazebnik *et al.* (2007c,b)).

The values of the dielectric constant and the effective conductivity of the different breast tissues at 2.45GHz are summarized in table 2.1. The contrast in dielectric constant and effective conductivity between malignant and group III normal tissue is more than 10 times. However the contrast reduces to about 14% between malignant tissue and group I normal tissue. This fact poses a challenge for the detection of breast tumors, since Group I and II normal tissue corresponds to glandular and fibroconnective tissue (glandular region) where almost all of the tumors are produced.

2.2.2 Breast tissue modelling

As shown in the previous section, breast tissue can be quite heterogeneous and frequency dispersive. These two factors poses a challenge for the design and also the operation of micro-

Table 2.1 Complex dielectric constant of breast tissue at 2.45GHz.

Group	ε_r	σ_{eff}
I	47.53	1.665
II	38.41	1.257
III	4.717	0.087
Malignant	54.68	1.934

wave imaging systems applied to breast cancer detection. Accurate numerical breast models are important for the design and test of microwave imaging algorithms. Anatomically realistic numerical phantoms have been developed for this purpose (Zastrow *et al.* (2008)). These numerical phantoms are obtained from high resolution MRI images. The MRI images are segmented and then voxel intensities are transformed into dielectric properties using an appropriate mapping function. This process leads to very realistic 3D voxel models of the human breast which can then be imported into a 3D full-wave electromagnetic solver. A simplification of MRI derived numerical phantoms can be achieved allowing full-wave simulations to be performed on commercial codes without hardware acceleration or prohibitive simulation times (Zhu *et al.* (2009)).

Another important aspect of breast tissue imaging is the development of materials that closely simulate its electrical properties. These phantom materials are important for the test of microwave imaging systems in laboratory controlled experiments before clinical implementation. Different mixtures of liquids such as water, glycerin, corn syrup and canola oil have been proposed for producing very simple tissue mimicking phantoms (Bindu *et al.* (2004); Li *et al.* (2003)). More recently, the use of gelatin-like materials have been proposed for this application (Lazebnik *et al.* (2005); Croteau *et al.* (2009); Porter *et al.* (2010)). Such materials can be easily molded for producing anthropomorphic breast phantoms.

2.3 Inverse scattering for Microwave Tomography

Section 2.2 has reviewed the electrical properties of human breast tissues. This data suggests that electrical properties of these tissues are strong indicators of their functionality and possible pathological affections. This difference or contrast between the different tissue types will produce a scattering phenomena that can be modeled using the techniques described in section 2.1.

The scattering problem is generally defined as the *direct* problem, from a known incident field it is possible to calculate the scattered field produced by a dielectric object whose spatial

electrical properties are known. On the other hand, from a microwave tomography perspective we need to solve an *inverse* problem. In this case an unknown object is illuminated by a series of transmitters and the scattered field is measured at a series of receivers, from this measured scattered field the spatial distribution of the electrical properties, $\chi(\mathbf{r})$ of the unknown object are inferred.

The inverse scattering problem is normally solved using the following system of equations, which is derived from equation 2.12 and 2.13. Referring to figure 2.1, and the object being illuminated using M different transmitters :

$$\mathbf{y_i} = \mathbf{G_o X E_i} + n_i^o \tag{2.16}$$

$$\mathbf{E_i} = \mathbf{E_i^{inc}} + \mathbf{G_c X E_i} \tag{2.17}$$

Where i refers to the i-th independent illumination of the object, n_i^o is a noise term which models all the possible noise contributions from the measurement equipment, $\mathbf{y_i}$ is a vector of length N containing the measured scattered field at the receivers positions, $\mathbf{E_i}$ and $\mathbf{E_i^{inc}}$ are vectors of length n containing the total and incident field inside the region D, $\mathbf{X}$ is a diagonal matrix of size n by n containing the unknown contrast in each pixel or voxel and $\mathbf{G_o}$ and $\mathbf{G_c}$ are the observation and coupling discretized Green's functions.

Equations 2.16 and 2.17 can be combined to form an equation which is only a function of the contrast $\mathbf{X}$:

$$\mathbf{y_i} = \mathbf{G_o X (I - G_c X)^{-1} E_i^{inc}} \tag{2.18}$$

Equation 2.18 clearly shows the non-linearity of the problem with respect to $\mathbf{X}$. Most of the different inverse algorithms proposed in the literature are based in the solution of equation 2.18 or the system formed by 2.16 and 2.17. In all the cases the problem is ill-posed and requires regularization for obtaining a stable solution.

Linearization of the problem

The most simple method to aleviate the above mentioned mathematical difficulty is known as the Born approximation (Chew (1999)). In this approach it is assumed that the total field is equal to the incident field (i.e. $E_i \simeq E_i^{inc}$). The data equation then reduces to :

$$\mathbf{y_i} = \mathbf{G_o X E_i^{inc}} + n_i^o \tag{2.19}$$

A solution for the contrast can be found solving this linear equation using the least squares

method. This linear inverse problem is ill-posed and requires a regularization technique for its solution, examples of this regularization procedures are the truncated singular value decomposition or Tikhonov regularization (Pastorino (2010)). The approximation is only valid for very small contrasts or very small objects. Other approximations have been proposed for linearizing the inverse-scattering problem. Among them we can cite the Rytov approximation (Chew (1999)), the extended Born approximation (van den Berg et Abubakar (2002)) and the Diagonal Tensor approximation (Song et Liu (2005)). All of these techniques extend the validity of the original Born approximation, however their application is limited to weak or small contrasts. These approximations can also be used to find an initial guess for more elaborated iterative inversion algorithms or as a preconditioner to improve the convergence rate of the direct problem solution.

The Born approximation can also be used in the form of an iterative method to retrieve the unknown contrast function (van den Berg et Abubakar (2002); Ali et Moghaddam (2010)). The iterative procedure is started using the zeroth order Born approximation. At iteration k, the total field in the discretizated region is computed using equation 2.17 and the computed contrast function of the previous iteration ($\mathbf{X^{k-1}}$). $\mathbf{X^k}$ is then computed solving a linear inverse problem from equation 2.16. This procedure can greatly enhance the performance of the Born approximation.

Nonlinear Methods

Non-linear methods try to solve the inverse problem using optimization theory. In general, the objective is to minimize a cost function which is directly related to the quantity of interest, the contrast of the OUT in the case of MT.

Optimization theory includes global and local optimization methods. Although some research groups have applied global optimization methods such as simulated annealing, genetic algorithms or particle swarm optimization (Pastorino (2010)) to solve the microwave tomography problem, these methods become non practical from a computational burden point of view when applied to a realistic configuration. Improvements in computer capabilities, hardware acceleration techniques or parallel programming techniques can improve the speed of this kind of algorithms.

On the other hand, local optimization methods require much less computational cost. However they can only assure convergence into a local minimum of the cost function. Moreover, these methods are generally very efficient to deal with "medium" sized objects (the upper boundary limit for these algorithms is not very clear in the literature), which are larger (or present higher contrasts) than those efficiently treated by linear methods.

Among the most popular local optimization methods applied to microwave tomography

are the distorted Born iterative (DBI) (Chew (1999)) method and the contrast source inversion (CSI) method (van den Berg et Abubakar (2002)). DBI is an iterative method similar to the Born iterative method, where at each iteration the contrast function is updated as :

$$\mathbf{X^{(k+1)}} = \mathbf{X^{(k)}} + \delta\mathbf{X^{(k)}} \tag{2.20}$$

And the scattered field at the receiver positions is calculated as :

$$\mathbf{E_i^{s(k+1)}} = \mathbf{G_{oI}}^{\mathbf{(k)}}\delta\mathbf{X^{(k)}}\mathbf{E_i^{(k)}} \tag{2.21}$$

Where $\mathbf{G_{oI}}^{\mathbf{(k)}}$ is the inhomogeneous Green's function calculated at iteration k. This Green's function has to be computed numerically from the MT system of equations (Pastorino (2010)). The detailed description of the algorithm is described in (Chew et Wang (1990)), and it can be summarized in the following steps.

First the initial contrast function ($\mathbf{X^0}$) is computed using the Born approximation, as well as, the initial inhomogeneous Green's function. At each iteration a linear inverse problem is solved to compute $\delta\mathbf{X^{k+1}}$ by minimizing the cost function 2.22, which is just the residual error between the measured and calculated scattered field, following the procedure in (Chew et Wang (1990)). Once the updated value of $\delta\mathbf{X}$ is known, the values of $\mathbf{G_{oI}}^{\mathbf{(k)}}$ and $\mathbf{E_i^{(k)}}$ are computed. Then, $\mathbf{E_i^{s(k+1)}}$ is computed and its value is used to compute the residual error. The iterative procedure is continued until this residual error is smaller than a given threshold.

$$\mathbf{F}(\chi) = \sum_i \left\|\mathbf{y_i} - \mathbf{E_i^{sk}}\right\|^2 \tag{2.22}$$

The DBI method usually converges in a few iterations, however each iteration requires the computation of the inhomogeneous Green's function and the solution of a linear inverse problem, both of which can be computationally expensive. This method has been applied successfully in microwave tomography however it requires a very efficient forward solver. The introduction of parallel computing techniques and Graphical Processing units (GPU) allows a fast solution of the forward problem at each iteration (Winters *et al.* (2009)).

In the CSI method (van den Berg et Abubakar (2002)), the solution of a forward problem is not needed for each iteration. The MT equation system described in 2.16 and 2.17 is written as a function of the contrast sources $\mathbf{w_i} = \mathbf{XE_i}$:

$$\mathbf{y_i} = \mathbf{G_o w_i} + n_i^o \tag{2.23}$$

$$\mathbf{w_i} = \mathbf{X}(\mathbf{E_i}^{\mathbf{inc}} + \mathbf{G_c w_i}) \tag{2.24}$$

The inverse problem is then treated as an optimization problem where a cost function is minimized with respect to the two unknowns of the problem. The optimization algorithm used in the CSI method is the non-linear conjugate gradient algorithm (Nocedal et Wright (2006)). An iterative minimization algorithm requires the computation of a descent direction and the step length at each iteration (Nocedal et Wright (2006)). In the CSI method, both contrast and currents are updated as :

$$\mathbf{X^{(k+1)}} = \mathbf{X^{(k)}} + \alpha_X^{(k)} \mathbf{p_X^{(k)}} \tag{2.25}$$

$$\mathbf{W^{(k+1)}} = \mathbf{W^{(k)}} + \alpha_W^{(k)} \mathbf{p_W^{(k)}} \tag{2.26}$$

Where W is a vector containing the constrast sources for the M different illuminations ($i = 1$ to M) and the quantities $\alpha_X^{(k)}, \mathbf{p_X^{(k)}}$ and $\alpha_W^{(k)}, \mathbf{p_W^{(k)}}$ are the step length and direction descent for minimization with respect to the contrast function and the equivalent currents respectively. A regularized version of the CSI method is the Multiplicative Regularization CSI method (MR-CSI) (van den Berg et Abubakar (2002); Abubakar *et al.* (2002)). The cost function for the MR-CSI is the weighted sum of the errors in equations 2.23 and 2.24 multiplied by a regularization term :

$$\mathbf{F_{CSI}^k}(\mathbf{X}, \mathbf{W}) = (\mathbf{F_1} + \lambda^k \mathbf{F_2}) \mathbf{F_r^k} \tag{2.27}$$

$$\mathbf{F_1}(\mathbf{W}) = \frac{\sum_{i=1}^{M} ||\mathbf{y_i} - \mathbf{G_o} \mathbf{w_i}||^2}{\sum_{i=1}^{M} ||\mathbf{y_i}||^2} \tag{2.28}$$

$$\mathbf{F_2}^k(\mathbf{X}, \mathbf{W}) = \frac{\sum_{i=1}^{M} ||\mathbf{X}(\mathbf{E_i^{inc}} + \mathbf{G_c} \mathbf{w_i}) - \mathbf{w_i}||^2}{\sum_{i=1}^{M} ||\mathbf{X^{k-1}}(\mathbf{E_i^{inc}})||^2} \tag{2.29}$$

$$\mathbf{F_r^k} = \mathbf{F_{WL2}^k}(\mathbf{X}) = \frac{\Delta^2}{S} \sum_{p=1}^{n} \frac{|\bigtriangledown \mathbf{X_p^k}|^2 + (\delta^k)^2}{|\nabla \mathbf{X_p^{k-1}}|^2 + (\delta^k)^2} \tag{2.30}$$

Where $\mathbf{F_r}$ is the regularization term, S is the surface of the imaging domain D, Δ is the discretization step and $|\nabla \mathbf{X_p^k}|^2$ is a factor that computes the gradient of the contrast function along the x and y directions.

The parameters λ^k and δ^k play a key role on the stability of the algorithm and are automatically computed at each iteration in the MR-CSI method. The expressions for computing

these parameters, the gradients expressions, as well as other details of the algorithm can be found in (Abubakar *et al.* (2002)).

The original CSI method needs a lot more iterations than DBI to converge but it produces very similar results in terms of accuracy and computational cost. However it has been shown in (Barriere *et al.* (2007)), that the CSI method can be modified to obtain accurate results while improving the rate of convergence of the algorithm leading to faster results.

2.4 Microwave tomography systems for medical imaging

Medical imaging applications of microwave signals have been an active research field in the past 20 years. Among the different prototypes developed for this application, we can refer to the initial experiments conducted by Larsen and Jacobi (Larsen et Jacobi (1979, 1985)), the 2.45GHz microwave camera by Franchois, Bolomey et al. (Franchois *et al.* (1998)), the 2.45GHz cylindrical scanner by Jofre et al. (Jofre *et al.* (1990)) and the 2.45GHz circular tomographic scanner by Semenov et al. (Semenov *et al.* (1999)).

2.4.1 Measurement setups for breast cancer detection

Recent work in the field of microwave tomography applied to breast cancer detection includes the development of several clinical or pre-clinical prototypes. Among them, we can cite the clinical system developed at Dartmouth College (Meaney *et al.* (2000)), the system developed at the Technical University of Denmark (Zhurbenko *et al.* (2010)), the CMI clinical prototype developed at Bristol University (Klemm *et al.* (2009b,a, 2010)), the Duke University's MT system (Stang (2008)) and the MT system developed at Chalmers University (Fhager *et al.* (2011)). Pictures of the different systems are shown in Figures 2.4 to 2.7.

Figure 2.4 Dartmouth College microwave spectroscopy clinical prototype (Meaney *et al.* (2000)). Image obtained from Dartmouth College website

Figure 2.5 University of Bristol CMI clinical prototype. Image obtained from (Henriksson *et al.* (2011)).

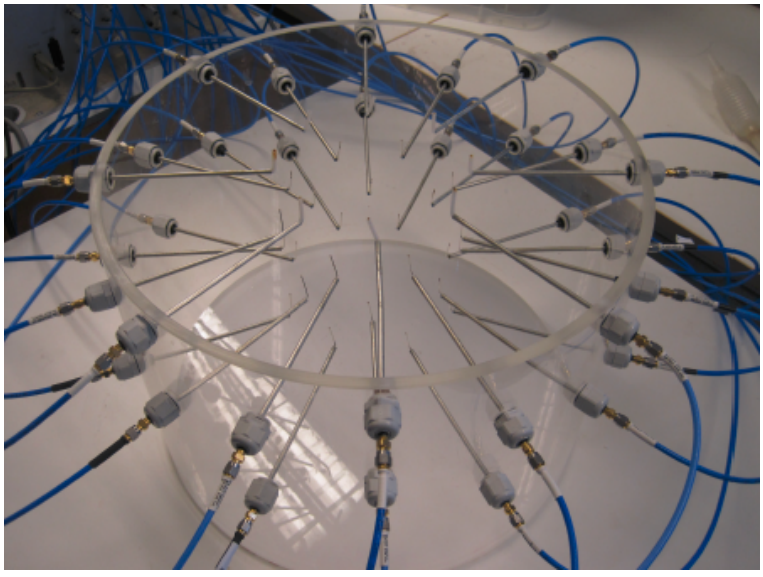

Figure 2.6 University of Chalmers clinical prototype. Image obtained from (Fhager *et al.* (2011)).

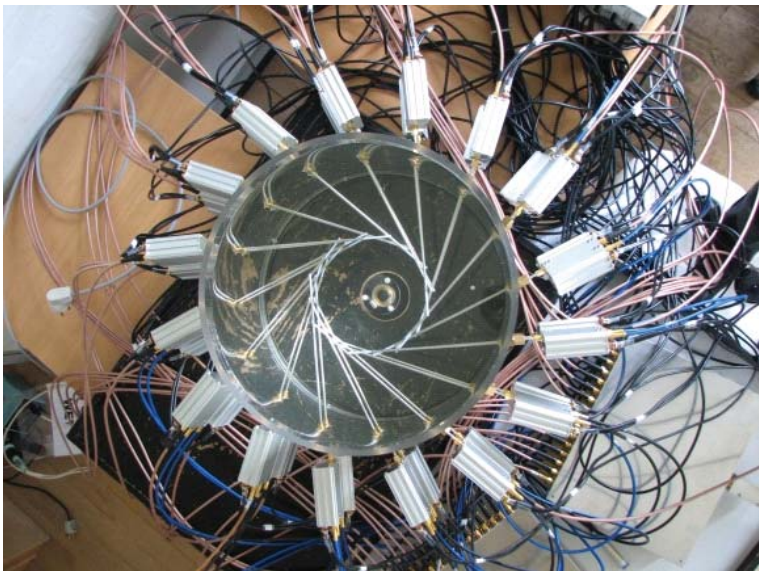

Figure 2.7 DTU's microwave tomography clinical system. Image obtained from DTU website.

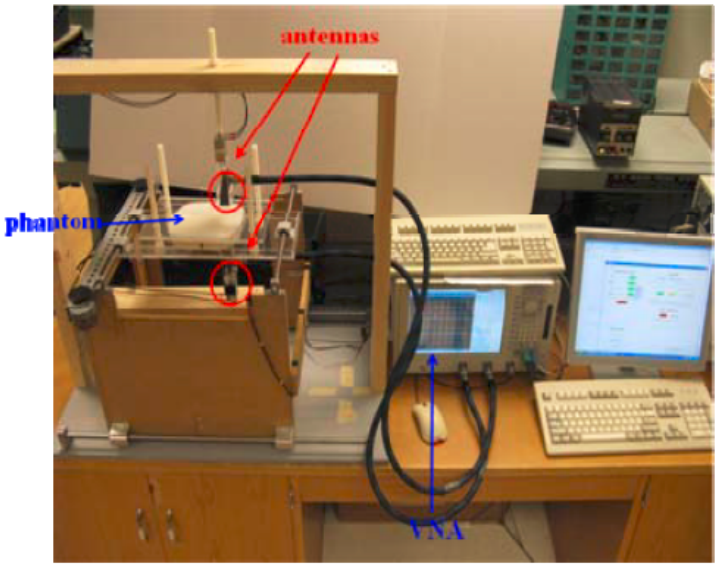

Figure 2.8 McMaster University Raster scan. Image obtained from (Amineh *et al.* (2011a)).

The original system presented in (Meaney *et al.* (2000)) is a 2.5D imaging system and shown in Figure 2.4. This means that the image of the breast is obtained as a superposition of 2D slices. In the measurement setup, the patient is lying prone in an examination table with the breast pending in a liquid filled tank. The liquid is needed for impedance matching purposes and to reduce the modeling error when considering the system to be immersed in a homogeneous medium. The breast is surrounded by an array of monopole antennas, as shown

in figure 2.4. The array of antennas move up and down to obtain the data at the different planes. The monopole antenna was chosen for this application because it can be easily and accurately modeled, it is simple to fabricate and a broadband response can be obtained when immersed in a lossy medium. All the antennas can be used as transmitters and receivers. The signals are collected in a parallel-detection scheme as described in (Li *et al.* (2004)). This parallel-detection scheme allows for very fast data acquisition. The current version of this system has an operative bandwidth from 500-3000MHz with inter-plane imaging capability (transmitting and receiving antenna at different heights) for 3D image reconstruction as described in (Fang *et al.* (2010)), recently it has been shown that it is possible to take a 3D image of a patient in less than 20 minutes, including examination of the patient and image reconstruction (Grzegorczyk *et al.* (2012)).

The system presented in (Zhurbenko *et al.* (2010)) is a full 3D microwave imaging system. The complete description of the microwave hardware is described in (Zhurbenko (2008)). An image of the system is shown in figure 2.7. It consists on an array of 32 monopole antennas horizontally placed in a bird's nest arrangement. The array is also placed in a liquid filled tank. For each antenna transmitting, the data is collected at the other 31 antennas, resulting in a total of 32x31 measurements. The measurement process takes approximately less than one minute per breast.

The Chalmer's University system is described in (Fhager *et al.* (2011); Zeng *et al.* (2011)). As it can be seen in Figure 2.6, it consists on several rings of monopole antennas in a very similar arrangement to the previously presented systems. The particularity of the system is that the measurements are taken in the time domain. An ultra-wideband (UWB) signal is generated using a pulse generator and the response is measured using a sampling oscilloscope. The advantage of this system is that it can measure a wideband signal faster compared to a frequency swept measurement. An interesting study comparing the performances of a frequency domain versus a time domain measurement system is performed in (Zeng *et al.* (2011)).

Another interesting approach is the one proposed by the University of Bristol (Klemm *et al.* (2009b)). This is the first implementation of a clinical radar system. A picture of the system is shown in Figure 2.5. It consists of an hemispherical conformal array of 60 wide-band patch antennas. Using this approach, qualitative reconstruction images of small objects have been successfully achieved. Clinical tests of this system are currently ongoing. The measurements are taken using an 8-port VNA, that considerably accelerates the measurement procedure (Henriksson *et al.* (2011)).

In (Stang (2008)), the hardware design of a clinical prototype as a continuation of the very active research in microwave tomography at Duke University is described. It consists

in a conformal array of patch antennas surrounding the breast, where no matching fluid is used. Instead, custom solid inserts made of low-loss dielectric materials have been used for matching purposes.

Finally, another interesting approach is the raster-scan system developed at McMaster University, a picture of which is shown in Figure 2.8. It consists of two wideband horn antennas that scan the surface of the breast compressed between two dielectric plates, one antenna above and the other below the plates. Qualitative images of scatterers inside phantoms have been succesfully produced with this system (Amineh *et al.* (2011b,a)).

2.4.2 Other measurement setups available in the literature

Several other MT measurement setups have been developed for biomedical or non-destructive test applications. In general these systems consist in an array of antennas combined with a switch matrix to measure the transmission between a pair of antennas in the array. The measurement is generally done using a vector network analyzer (VNA). Two examples of MT measurement setups are shown in Figures 2.9 and 2.10.

The University of Manitoba system consists in a series of Vivaldi antennas arranged in a circular configuration (Gilmore *et al.* (2010)). The system is designed to operate in air, frequency limited by the bandwidth of the antennas (3 to 6 GHz). The antennas are oriented to generate a vertically polarized field which is used to obtain quantitative 2D images of elongated objects. A variation of the system was presented in (Ostadrahimi *et al.* (2012)), where in this case the measurements are taken using an indirect field measurement technique based in the modulated scattering technique.

Several other MT systems have been developed for different biomedical applications, among them we have the previously cited works by Semenov (Semenov *et al.* (2000, 2002)) and the MT based stroke detection system of Chalmers University (Fhager et Persson (2011); Fhager *et al.* (2010)). The stroke detection system is shown in Figure 2.10. It consists in a series of triangular patch antennas mounted in a helmet to monitor the brain and make a fast diagnostic of the patient suspected to suffer a stroke.

2.5 Hybrid Methods

The recent study presented in (Lazebnik *et al.* (2007b)) has shown that the small contrast between malignant and fibroglandular tissue poses a major challenge for microwave early detection of breast tumors. For this purpose, some hybrid techniques have been proposed to enhance the results obtained with microwave tomography.

In (Zhao *et al.* (2008)), dielectric and elastic contrasts are combined to enhance breast

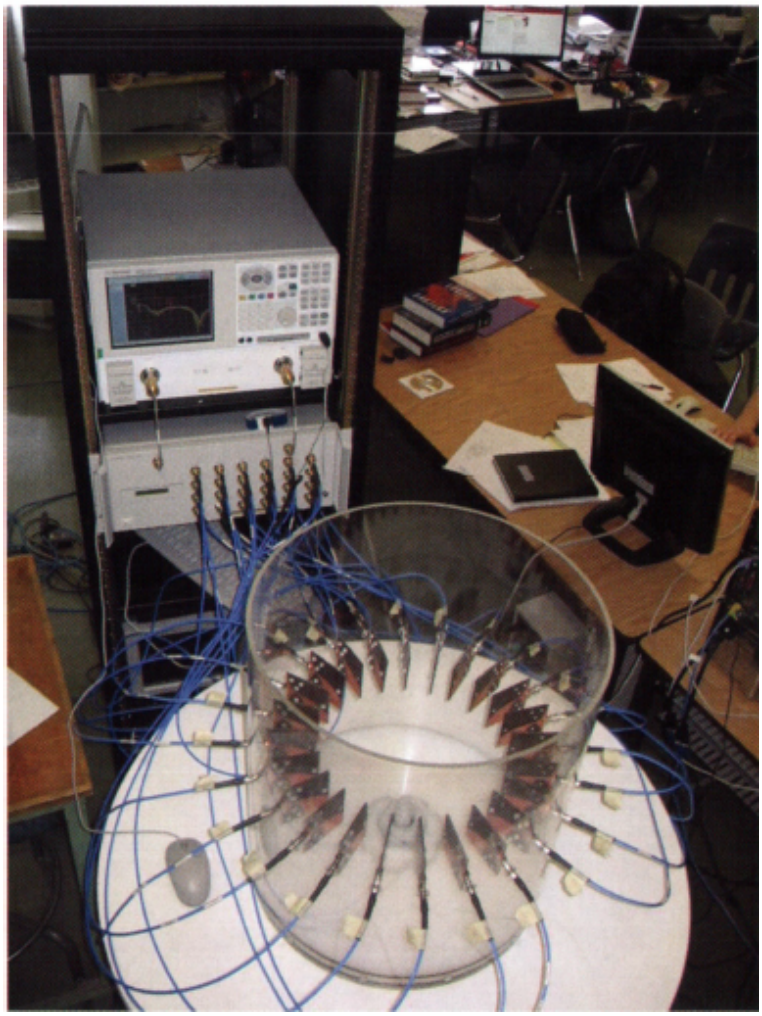

Figure 2.9 University of Manitoba microwave tomography system. Image obtained from University of Manitoba website.

cancer detection, since malignant tissue is considerably stiffer than both adipose and fibroglandular tissue according to (Samani *et al.* (2003)). The breast is mechanically compressed to induce a displacement, while at the same time, a microwave signal is transmitted into the breast and the scattered field is collected using an antenna array. The mechanical displacement will modulate the scattered field measured at the receiver. Hence, the total scattered field has two components, the normal scattered field due to the dielectric contrast and a Doppler field perturbation due to mechanical vibration. A numerical study of this method is performed in (Zhao *et al.* (2008)) and a 5dB improvement in the measured scattered field is obtained (for the same malignant to fibroglandular contrast).

The use of contrast agents to increase the contrast between normal and malignant fibroglandular tissue is studied in (Shea *et al.* (2009)). The contrast agent used in this application,

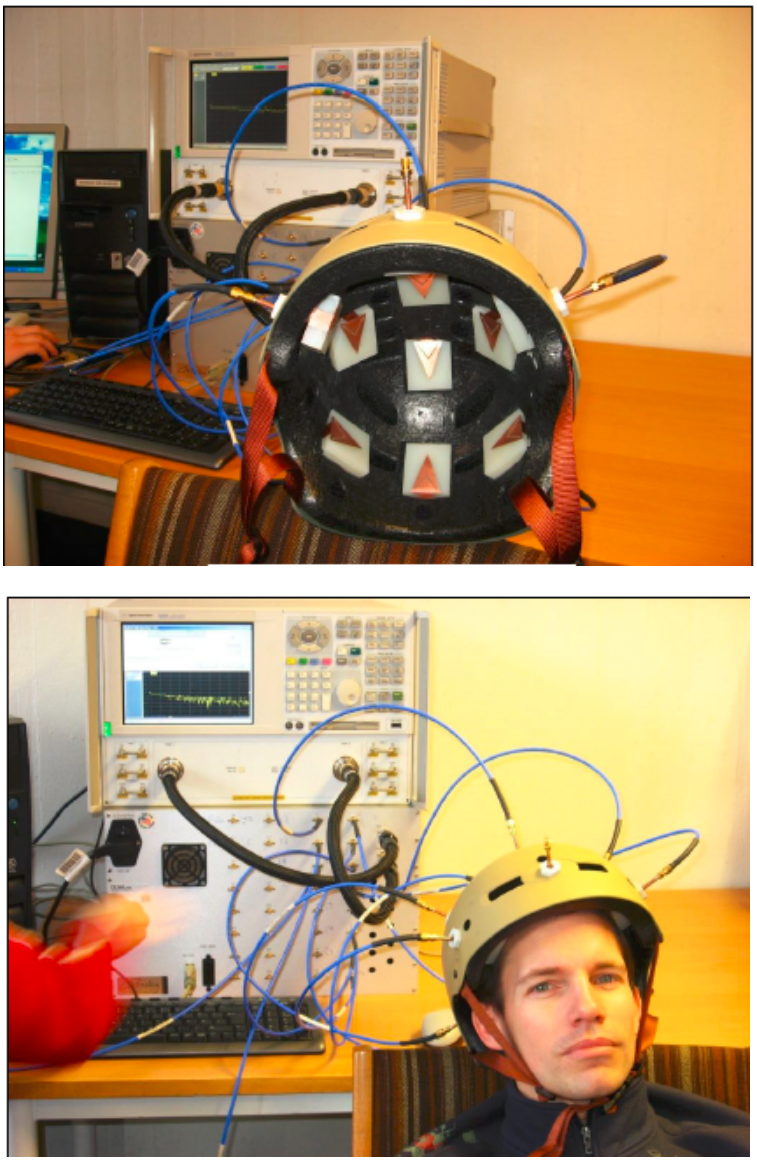

Figure 2.10 Chalmers University microwave tomography system for the detection of brain stroke. Image obtained from Chalmers University webpage.

micro bubbles that accumulate passively in tumors (Mashal *et al.* (2010)), acts by lowering the permittivity of the malignant tissue. The imaging process is taken in two steps, with and without contrast agent, and the difference of the two images is obtained to detect possible breast tumors.

CHAPTER 3

Measurement Setup Configurations for Planar Microwave Tomography

In this chapter, an analysis of Microwave Tomography (MT) measurement setups is performed for different configurations based on breast compression. These types of configurations allow measuring the evanescent component of the scattered field and a compact measurement setup that can be easily integrated in a standard mammography system.

3.1 Introduction

A measurement setup in MT typically includes a series of receiving (Rx) and transmitting (Tx) antennas for measuring the scattered fields needed for the reconstruction algorithms. The antennas can be arranged in planar, cylindrical or hemi-spherical surfaces. In the available clinical prototypes, the patient lies prone in a table with the breast pendant in a liquid (Meaney *et al.* (2000); Craddock *et al.* (2008)). This configuration has been proposed for maximizing the comfort of the patient. In such a case, a cylindrical or hemi-spherical configuration is preferred since the antennas can be conformal with the shape of the breast and can accurately sample the scattered fields. In particular, compression of the breast may present several advantages over this classical configuration (Diaz-Bolado *et al.* (2011a,b)). The Tx and Rx antennas can be placed very close to the OUT, allowing the measurement of the evanescent scattered fields. Also, this procedure can lead to simplifications of the reconstruction algorithm since the thickness is precisely known, or the *a priori* information from mammography can be integrated in the solution of the inverse problem. Finally, the fact that the breast could be in similar geometrical configurations in both X-ray mammography and MT would make it easier to compare and correlate the images obtained with the two methods. Such a combined approach has already been used with other techniques, i.e. mammography with optical imaging or positron emission tomography with computed tomography (Fang *et al.* (2009)). In the case of a configuration using breast compression, a planar configuration for the Tx/Rx antenna array will be better adapted.

Evanescent scattered fields have been exploited for a long time in the area of microwave near-field microscopy (Gao et Xiang (1998); Kleismit *et al.* (2006)). This approach is commonly used in non-destructive evaluation of materials allowing spatial resolutions in the order of the nanometer. The exploitation of evanescent scattered fields in MT was proposed in (Bucci *et al.* (1999, 2001)). The authors showed that an enhancement in the reconstructed

images obtained in MT was obtained by using close-proximity setups, however this enhancement was limited to the region near the edges of the imaging domain.

In this chapter, we will analyze how the quality of the reconstructed images can be improved through breast compression. First of all, we will discuss different possibilities for the implementation of a planar MT measurement setup using breast compression. Next, we will shortly introduce the analysis techniques used for the comparison of the different configurations. This will include a review of the mechanical properties of the breast and a simple analysis of the deformation of breast tissues under compression. Finally the results of the analysis will show when and how we can improve the image quality by exploiting the measurement of evanescent scattered fields.

3.2 Different configurations for the MT setup based on breast compression

Planar measurement setups for microwave imaging have already been studied in the literature, including the planar microwave camera (Franchois *et al.* (1998); Henriksson *et al.* (2010)) or the raster scan proposed in (Amineh *et al.* (2011b)) that used breast compression. However, no analysis of the effect of breast compression on the quality of the obtained images was discussed. Different possibilities are available for the implementation of a planar MT setup. The first and more straightforward idea could be to implement a planar array of antennas to be used as Tx and Rx. This configuration has the drawback that the antennas, being in close proximity of the scatterers, will disturb the field to be measured. A possible solution to this problem is to include the antennas in the formulation of the problem taking into account their presence in the discretization of the MT system of equations (Paulsen et Meaney (1999); Franza *et al.* (2002)). Another possibility is to use an array of small near-field probes to minimize perturbations in the measured field (Memarzadeh-Tehran *et al.* (2010)).

The configurations considered in this chapter are shown in Figure 3.1. Figure 3.1(a) shows a classical circular MT setup where both the Tx and Rx probes are placed in a circle surrounding the OUT. Usually both the Tx probes, Rx probes and OUT are immersed in a matching medium that is properly chosen to maximize field coupling between the probes and the region of interest in the OUT. Two configurations based in breast compression are shown in figures 3.1(b) and 3.1(c). The first one, which will be referred to as the camera configuration, is a setup that consists in a series of Tx's illuminating the OUT from one side and an array of near-field measurement probes on the other side. This setup arrangement creates a very compact system that could be integrated with a standard mammography apparatus. A drawback of this configuration is the fact that we can only have transmission information through the object, which translates into a limited view of the OUT. The second compressed

configuration shown in figure 3.1(c) will be called the waveguide configuration. The compound structure formed by the immersion medium, the enclosure formed by the dielectric plates and the surrounding air region can be seen as a multilayer dielectric waveguide. The structure is capable of guiding different TE^x (E_z) or TM^x (E_x and E_y) modes depending on the frequency of operation, the dielectric properties of the immersion media and dielectric plates and the thickness of the different layers. Combinations of the different modes can be launched by using an array of transmitting antennas and varying the phase shift between them (Diaz-Bolado et Laurin (2008)). This configuration has the advantage that the scattered fields can be measured both on top and bottom of the structure thus doubling the information compared to the camera configuration. This configuration also allows the exploitation of spatial and modal diversity to create the desired number of independent illuminations. In the 2D case this fact can be a limitation since the number of independent illuminations is limited to twice the number of possible modes in the waveguide, considering propagation along the positive and negative x axis, and that only the propagating modes are considered. In the 3D case this is no longer a limiting factor since the additional dimension gives the freedom in the spatial diversity to create the desired number of independent illuminations.

3.3 Numerical Models

In this section the different numerical phantoms used in the reconstructions will be presented. Since we are comparing measurement setups with and without compression, it is important, in order to make a comparison between the configurations, to have a model that takes into account, at least approximately, the deformation of the various breast regions resulting from the compression. For this purpose, we will perform a simple mechanical analysis of the compressed breast tissues. Then, the numerical phantoms used in the different reconstructions will be presented. These numerical breast models have been inspired from the anatomically realistic numerical breast phantoms presented in (Zastrow *et al.* (2008)).

3.3.1 Mechanical properties of Breast Tissues

The mechanical properties of human tissues have been an active research subject in different medical applications. Previously we have mentioned elastography, which is a technique for imaging soft tissue elastic modulus. However breast tissue deformation is also studied for image comparison between mammography and other non-compressing techniques such as CT or MRI of the breast (Kellner *et al.* (2007)) or image guided surgery (Miga *et al.* (1999)).

In all of these applications, breast tissues are generally approximately modelled as linearly-elastic materials. A material will experience mechanical deformation when a force is applied

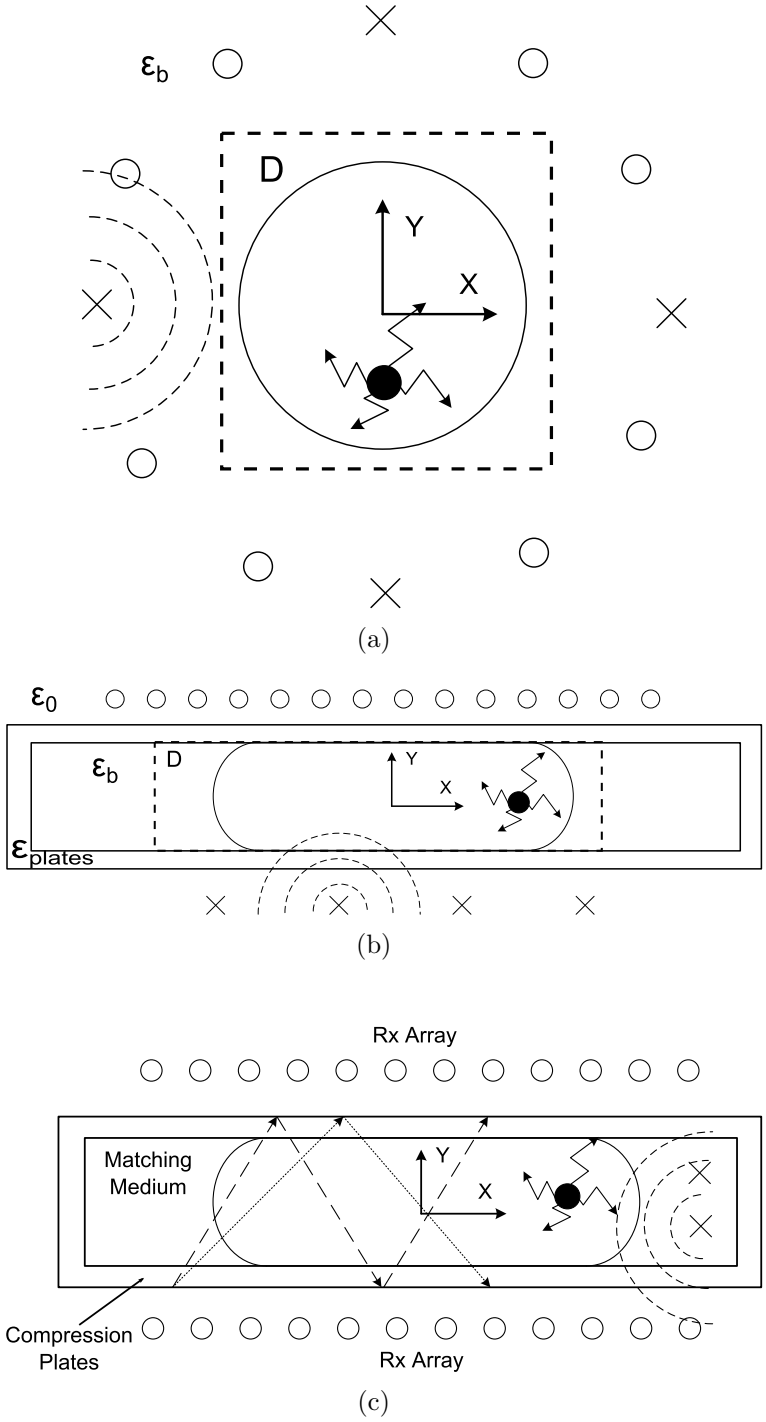

Figure 3.1 MT configurations analyzed in this chapter.(a) Circular MT configuration. (b) Camera configuration. (c) Waveguide configuration

to it. An elastic material is defined as a material which returns to its original unloaded dimensions when the load is removed. In a linear elastic material the relation between the

stress and strain of the material is constant ang given by the Hooke's Law. Stress is defined as the ratio between the load applied to a material for a given area ($\sigma = P/A[N/m^2]$), whereas the strain is defined as the ratio between the change in length of a material and its original length when a load is applied to it ($\epsilon = \delta L/L$) (Bazergui *et al.* (1993)). In this case, we are interested in determining the deformation of an object under compression, as it can be seen in figure 3.2.

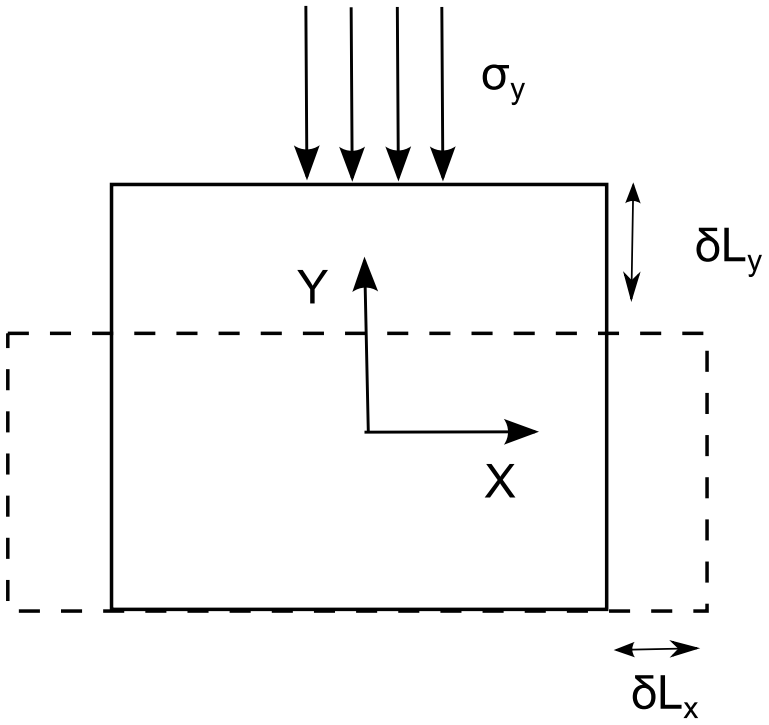

Figure 3.2 Schema of the mechanical deformation of an object subject to normal stress.

Linear-elastic materials are characterized from two parameters, Young's Modulus ($E = \sigma/\epsilon$) and Poisson's ratio ($\nu = -\delta L_x/\delta L_y$ with $-1 < \nu < 0.5$) (Bazergui *et al.* (1993)). In order to make a consistent comparison between the different configurations, we will analyze the deformation experienced by a breast-like object composed of fat and glandular tissue. For this analysis, we will use CST Multiphysics, which is part of the CST Studio suite and includes a mechanical solver based on the finite element method. The results were also confirmed using ANSYS Mechanical solver. The simulation geometry is shown in Figure 3.3(a). The highly simplified breast-like object consists in a sphere of radius 8cm whose center is placed at the coordinate origin. To obtain the compressed breast shape, the sphere is cut at planes $z = 0$ and $y = \pm 3cm$. A smaller sphere of radius 0.75cm, centered at $x = 0$, $y = 0$ and $z = 4cm$ is added. The cut sphere represents fatty tissue and the small sphere represents glandular tissue. The two objects are assigned the mechanical properties given in (Kellner *et al.* (2007)),

and reported in Table 3.1. These properties were obtained from a compilation of different published results both from *in vivo* and *in vitro* measurements of human tissues. However, breast tissues are quite heterogeneous and these values could vary greatly among different patients or parts of the breast.

Table 3.1 Mechanical and Electrical properties of the different tissues present in the numerical phantoms

Parameter	Fat	Fibroglandular	Immersion medium
Young's Modulus	1 KPa	10KPa	-
Poisson's ratio	0.49	0.49	-
Permittivity	7	45	15
Conductivity	0.16S/m	1.36S/m	0.4S/m

A small displacement of 3mm is applied to the compression plates at $y = -3cm$ and $y = +3cm$ in the $+y$ and $-y$ directions respectively, as shown in Figure 3.3(a), while the plane $z = 0$ is held fixed to simulate the stiffness of the thorax. This small displacement is used to preserve the validity of the linearly-elastic formulation, since this tissue model is valid only for small deformations where the strain should be kept smaller than 5%. However for the simple case we want to simulate, this approximation will give an idea of how the breast tissue reacts under compression. Figure 3.3(b) shows the displacement vector obtained from the simulation. As can be seen, the fat part of the object assumes the most of the deformation, while the shape of the glandular region remains more or less unchanged, as its displacement is along z and more or less constant over its volume. This effect was expected since the glandular tissue has a Young's modulus ten times higher than that of the fat tissue.

3.3.2 Numerical Breast Phantoms

The numerical phantoms that will be used in the different reconstructions performed in section 3.5.2 are shown in Figure 3.4. They differ in the content of fibroglandular tissue, and they will be identified in the sequel as *mostly fatty*, *scattered fibroglandular* and *very dense*. All these phantoms consist of a mixture of fat and glandular tissue, whose electrical properties at the frequency of 2.45GHz are given in Table 3.1 (Lazebnik *et al.* (2007a)). In the uncompressed phantoms, the fat portion is a circle of 29mm in radius and the glandular portion varies from one phantom to the other to reflect the percentage of glandular tissue corresponding to each category. In Section 3.3.1, it was shown how under compression the fat tissue suffers more deformation than the glandular tissue due to its lower stiffness. Taking this into account, it was assumed that the fat portion is deformed into a flattened ellipse

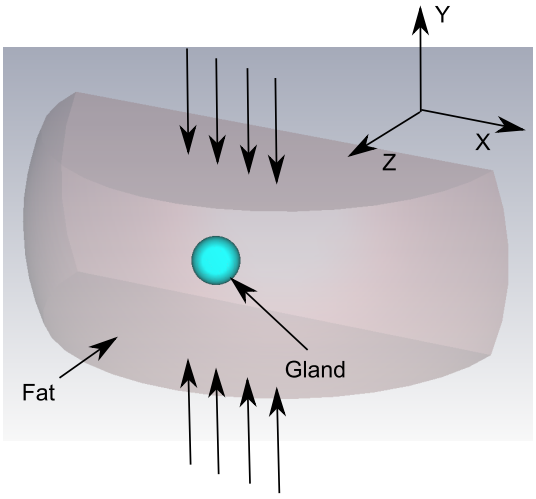

(a)

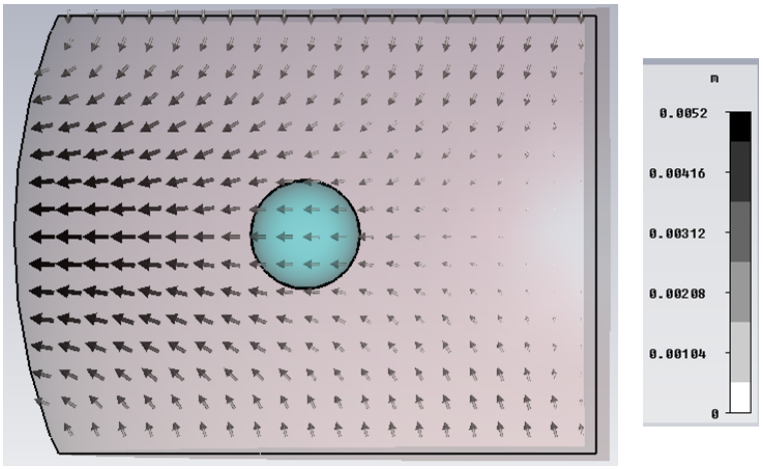

(b)

Figure 3.3 Results of the CST multyphisics simulation. (a) Simulation model. (b) Displacement vector in the $x = 0$ plane. The grey scale indicates local tissue displacement in meters.

keeping the volume of the breast constant, whereas the glandular portion is kept unchanged. The same volume is also maintained for the immersion medium.

3.4 Analysis Techniques

In this section, the inversion algorithm used for the reconstructions will be shortly explained, as well as, an efficient way to attack the inhomogeneous inverse scattering problem of the breast compression based configurations. In a general MT problem the OUT is placed inside a domain D and it is sequentially illuminated using a series of M different transmitting antennas. For each illumination the scattered field is measured at N points. For all the confi-

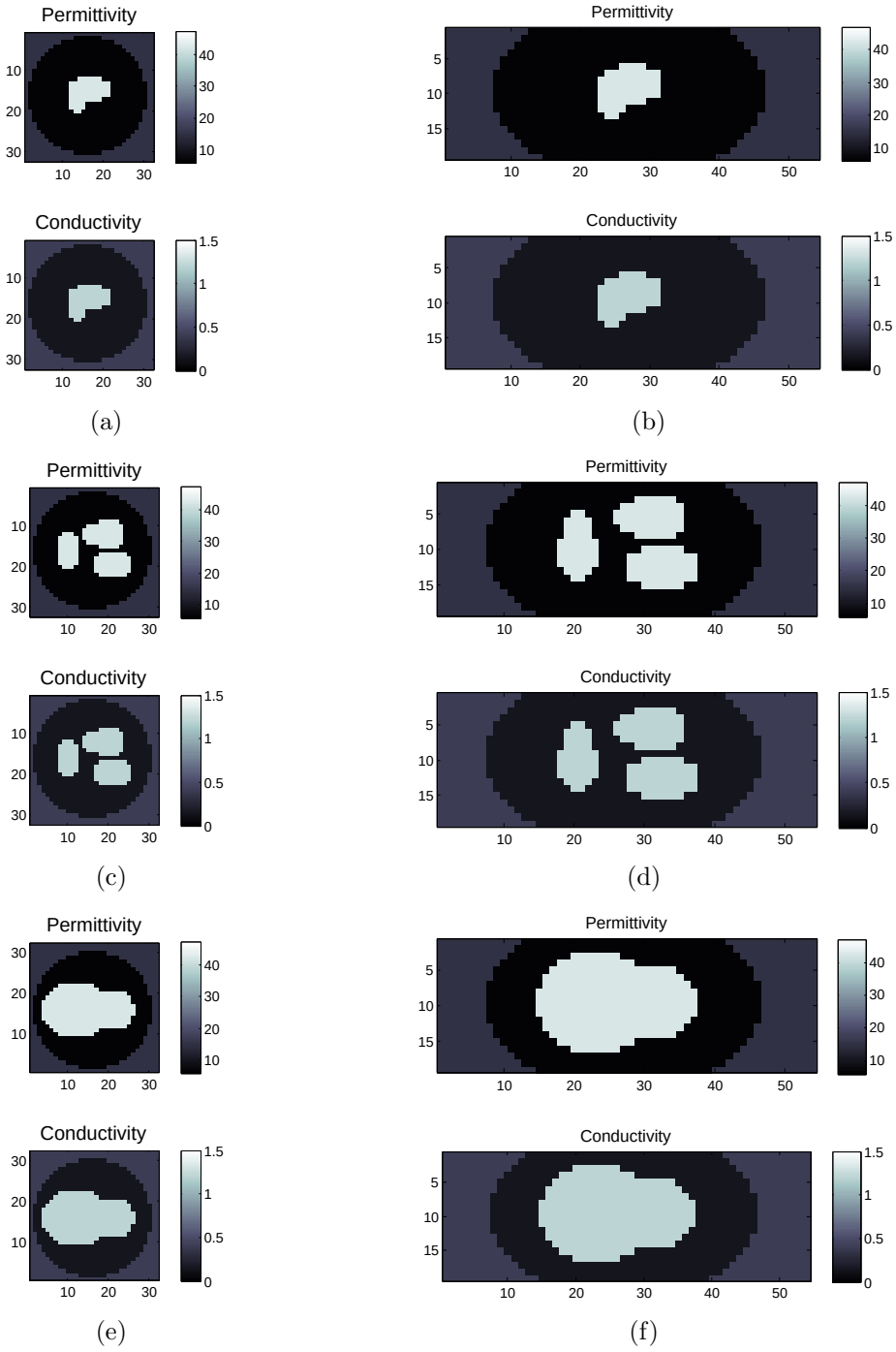

Figure 3.4 Six phantoms used in the reconstructions with and without compression. (a) (b) Mostly fatty phantom without and with compression. (c) (d) Scattered fibroglandular phantom without and with compression. (e) (f) Very dense phantom without and with compression.

gurations previously explained, a 2D TM case is considered, that is, the objects are infinite along the z direction and the electric field has only a z component. A system of two inte-

gral equations defines the scattering problem. Following the development in (Abubakar *et al.* (2002)), we can discretize the system of equations using the Method of Moments (MoM) with pulse basis functions and point matching and obtain the following system of matrix equations :

$$\mathbf{y_i} = \mathbf{G_o w_i} \tag{3.1}$$

$$\mathbf{w_i} = \mathbf{X}(\mathbf{E_i^0} + \mathbf{G_c w_i}) \tag{3.2}$$

Where we have $i = 1...M$. The domain D is discretized in n pixels ($n = n_x \times n_y$). Vector $\mathbf{y_i}$ of size N contains the measured scattered fields due to the i^{th} illumination. $\mathbf{E_i^0}$ is the incident field vector of length n in the domain D when no OUT is present. $\mathbf{G_o}$ and $\mathbf{G_c}$ are the observation and coupling Green matrices of size $N \times n$ and $n \times n$ respectively. These matrices are calculated from the discretization of the 2D Green's function (GF) of the domain D.

$\mathbf{X}$ and $\mathbf{w_i}$ are the unknowns of the problem. $\mathbf{X}$ is a diagonal matrix ($\mathbf{X} = diag(\mathbf{x})$), where $\mathbf{x}$ is a vector of length n containing the discretized version of the contrast function which is defined as $\chi(\mathbf{r}) = (\epsilon(\mathbf{r}) - \epsilon_b)/\epsilon_b$. $\epsilon(\mathbf{r})$ is the unknown complex permittivity in the discretization region D and ϵ_b is the complex permittivity of the background medium. Finally, $\mathbf{w_i}$ is a vector which contains the induced polarization currents in the OUT ($\mathbf{w_i} = \mathbf{X E_i^t}$), where $\mathbf{E_i^t}$ is the total electric field in the domain D. The unknowns $\mathbf{X}$ and $\mathbf{w_i}$ are found through a modified version of the well-known CSI technique presented in (Barriere *et al.* (2011)) and deteailed in Annex A. The quality of the reconstructed images will be compared in terms of the Mean Square Error (MSE) after a fixed number of iterations of the algorithm, where MSE is defined as $\Delta\mathbf{x} = \|\mathbf{x} - \mathbf{x_0}\|^2 / \|\mathbf{x_0}\|^2$, in which x_0 is the known imposed contrast.

The configurations for the MT proposed in Figure 3.1 and based on breast compression needs some modifications for the solution of the MT inverse problem. In these configurations we have to consider the dielectric medium of the compression plates. Following the general formulation, we should use the homogeneous GF for the background air region, and define the contrast function for the whole region containing the plates and the immersion medium with a considerable computational overhead. However, since we are only interested in imaging the region between the compression plates it would be quite advantageous to reduce the size of the discretization region. This is quite possible because the geometry and electrical properties of the plates are well known. For this purpose a modified GF and incident field need to be computed to take into account of the presence of the inhomogeneous background.

The computation of inhomogeneous GF is widely treated in the literature, specially for the case of infinite multilayered media (Tai (1994); Chew (1999); Mosig et Itoh (1989)).

However, the geometries presented in Figure 3.1 are laterally closed to contain the matching fluid and allow a compact measurement setup, in such a case, our inhomogeneous media cannot be considered as an infinite multilayered media. Another possibility is to compute this GF numerically. According to (Tai (1994)), the inhomogeneous discrete version of the GF for a 2D TM scalar case, $\mathbf{G_{in}}$, can be expressed as

$$\mathbf{G_{in}} = \mathbf{G_{homo}} + \mathbf{G_{scat}} \tag{3.3}$$

Where $\mathbf{G_{homo}}$ is the GF corresponding to the homogeneous case and $\mathbf{G_{scat}}$ is the contribution of the inhomogeneous part of the structure. $\mathbf{G_{scat}}$ can be obtained combining equations 3.1. For the case of the $\mathbf{G_{c_{in}}}$ GF it can be expressed as

$$\tilde{\mathbf{G}}_{\mathbf{c_{in}}} = \mathbf{G_{homo}} + \mathbf{G_{free}}\mathbf{w_{free}}|_D \tag{3.4}$$

$$\mathbf{w_{free}} = (\mathbf{I} - \mathbf{X_{in}}\mathbf{G_{free}})^{-1}\mathbf{X_{in}}\mathbf{G_{free}} \tag{3.5}$$

Where $\tilde{\mathbf{G}}_{\mathbf{c_{in}}}$ and $\mathbf{G_{homo}}$ are defined in the smaller region D corresponding to the imaging domain defined in Figures 3.1(a) and 3.1(b)) . On the other hand, $\mathbf{G_{free}}$ and $\mathbf{X_{in}}$ are the free space discrete GF and inhomogeneous contrast, and they are defined in a region that contains the whole structure including the dielectric plates. For this reason on the $\mathbf{G_{free}}\mathbf{w_{free}}$ term we only have to take into account the pixels contained in the smaller region D. The inhomogeneous contrast has been defined with respect to the air region $\mathbf{X_{in}} = (\varepsilon(\mathbf{r}) - \varepsilon_0)/\varepsilon_0$. The GF relative to the new background permittivity, ε_b, can be obtained through multiplication by a constant term $\mathbf{G_{c_{in}}} = \tilde{\mathbf{G}}_{c_{in}}(\varepsilon_b/\varepsilon_0)$. The same procedure can be obtained to calculate $\mathbf{G_{o_{in}}}$ and $\mathbf{E_{in}^{inc}}$.

An example of this procedure is shown here and the results are compared to a simulation using CST Microwave Studio. The geometry consists on a slab of glycerine ($\varepsilon_r = 6.28$, $\sigma = 0.43S/m$), with a contour of Plexiglas ($\varepsilon_r = 2.56$, $\sigma = 0.0051S/m$). The size of the glycerine slab is 240 by 38 mm and the thickness of the plexyglass contour is 6mm. The scattering object is a rectangle of 12 by 10 mm, with an electric contrast of 2 referred to the glycerine permittivitty, located at x=0, y=10mm. The object is illuminated by 4 electric line sources located at $x = \pm 64mm$ and $y = \pm 12mm$ and the scattered field is measured at $y = \pm 30mm$ at 80 positions along the x direction (40 located at $y = -30$ and 40 at $y = 30$) with a spacing of 2mm between the measurement probes. The results obtained with equations 3.1, 3.3 and 3.4 implemented in Matlab and the finite integration time domain formulation of CST Microwave Studio are shown in Figure 3.5 both for the amplitude and phase of the scattered field. Here the four sets of 80 measurements are shown in sequence

along the horizontal axis to ease visualization. CST Microwave Studio is a 3D solver so appropriate boundary conditions are used in the simulation to represent a 2D geometry. The mesh size is dx=dy=2mm for the MoM simulation ($\Delta \approx \lambda/20$) and assigned to $\lambda/30$ in CST at a frequency of 2.45GHz. As it can be seen from the figure, the results for these two very different techniques agree very well both for the amplitude and the phase. This fact validates the approach used for the calculation of the scattering from an inhomogeneous object using an inhomogeneous Green's function. This formulation reduces considerably the size of the Green's matrices G_c and G_o and the incident electric field vector E_i^0. For instance, in the given example, the size of G_c is reduced from 3150 by 3150 elements to 1026 by 1026 elements, considering an imaging region D of 54 by 19 pixels. This has a considerable impact in the reconstructions that will be performed in section 3.5.2, since the CSI type algorithms involves a lot of matrix vector products of the quantities previously mentioned.

3.5 Results

3.5.1 SVD analysis of the configurations

The configurations shown in 3.1 will be now compared on the basis of the singular value decomposition (SVD) of the operator G_o. This is a useful technique for the analysis of different measurement setups in MT. In (Bucci *et al.* (2001)), the authors analyzed the relation between the singular values of the matrix $\mathbf{G_o}$ and the available information in the system, as well as, its relation to the quality of the reconstructions. The same technique was also used in (Crocco et Litman (2009)) to analyze different MT configurations using a metallic enclosure. It was shown, that for a given value of signal-to-noise ratio (SNR) which qualitatively corresponds to a line parallel to the x axis, a high number of significant singular values increases the amount of information available for the solution of the inverse problem. The radiation operator matrix $\mathbf{G_o}$ of size $N \times n$ admits a SVD decomposition of the form $\mathbf{G_o} = \mathbf{U}\mathbf{\Psi}\mathbf{V}^\dagger$. Where $\mathbf{U}$ and $\mathbf{V}^\dagger$ are square matrices of size $N \times N$ and $n \times n$ respectively and $\mathbf{\Psi}$ is a $N \times n$ rectangular diagonal matrix which contains a vector σ with the N singular values of the matrix $\mathbf{G_o}$.

The three configurations share the same immersion medium previously defined. The dielectric plates have the same material and thickness than in the example previously presented in section 3.4. The results for the different cases are shown in Figure 3.6. The singular values are plotted for two cases of circular configuration with radius 75mm and 100mm and for the waveguide and camera configuration for $N = 80$ Rx's. In both cases, the breast is compressed up to a value of 38mm which represents a level of compression similar to a standard mammography test (Poulos *et al.* (2003)). In the circular configuration, a homogeneous GF is used, whereas in the waveguide and camera configuration an inhomogeneous GF is considered.

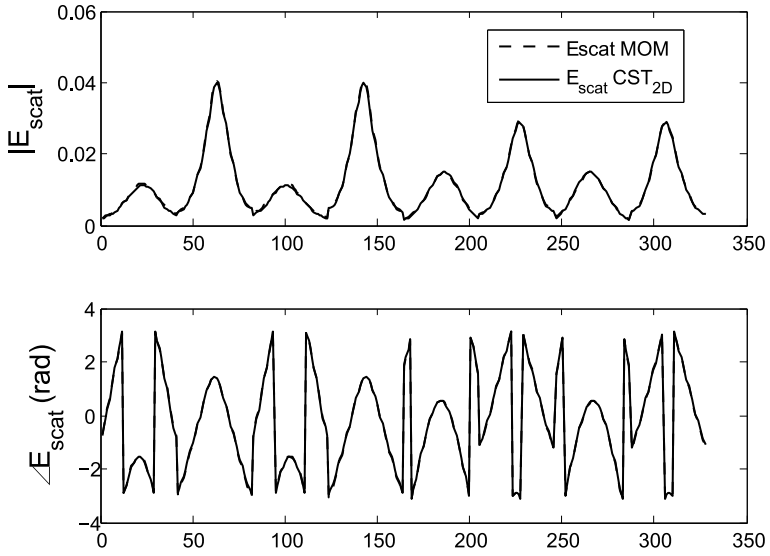

Figure 3.5 Scattering of a rectangular object using the inhomogeneous GF approach and using CST Microwave Studio.

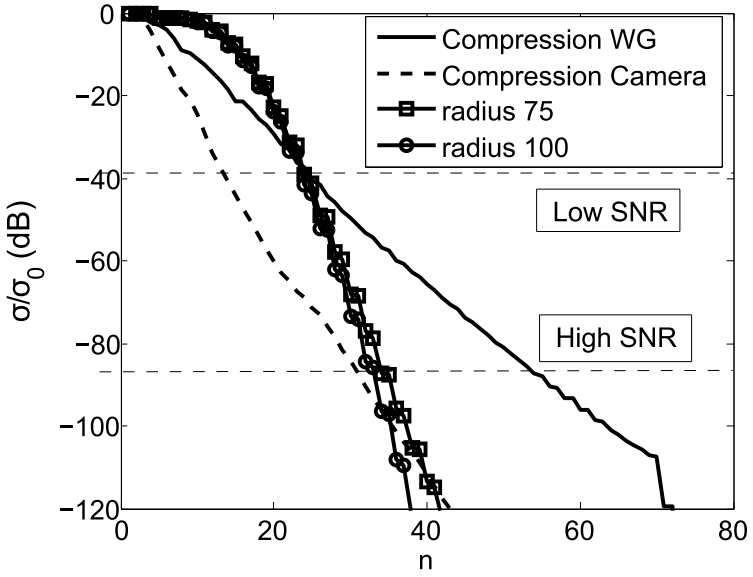

Figure 3.6 Normalized singular values of the $\mathbf{G_o}$ operator for the different configurations.

Some interesting remarks can be made based on Figure 3.6. The spectrum of the singular values for the circular configuration presents the step-like behavior described in (Bucci *et al.* (1999, 2001)). The effect of proximity, predicted in the cited references, can also be observed since more singular values are available in the case of the smaller radius configuration. It can also be observed that the camera configuration has less significant singular values than the other configurations. A possible explanation for this fact is that only transmission information

through the OUT is obtained with this configuration. The largest number of significant singular values from all of the cases is obtained with the waveguide configuration. This configuration also exhibits the slowest decay rate of singular values. Another interesting fact is the effect of the inhomogeneous background in the waveguide and camera configuration which changes the behavior of the singular values. A quasi-linear decay rate of $\log(\sigma)$ can be observed. Due to this, the compression configurations presents more significant singular values when a high SNR is available in the measurement system. However, when the SNR decreases the number of significant singular values available from the two configurations is very similar. This is an important result since one of the goals of breast compression is to have more information available in close proximity of the OUT, provided that this additional information is not hidden in the noise or measurement errors.

3.5.2 Reconstruction of the numerical Phantoms

In order to confirm the results obtained from the SVD analysis of the $\mathbf{G_o}$ operator, now we will reconstruct the three proposed phantoms with and without compression using the waveguide and circular configurations respectively and for different levels of SNR. The synthetic measured data are generated using a MoM code and Gaussian noise is added to the scattered field to represent experimental conditions. The CSI algorithm of (Barriere *et al.* (2011)) is used and the results of the reconstructed images are compared after 2000 iterations.

As it was previously mentioned in Section 3.2, the number of independent illuminations that can be generated with the waveguide configuration is limited to the number of independent modes that can propagate in the structure. The number of modes can be calculated using the transmission matrix method described in (Schlereth et Tacke (1990)). Wave propagation is considered along the x direction with the electric field oriented in the z direction (i.e. TE modes in the terminology of the cited reference). For a multilayer structure composed of a slab of the immersion medium described in Table 3.1 of thickness 38mm, compression plates of plexyglass ($\varepsilon_r = 2.56$ and $\sigma = 0.005 S/m$) of thickness 6mm and the outer air region, there is a total of three independent modes propagating (i.e. above cut-off) at the frequency of operation, $2.45 GHz$. From this result the number of transmitters is fixed to $M = 6$ and the number of receivers will be fixed to $N = 80$, with half of them located at $y = -30$ and the other half at $y = 30$ for the waveguide structure. These receivers are located 5mm above and below the compression plates. For the circular structure, the number of transmitters and receivers are the same, however in this case they are equally spaced around a circumference of 75mm radius.

The reconstructions of the OUT shown in Figure 3.4 for two different values of the SNR are shown in Figs. 3.7 and 3.8, and the MSE of the different cases is shown in Tables 3.2 and

3.3. These results agree with the previous conclusions obtained about the spectrum of singular values. As it can be seen from the figures and tables, the compression of the breast allows an enhancement of the reconstructed images when the number of transmitters and receivers is unchanged. This fact is true provided that we can accurately measure the scattered fields with a large SNR (i.e. 40dB). This value of SNR has been previously achieved in state of the art measurement systems (Henriksson *et al.* (2010)) in which the field measurement are done in close proximity of the OUT. When the SNR is reduced to 10dB, the evanescent component of the scattered field is masked by the noise and no enhancement in the reconstructed images was observed. Several cases have been tested in our particular case and it has been found that the quality of the reconstruction results starts to degrade for a SNR of 20dB or smaller for the waveguide configuration.

The reconstructions for the circular configuration can be enhanced by increasing the number of independent illuminations. For the particular case of the fibroglandular phantom, the reconstructions were repeated for different number of Tx antennas. It was found that for 12 illuminations the quality of the reconstructed images was similar to the values reported using the waveguide configuration. Further increments of the number of Tx antennas did not improve the quality of the images in terms of the MSE. Finally, the number of independent illuminations for the waveguide configuration was limited to the number of propagating modes in a 2D case. Moreover, considering the small distances between the transmitters, receivers and OUT, the excitation of evanescent propagating modes (below cut-off) could also be considered to increase the number of independent illuminations.

Table 3.2 MSE of the different reconstructed phantoms for $SNR = 40dB$. $N = 80$, $M = 6$ and $n = 32 \times 32$ and $n = 54 \times 19$ pixels for the compressed and uncompressed case.

Phantom	Compression	No Compression
Mostly fatty	0.093	0.169
Scattered Fibro	0.2773	0.4088
Very Dense	0.1438	0.2141

3.5.3 Effect of the compression plates in the reconstruction capabilities

In this section, the effect of the compression plates will be analyzed. Apart from the breast tissues, there are three media present both in the camera and waveguide configuration : the immersion medium, the compression plates and the surrounding air where the measurement takes place. Usually, there is a large difference in permittivity between the air and the immersion medium, and this medium is specifically chosen to couple the maximum energy inside the

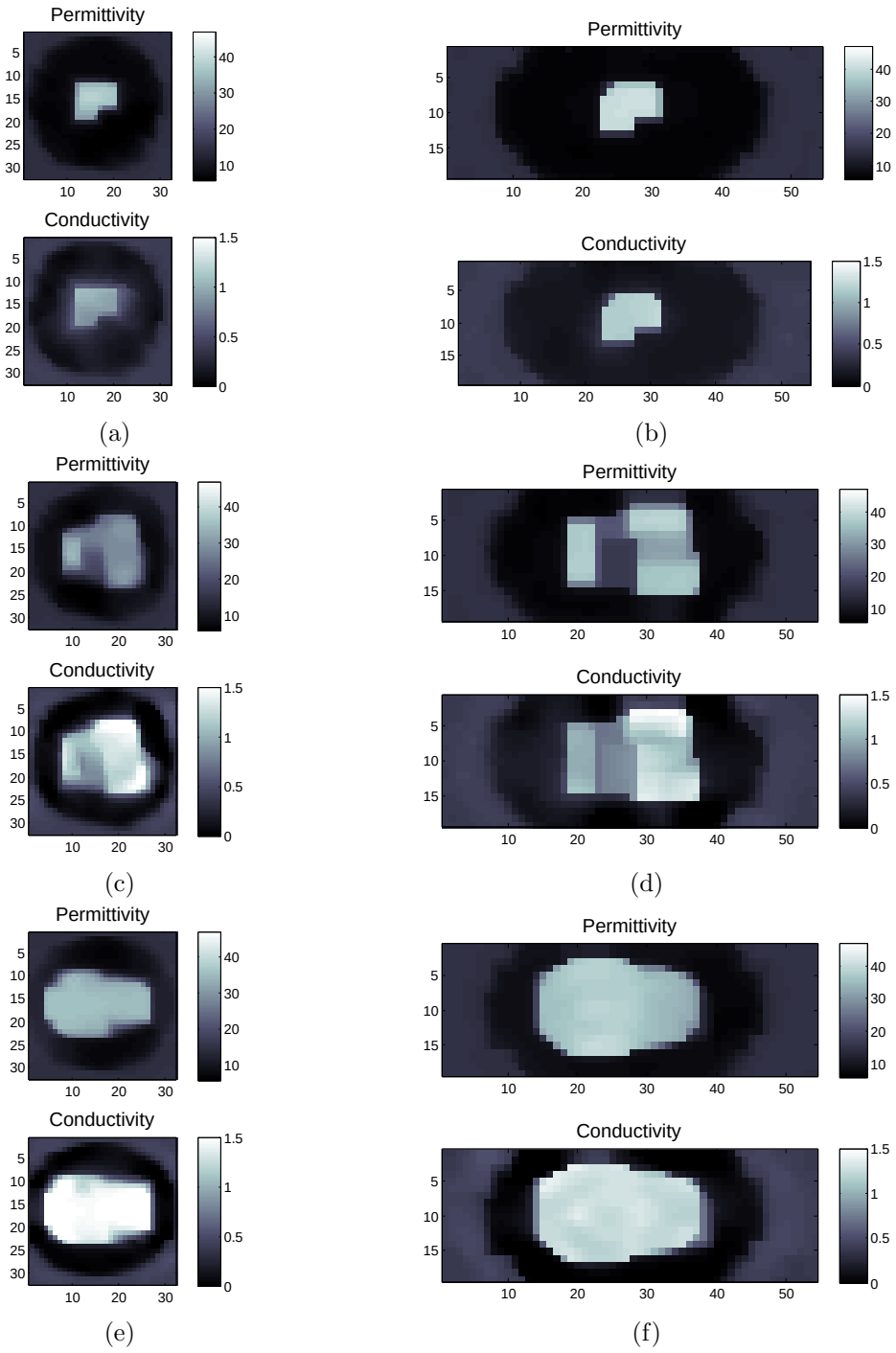

Figure 3.7 Reconstructions for the different phantoms for a SNR of 40dB. (a) (b) Mostly fatty phantoms. (c) (d) Scattered fibroglandular phantoms. (e) (f) Very dense phantoms.

breast. In principle it could be possible to enhance the quantity of scattered field transmitted to the air region by an appropriate choice of the thickness and electrical properties of the compression plates. For this purpose the SVD decomposition will be performed for different

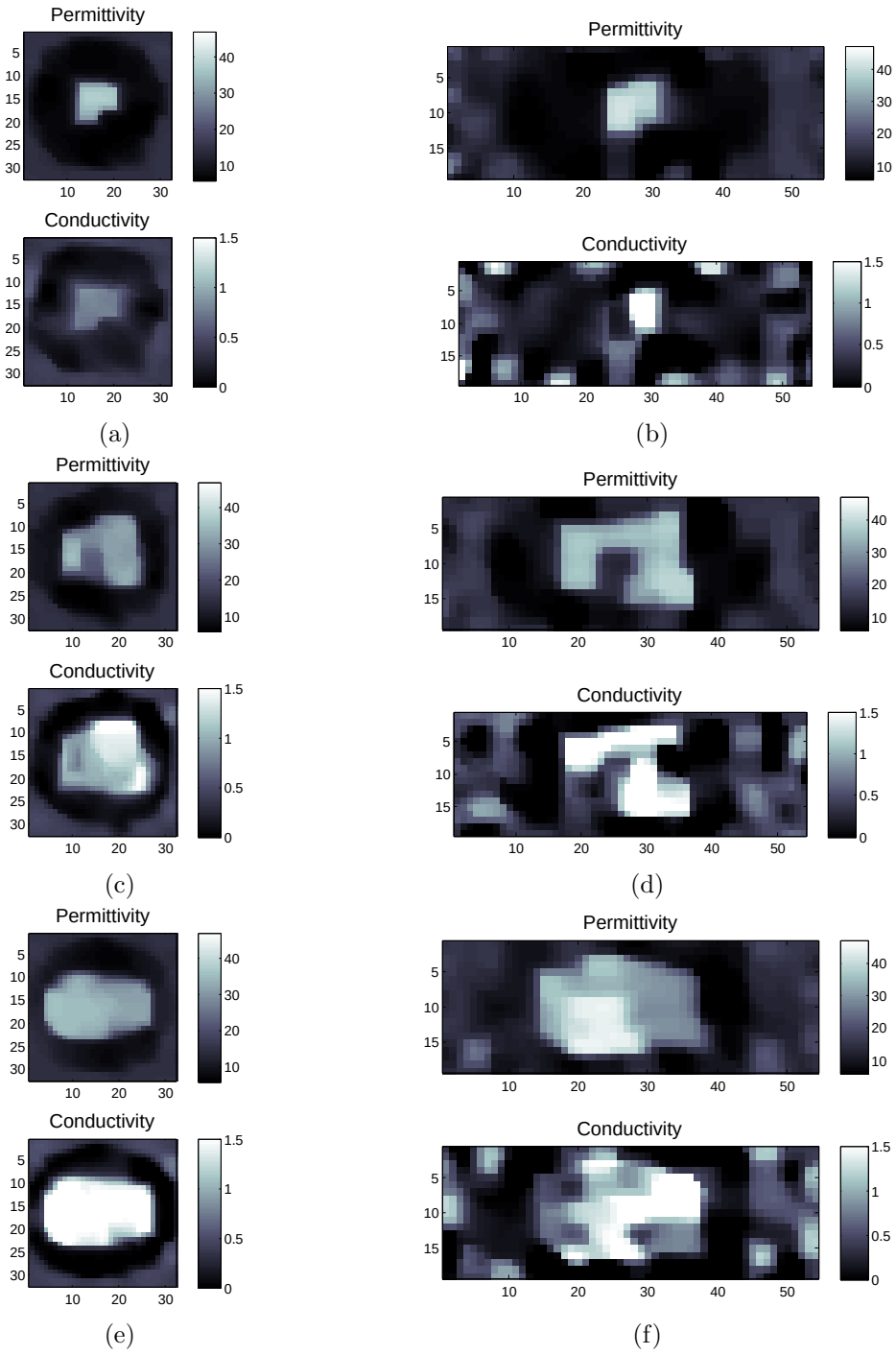

Figure 3.8 Reconstructions for the different phantoms for a SNR of 10dB. (a) (b) Mostly fatty phantoms. (c) (d) Scattered fibroglandular phantoms. (e) (f) Very dense phantoms.

thickness and permittivity values of the compression plates.

The SVD analysis for the waveguide configuration is shown in Figure 3.9. Figure 3.9(a) shows the spectra of singular values for different thicknesses of the compression plates made

Table 3.3 MSE of the different reconstructed phantoms for $SNR = 10dB.N = 80$, $M = 6$ and $n = 32 \times 32$ and $n = 54 \times 19$ pixels for the compressed and uncompressed case.

Phantom	Compression	No Compression
Mostly fatty	0.3343	0.1993
Scattered Fibro	0.456	0.4034
Very Dense	0.2967	0.1889

of dielectric material with $\varepsilon_r = 2.56$ and $\sigma = 0.005S/m$ and using the immersion media defined in 3.1 ($\epsilon_r = 15$, $\sigma = 0.4S/m$). Figure 3.9(b) shows the variation of the singular values for different values of ε_r for a constant thickness of 6mm. The position of the receivers is always kept at a distance of 5mm of the top and bottom plates. As it can be seen from the figures, the thickness of the plates impacts on the decay rate of the singular values, whereas the permittivity of the plates produces essentially no effect. From this result we can conclude that the plates should be kept as thin as possible in order to place the receivers as close as possible to the OUT.

3.6 Conclusion

In this chapter we have analyzed different configurations for the MT problem based in breast compression. These configurations were designed in the context of creating a compact measurement setup that can be easily integrated with a standard mammography apparatus. The different configurations were compared based on the SVD of the radiation operator and through the reconstruction of several breast-like objects with and without compression using synthetically generated measurements for different levels of SNR.

– It has been shown that an enhancement in the quality of the reconstructed images can be obtained using a breast compression based measurement configuration compared to a classical circular MT measurement system for the same measurement conditions (i.e. equal number of Tx and Rx antennas and same SNR level). This enhancement is due to the measurement configuration in a compressed breast, where the Rx's can be placed in close proximity to the scatterers, and thus allows better measurement of a more significant portion of the evanescent scattered fields spectrum. In other words, it is possible to acquire more information from the scattered field variation. It was shown that the enhancement is dependent on the SNR level, which will determine if the information from the evanescent scattered fields is not hidden in the measurement noise. In our case, it was found that a SNR of 20dB or better was needed for an enhancement in the quality of the reconstructions. However due to the non-linearity of

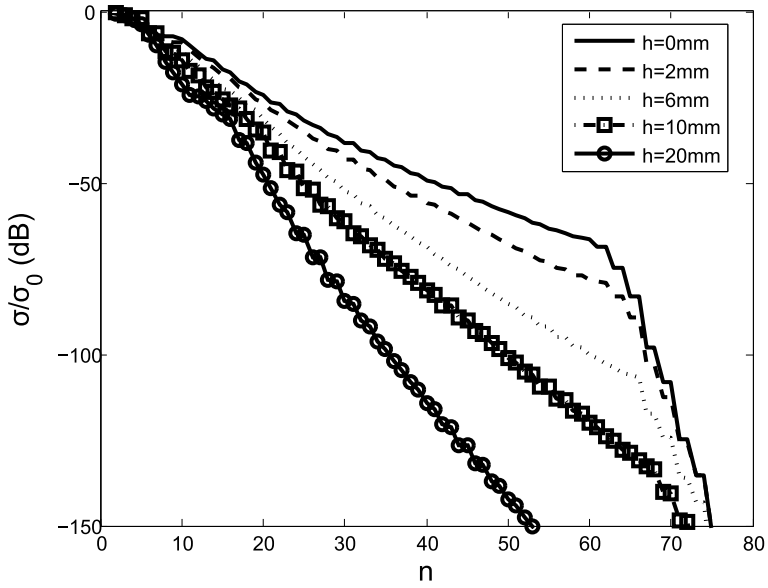

(a)

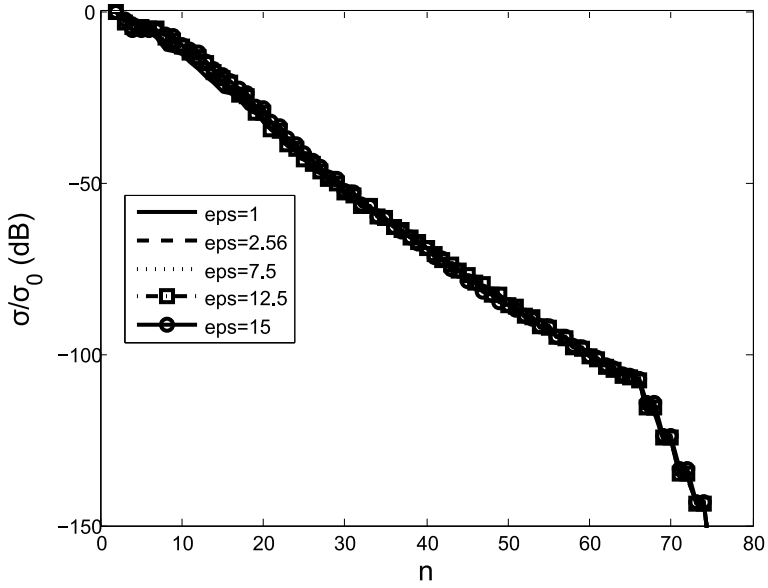

(b)

Figure 3.9 SVD analysis of the effect of the compression plates (a) Thickness variation (b) permittivity variation.

the inverse scattering problem, this threshold value may be dependent on the geometry of the configuration, the frequency of operation and the particular algorithm used for the solution of the inverse scattering problem.

– The waveguide configuration has shown a higher potential of reconstruction than the camera configuration since this latter can only provide information about transmission

through the OUT, resulting in a limited view of the scattered field.

– An efficient way to treat the inhomogeneous background of the breast compression configurations based on the calculation of the inhomogeneous Green's function has been presented. The computation of this Green's function is performed numerically and its reduced size allow a significant reduction both in terms of memory and computer time needed to solve the inverse scattering problem.
– The reconstruction of simple breast-like models was performed with and without compression where only the fat portion of the breast was deformed, taking into account the results from a simplified mechanical simulation of the breast tissue deformation. An interesting study could be performed by using realistic numerical phantoms available in the literature and applying a non-linear formulation for the mechanical deformation that allows large deformations.

CHAPTER 4

Near-field measurement setups for planar Microwave Tomography

4.1 Near-field measurement techniques

In the previous chapter it has been discussed how the measurement of the evanescent scattered fields can enhance the quality of the reconstructed images in MT. The different possibilities for implementing a planar MT system were also briefly discussed in section 3.2. It was mentioned that measuring the evanescent scattered field of an OUT requires to set the measuring probe or antenna very close to the object, which in turn will disturb the field that we want to measure. Moreover, the scattered field is obtained as the difference of two measurements of the total and incident fields and its amplitude is in general much weaker compared to the total field or incident field (i.e. up to 30dB in the case of the waveguide configuration) which poses a major challenge for the measurement system.

In general, near-field measurements always represent a trade-off between sensitivity and accuracy. There are different types of near-field measurement techniques which can be divided into direct and indirect techniques (Memarzadeh-Tehran (2010)). Among direct techniques we can cite detector loaded probes (Smith (1981)), electro-optic probes (Suzuki *et al.* (2008)) and classical probes (Elasoued (2004)). Detector loaded probes consist typically in a small antenna loaded with a diode that rectifies the high frequency signal and generate a DC voltage proportional to the amplitude of the electric field. The signal is then transmitted through resistive wires to the measurement equipment. This approach is only capable of measuring the amplitude of the electric field, although phase information can be retrieved by performing several measurements and applying post-processing techniques. Electro-optic probes generally consist in a small antenna loaded with a non-linear crystal which is illuminated using light at a predetermined wavelength. The refractive index of the crystal changes in the presence of an electromagnetic field and the phase of the light passing through the crystal will experience a phase shift proportional to the EM field. Finally these phase variations are detected using an optical detector. In principle, this setup can measure both magnitude and phase of the EM field with minimal perturbation, however it presents several drawbacks. Among them we can cite the long warm-up time to synchronize the laser and the optical receiver, the low sensitivity of the system that requires a sufficiently high signal to detect the change in the phase of the optical signal and the cost of the system. Finally, classical probes typically consist in a small antenna connected by a transmission line to a VNA, in this case the EM

field at the position of the probe is directly proportional to the measured S_{21} parameter. This procedure has the problem that the currents induced in the transmission line, typically a coaxial cable, can perturb the EM field to be measured.

Indirect techniques typically include perturbation techniques and the Modulated Scattering Technique (MST). A perturbation technique is an indirect way of measuring an EM field, it consists in placing a small scatterer in the region where the field has to be measured, for instance in front of the OUT. A scattered field proportional to the local field at the position of the scatterer is reflected back to the OUT or to an auxiliary device. The measured field is then obtained substracting the reflected or transmitted signal in two different states of the scatterer. In this technique, the scatterer has to be sufficiently small in order to not disturb the field in excess of a tolerated limit. This fact makes the scattered signal very small and difficult to measure or distinguish from other interferences. A possible solution to increase the sensitivity of the measurement system using an indirect technique is to add a feature to the scattered signal that the receiver can recognize. The implementation of this technique is known as the MST, it consists in modulating the scattered field in a way that the modulated signal can be detected using an homodyne receiver.

4.1.1 The Modulated Scattering Technique

As previously stated, the MST is an indirect measurement technique for EM fields in the microwave frequency regime. A schematic of a general MST measurement procedure is shown in Figure 4.1. The objective is to measure a field distribution generated by an OUT which acts as transmitter. A near-field probe loaded with a non-linear element, typically a diode, is scanned around the OUT. At the same time this non-linear element is switched on and off at a modulation frequency f_m, where f_m is much smaller that the measurement frequency or carrier frequency f_c. The probe will scatter a field proportional to the actual value at the position of the probe, this modulated scattered field can be detected using an auxiliary receiver antenna (bi-static mode) or from the antenna generating the measured field distribution (mono-static mode) plus a coherent receiver capable of measuring both amplitude and phase of the EM field. Another alternative, is to use a VNA as the measurement instrument, where in that case, the electric field will be proportional to the difference of two S parameter measurements $E \propto \delta S_{ij} = S_{ij}^{ON} - S_{ij}^{OFF}$ (i.e. S_{11} and S_{21} for a mono-static or bi-static implementation respectively) (Ostadrahimi *et al.* (2012)).

The modulation can be implemented using electrical, mechanical or optical mechanisms. The most popular approaches are the electrical and optical modulation, using a PIN diode or a photodiode respectively as a non-linear element. The electrical approach is usually implemented using resistive wires to modulate the pin diode whereas in the optical approach the

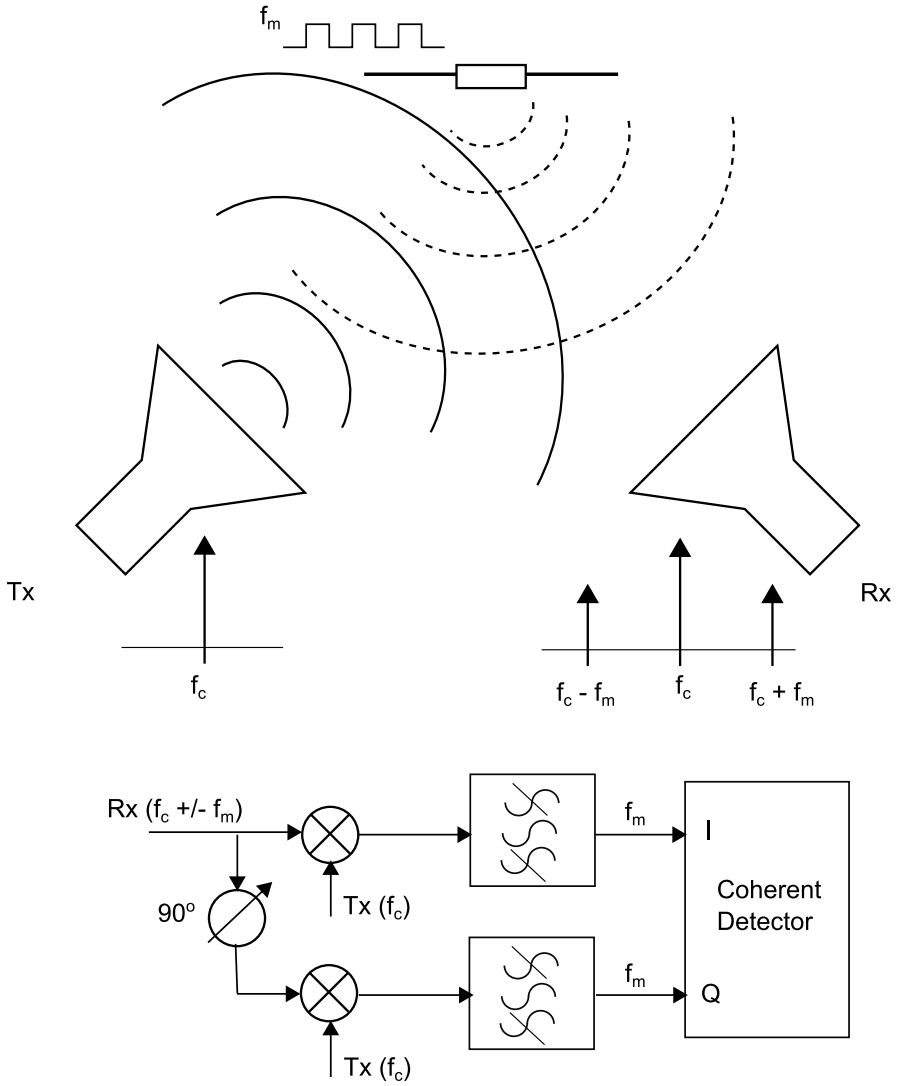

Figure 4.1 Schematic of the measurement principle using the modulated scattering technique.

light to modulate the photodiode is coupled using an optical fiber. Each of the approaches has its advantages and disadvantages. Electrical modulation is easier to implement and less expensive. On the other hand optical modulation provides an almost perturbation-free measurement, since the optical fiber is transparent to the EM field. The probe is however more expensive and difficult to fabricate.

4.1.2 Classical Near-field Measurements vs Modulated Scattering Technique

It was previously discussed how MST can provide accurate EM field measurement without perturbation. However this low perturbation comes at the expense of a reduced sensitivity in the measurement. Previous work in the field of MT include work using both classical

(Omrane *et al.* (2006)) and MST near-field measurement systems (Franchois *et al.* (1998); Henriksson *et al.* (2010)). In both cases, the measured scattered fields require appropriate calibration (Ostadrahimi *et al.* (2011)) or a modified formulation to include the sensors effect in the reconstruction model (Franza *et al.* (2002)).

Previous work in our research group included the design of OMS probes which allow perturbation free measurements. One of the objectives of this work will be to determine if this approach represents an advantage for simplifying the calibration algorithms. This point will be addresed in Chapter 5. On the other hand, the MST technique requires the implementation of a custom homodyne receiver whereas a classical near-field measurement is usually performed using a VNA, this issue will be also discussed in next chapter.

4.2 Design of a non-invasive wideband OMS probe

Previously it was mentioned that one of the drawbacks of the MST technique is the reduced sensitivity of the measurement. One solution for increasing the sensitivity of small probes is to add a tuning network to the probe to make it resonant and thus increase the modulation index of the probe(Bolomey et Gardiol (2001)). The modulation index, m, in the case of a small resonant probe can be defined as :

$$m \approx \frac{\|Z_{ON}\| - \|Z_{OFF}\|}{\|Z_{ON}\| + \|Z_{OFF}\|} \tag{4.1}$$

Where Z_{ON} and Z_{OFF} are the impedances of the modulated load in the ON and OFF states. This fact was used by our research group to create a resonant optically modulated probe at the frequency of 2.45GHz (Memarzadeh-Tehran *et al.* (2010)). The goal was to create a small dipole probe ($L = \lambda/12$) loaded by a photodiode to create a minimally invasive near-field probe. Both the photodiode and the antenna can be modelled as series RC circuit, then, by adding an inductance in series with the probe, it can be made resonant at one frequency of operation. The measured bandwidth of that probe, defined as the band over which the sideband level remains within 20 dB of its maximum value, was limited to the range 2 to 3.2GHz (46% bandwidth, normalized to the center of the band). This bandwidth is not sufficient in many applications. Here a new design published in (Memarzadeh-Tehran *et al.* (2011)) which includes an improved tuning circuit providing significantly enhanced bandwidth will be shortly presented. The equivalent circuit of the proposed probe is shown in figure 4.2.

It can be shown that the probe bandwidth is directly related to the order of the tuning network used. Using a higher-order tuning network will improve the bandwidth, however, it will also lower the dynamic range of the probe. The criteria leading to a proper selection of

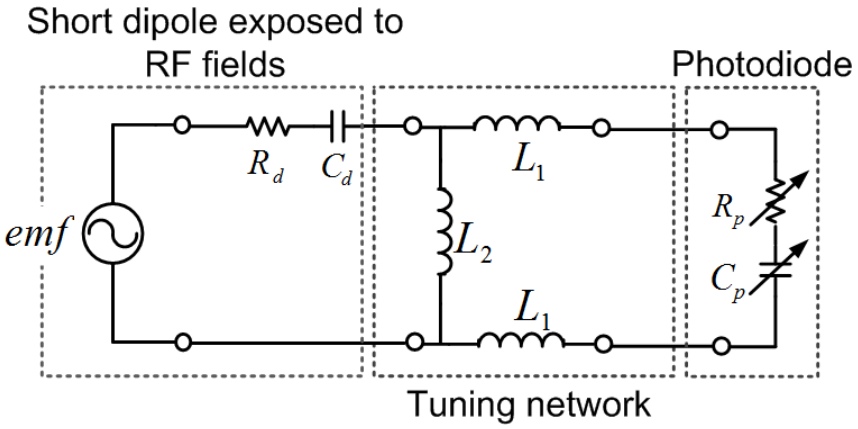

Figure 4.2 Circuit model of proposed OMS probe with second order tuning network.

tuning network can be summarized as follows : 1) its input impedance should be inductive as the impedance of the short dipole is significantly capacitive, 2) the tuning network should apply a DC short-circuit across the probe photodiode to prevent voltage rectification, which can decrease the modulation index of the probe (Memarzadeh-Tehran *et al.* (2011)), 3) it should provide a large modulation index over a wide band. The photodiode used in the construction of the OMS probe is a nonlinear device.

Figure 4.2 demonstrates the equivalent circuit of the proposed probe incorporating the tuning network which meets the requirements listed above. The tuning network consists of three inductors (i.e., two of value L_1 and one of value L_2) where two of them are on each arm of the dipole and the third is across the arms. The last inductor stabilizes the probe modulation depth by imposing a zero DC voltage across the photodiode (short-circuit). Based on a simple RC network model of the photodiode, the tuning network parameters were optimized by maximizing the difference of the current flowing through the dipole antenna in ON and OFF states, to achieve the highest value of m over 1–5 GHz band. For a PDCS12T photodiode, manufactured by Enablence Co, the measured input impedance of this photodiode at 2.62 GHz is $Z_{OFF} = 26.12 - j377.3\Omega$ and $Z_{ON} = 21.94 - j12.96\Omega$. The optimization results yield $L_1 = 12.5\ nH$ and $L_2 = 18\ nH$. The implementation of the inductive loads between the photodiode/short-dipole and the photodiode's terminals is illustrated in Figure 4.3. Simple planar spiral inductors are used and wire bonds are made between the photodiode and the central landing pads. They are also connected to the printed dipole antenna.

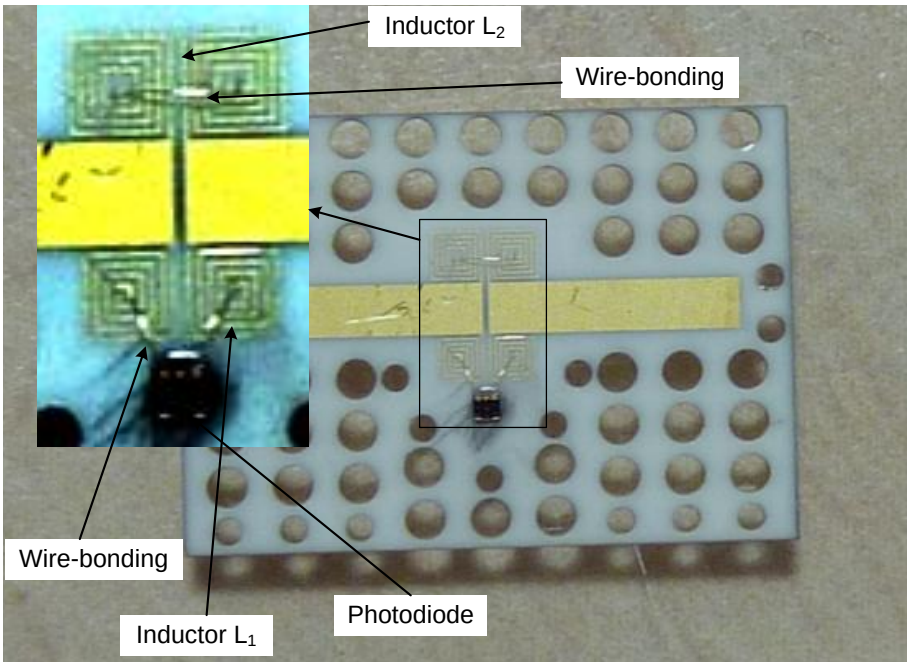

Figure 4.3 Photograph of the developed OMS probe (the length of the printed dipole is 10mm). Close-up view of the probe before fiber coupling and complete assembled probe (upper-left corner).

4.2.1 The OMS probe non-invasiveness improvement

The probe was fabricated on an alumina ceramic substrate using a Miniature Hybrid Microwave Integrated Circuits (MHMIC) process. This technology was used due to the precision requirements for implementing the spiral inductors of the tuning network. The high permittivity of alumina (i.e. ϵ_r= 9.9) may cause perturbation on the fields to be measured, thus several holes were performed on the alumina substrate using a michomachining laser technique to reduce the effective permittivity. In order to quantify this effect, two experiments were simulated using a full-wave electromagnetic commercial code (CST Microwave Studio). The first experiment, shown in figure 4.4 consisted of measuring the scattered field by the short-circuited probe for a linearly polarized plane-wave illumination. The origin is located in the middle of the probe and the scattered field is measured in a line along the y-axis and at a distance of 10mm away from the probe in the z direction. The second experiment consisted of measuring the transverse electric field of a 50 Ω microstrip line using the implemented MST probe. The probe was located 3mm above the trace and the equivalent lumped element circuit of the photodiode was placed between the two arms of the dipole. For each point, the measured electric field at the probe position was obtained using the following expression $E \propto \Delta\rho = \sqrt{S_{11_{ON}} - S_{11_{OFF}}}$ (Bolomey et Gardiol (2001)), where S_{11} was obtained at port 1

of the microstrip line while port 2 is matched to a 50 Ω load. Two different simulations were made with the photodiode in the ON and OFF states.

Both simulations were performed for three different cases : first, using the actual dimensions of the alumina substrate, second, using the same substrate with perforated holes and finally, without the substrate, except for a portion under the dipole arms. The results for the three cases are plotted in Figure 4.5 for the scattered field by the short-circuited probe and in figure 4.6 for the microstrip experiment. One can see in Figure 4.5, that the substrate has an effect on the field scattered by the probe which is directly related to the field measured by the probe itself using the MST technique. The curves for the cases without substrate and with the perforated substrate agree very well with each other, however for the case with the whole substrate there is a difference of up to 3dB between the curves. It can be seen that the presence of the substrate does affect the distribution of the scattered field. For instance, the difference between cases of the perforated and non perforated substrate at y=0 is about 3 dB and it decreases to about 1 dB at y ±40. The same effect is observed for the second experiment, where the curve for the perforated case is close to the curve in the case without the substrate, as already expected. In the design procedure, the substrate was kept as small as possible. However, it cannot be removed completely due to the need for physical layout of the inductors, photodiode and dipole.

4.2.2 Frequency response and validation of the probe

Frequency response

The impact of the tuning network on the frequency response of the probe was investigated by conducting an experiment with the following arrangement. A 50-Ω microstrip transmission line was fabricated on a RO3265 substrate, fabricated by the Rogers corporation, with thickness of 60 *mil*. In this experiment, the OMS probe was positioned as close as possible to the transmission line (terminated in a matched load) where a maximum of the E-field occurs. Then, the stationary probe was light-modulated and the generated sideband levels were recorded at different frequencies (i.e., $f_{RF} \pm f_{IF}$, where f_{IF} is modulation frequency). The signals at the input port of the transmission line include both the carrier and the sideband signals. The frequency response of the probe was obtained by reading the sidebands power level on a spectrum analyzer when the frequency was varied from 500 MHz to 5 GHz. Figure 4.7 shows the frequency response of the probe. As it can be seen in the figure, the $20dB$ bandwidth of the probe covers the frequency range 1.1 to 3.6GHz (106%). For comparison, we also included the frequency response of the probe previously developed by the authors (Memarzadeh-Tehran *et al.* (2010)) in the same figure. The simulated frequency response of

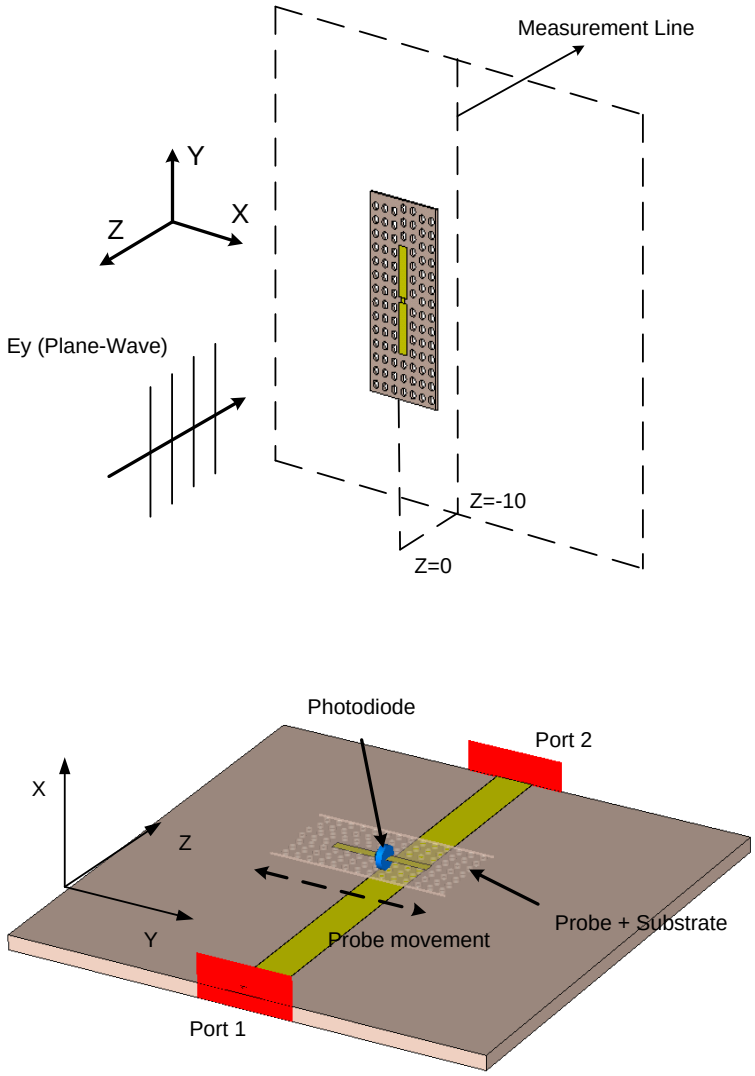

Figure 4.4 Simulation models in CST for the two experiments.

the probe obtained using the equivalent circuit of the probe is also shown. The simulated frequency response obtained using the equivalent circuit of Figure 4.2 is also shown. In this crude model, we did not include parasitic components for the planar inductors. The antenna impedance is modelled with a simple capacitor, and the photodiode by simple RC networks in both states. As a result, it can be seen that the accuracy of the prediction degrades as the frequency increases, leading to a difference of 250 MHz between the measured and simulated peak frequencies. Nevertheless, both simulated and measured characteristics clearly show significant improvement compared to the previous probe.

The sensitivity of the probe can be estimated using the ratio of the probe current in ON

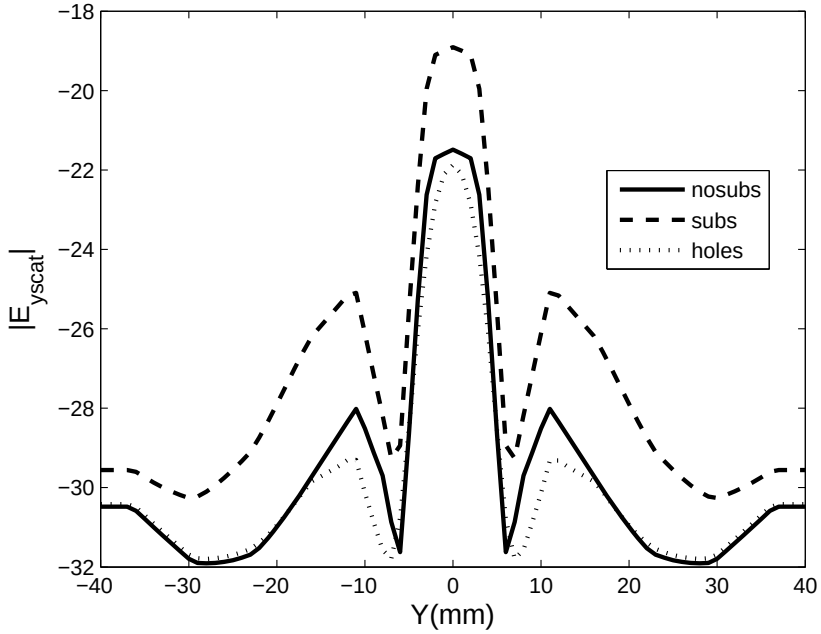

(a)

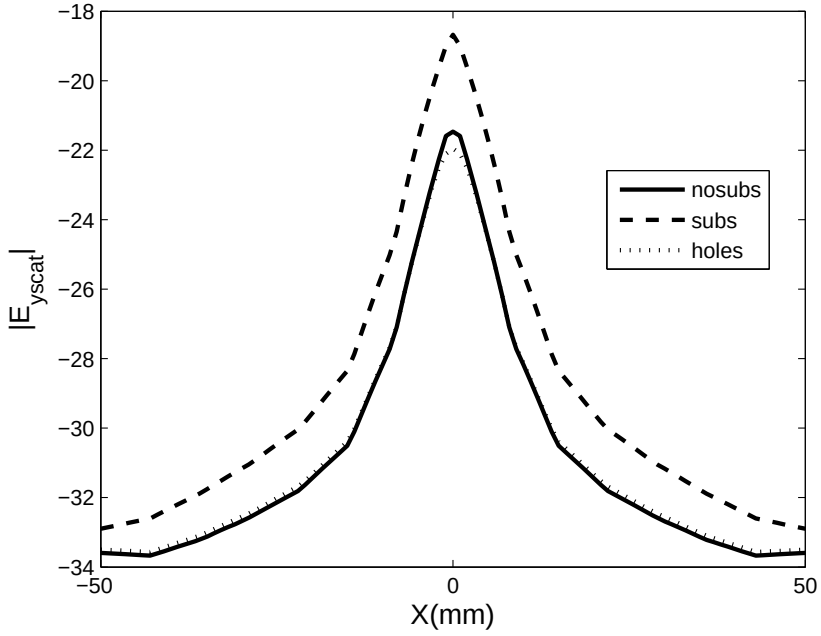

(b)

Figure 4.5 Scattered field by the short circuited probe under plane wave illumination for the two different cases. (a) X=0 Line. (b) Y=0 Line.

and OFF states ($CR = |I_{ON}|/|I_{OFF}|$). The CR value of this probe, compared to that of the

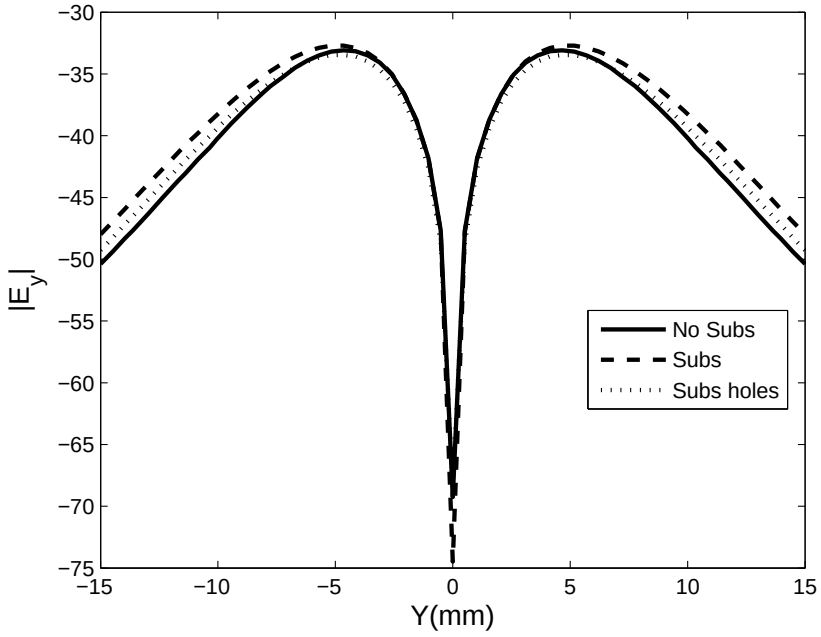

Figure 4.6 Simulation of the EM field of the microstrip line using the MST principle.

probe proposed in (Memarzadeh-Tehran *et al.* (2010)), showed an improvement of about 18 dB at the peak frequency. This enhanced sensitivity is due to the fact that a different type of photodiode was used. Moreover, there is no loss of sensitivity associated with DC voltage rectification in the new probe.

4.2.3 Probe measurement results assessment

The operation of the developed OMS probe in measuring electric field was investigated by scanning the transverse E-field distribution of the transmission line used in Section 4.2.2 at different frequencies. To do this, the probe was mounted on a planar positioning system and scanned across the line at a distance of 3 mm ($\lambda/40$) above the trace. The E-field magnitude measured using a spectrum analyzer where the magnitude of the E-field is read from the sideband power level. Comparisons with numerical simulations done with CST are shown in Figure 4.8. A very good agreement can be noticed. It can be seen that the dynamic range was limited in these measurements, which is due to the noise in the spectrum analyzer.

4.3 Practical implementation of the Dielectric Waveguide configuration

In this section, we will present the practical implementation of the dielectric waveguide configuration previously explained in Chapter 3. Two different antennas capable of launching

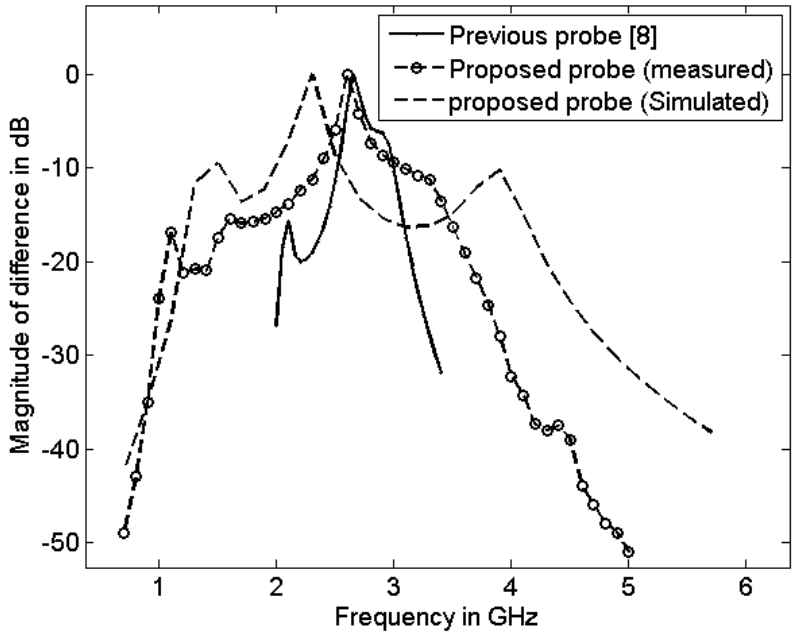

Figure 4.7 Frequency response of the proposed probe measured by reading the sideband level using a Spectrum Analyzer.

the different modes independently are designed and measured. A method for measuring the surface waves and the scattered field from cylindrical objects placed inside the waveguide is also presented. These measurements are performed using an optically modulated probe previously presented and good agreement between the measured and simulated results is obtained. The content of this section is adapted from a paper submitted to IEEE Transactions on Microwave Theory and Techniques.

4.3.1 The Dielectric Waveguide Configuration

A 2D cut of the configuration considered in this section, and which was previously introduced in Chapter 3, is shown in Figure 4.9. In this case, the breast is compressed between two dielectric plates in a setup very similar to X-ray mammography. The structure is laterally closed to allow the utilization of a matching fluid, in order to maximize the energy coupling inside the breast. The compound structure formed by the immersion medium, the enclosure formed by the dielectric plates and the surrounding air region can be seen as a multilayer dielectric waveguide. The guiding effect concentrate the fields in the region of interest and if there is an inhomogeneity, the scattered fields can be measured above and below the whole structure.

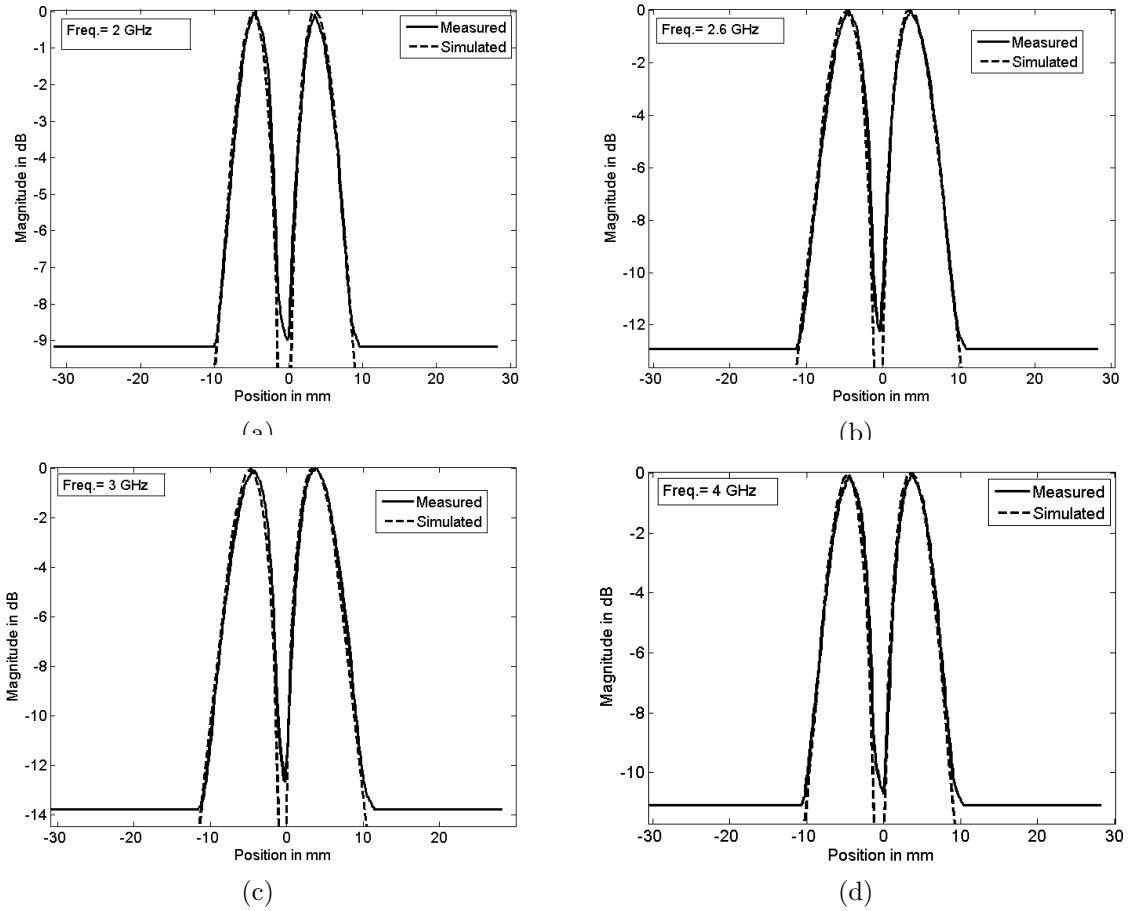

Figure 4.8 Measured and simulated transverse E-field of the microstrip transmission line at a distance of 3 mm at different frequencies ; (a) 2 GHz ; (b) 2.6 GHz ;(c) 3 GHz ; (d) 4 GHz.

This waveguide is capable of guiding different TE (E_x, H_y and H_z) or TM (H_x, E_y and E_z) modes depending on the frequency of operation, the dielectric properties of the immersion media and dielectric plates and the thickness of the different layers. In the particular case analyzed in this section, glycerine is used as the immersion media and the dielectric enclosure is made of plexyglass. The complex permittivity, i.e. relative permittivity and conductivity, of these materials was measured using a HP85070B dielectric measurement probe. The measured values are $\varepsilon_r = 7.1$, $\sigma = 0.45 S/m$ and $\varepsilon_r = 2.56$, $\sigma = 0.008 S/m$ for glycerine and plexyglass respectively at the test frequency of 2.45 GHz. The constructed phantom that will be later used in Section 4.3.3, is shown in Figure 4.10. From this phantom, we can form an equivalent dielectric waveguide and determine the number of modes propagating inside along the z axis. The waveguide is formed by 5 layers (air, plexyglass, glycerine, plexyglass and air) where the thicknesses of the glycerine and plexyglass layers are 40 mm and 6 mm respectively. The thickness of the glycerine layer was chosen accordingly to standard compressed

breast thicknesses values commonly used in mammography (Poulos *et al.* (2003)), whereas the thickness of the plexyglass layer, as shown in (Diaz-Bolado *et al.* (2011a)), should be kept as small as possible in order to enhance the level of scattered field measured. The final value was chosen considering the available materials for the construction of the phantom.

The number of modes in the structure, their propagation constants, as well as, their field distributions can be computed using different techniques, such as the Transverse Resonance method (Sorrentino (1989)) or the Transmission Matrix (TxM) method (Schlereth et Tacke (1990)). In our case, the TxM method has been use to calculate the parameters of the equivalent dielectric waveguide (the details of the method are explained in Annex B). As an example, the E field of two different TE modes propagating in the structure are shown in Figure 4.11. As it can be seen from the figure, the propagating modes have very different field distributions in the region between the plates. This fact is very useful in the solution of the MT problem because a number of dissimilar illuminations is required. Another salient feature is the very fast attenuation of the guided waves in the z direction, which is essentially due to absorption in the glycerin.

4.3.2 Surface wave launcher design

Once the guided modes and their field distributions are known , the next step is to develop a method to excite each mode independently in the waveguide. The excitation of surface waves is a well known effect in printed antennas or arrays. It is generally considered as an adverse effect and it has been extensively studied to provide design guidelines to enhance the efficiency of printed antenna arrays (Alexopoulos *et al.* (1983); Eleftheriades et Qiu (2002)). On the other hand, surface waves are intentionally excited in order to launch a guided mode in a dielectric waveguide in some applications. Among them, we can cite the implementation of spatial power combiners (Perkons et Itoh (1997); Perkons *et al.* (1998)) or planar leaky wave antennas (Podilchak *et al.* (2009)).

The excitation of a given surface wave mode requires an antenna producing a field having the same polarization as the mode that we want to excite, and placed as close as possible to the maximum of the field distribution of the desired mode (Perkons *et al.* (1998)). A surface wave launcher (SWL) has been designed for the dielectric waveguide presented in the previous section. For both the TE and TM cases there are two modes propagating in the structure, for the specified layer thicknesses and permittivities. As it will be shown, we can launch the modes using an array of two antennas and varying the phase shift between them. In our case, we want to launch modes having very different field distributions (see Figure 4.11). Mode TE_0 has a maximum in the middle of the slab, whereas mode TE_1 has a minimum in this position and maximum near the dielectric plates. The two antennas will be placed in between

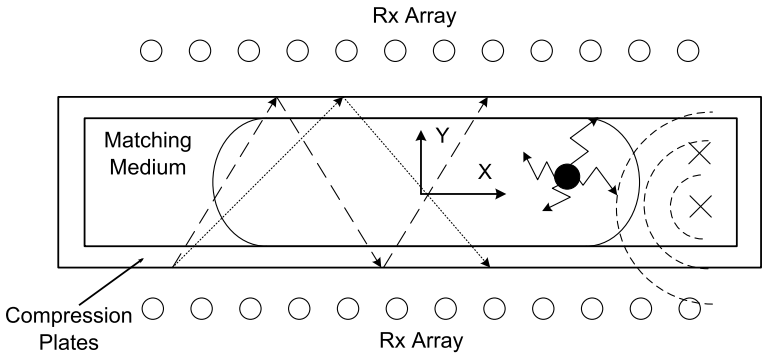

Figure 4.9 Schematic of the waveguide configuration for the MT problem.

the maximum of the different modes in order not to compromise the launching of any of the modes.

The TE modes are excited using an antipodal dipole antenna, fabricated in Rogers 6010 substrate ($\varepsilon_r = 10.2$, $tan\delta = 0.0023$) with thickness $h_{subs} = 1.27mm$. The arms of the dipole are parallel to the x axis. The antenna is designed using a full-wave simulator, CST Microwave Studio. The critical design issue of this type of antenna is the balanced excitation. In our case, the structure is fed from a microstrip line using a tapered microstrip balun (Stutzman et Thiele (1998)). It has been designed to operate directly in contact with glycerine inside the phantom shown in Figure 4.10. The lossy characteristics of the glycerine make the design slightly particular. A tapered balun normally has a length of several wavelenghts, however, in this case it is quite short in order to maintain a compact structure and reduce the losses. On the other hand, this lossy environment provides a wideband response from the dipole antenna (Fox *et al.* (2008)). The layout of the antenna, as well as, a photograph of the array arrangement are shown in Figure 4.12(a) and 4.12(b) respectively. The measured and simulated S_{11} parameter of the antenna are shown in Figure 4.13, the measurement is taken with the antenna array placed inside the phantom. The difference between simulations and mesurements can be explained from several factors, among them we can cite the presence of different SMA connectors and cables in the phantom which are not modelled in the CST simulation and possible errors in the measured permittivity values of the glycerine. As it can be seen from Figure 4.13, the antenna presents a wideband behavior due to its immersion in a lossy medium, a $-10dB$ bandwidth almost from 1 to 4 GHz can be observed. Finally, a plot of the E_x field in the plane $x = 0$ is shown in Figure 4.14(a) and 4.14(b) when the phase difference between the two excitation signals in the feeding ports is changed to 0^o and 180^o respectively. When compared with the analytically calculated fields in Figure 4.11, we can see that the array of dipole antennas succesfully launched the desired modes inside the dielectric waveguide.

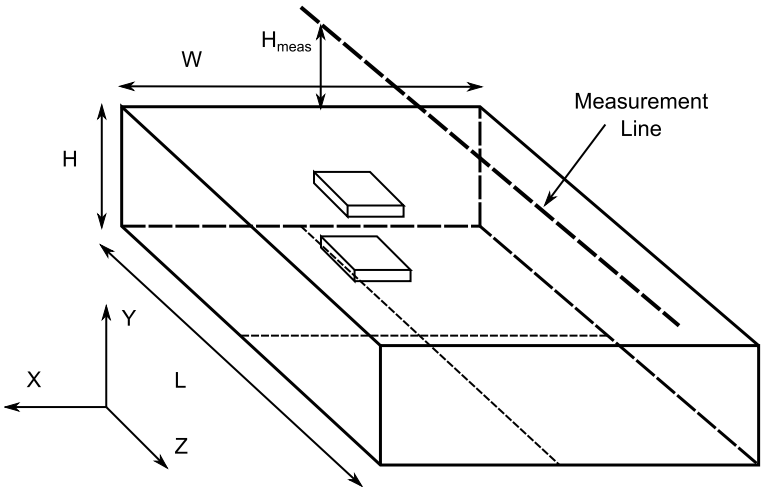

(a)

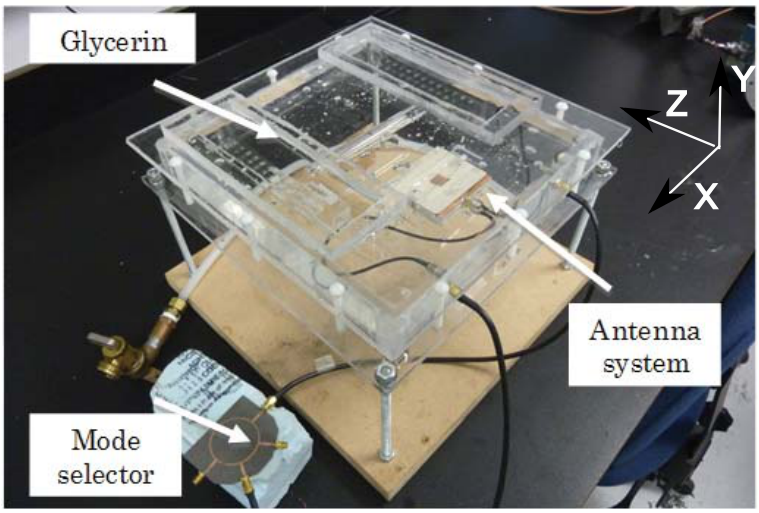

(b)

Figure 4.10 Picture of the implemented dielectric waveguide phantom. The dimensions of the plexyglass container are $W = 250mm$, $L = 270mm$, $H = 38mm$ and $H_{meas} = 5mm$. The plexyglass walls have a thickness of 6 mm. The antenna array is located at $z = -75mm$, where the center of the container is the axes origin.

In order to launch the TM modes, an aperture-coupled patch antenna has been designed. This type of patch antenna is very popular in the litterature and provides several advantages over other methods (Zurcher et Gardiol (1995)). The radiating edges of the patch are parallel to the x axis, so as to generate E_z and E_y components. In our case, a wideband structure was obtained with the utilization of a single patch, again due to the lossy characteristics of the medium in which the antenna is immersed. Again the SWL was created from two identical

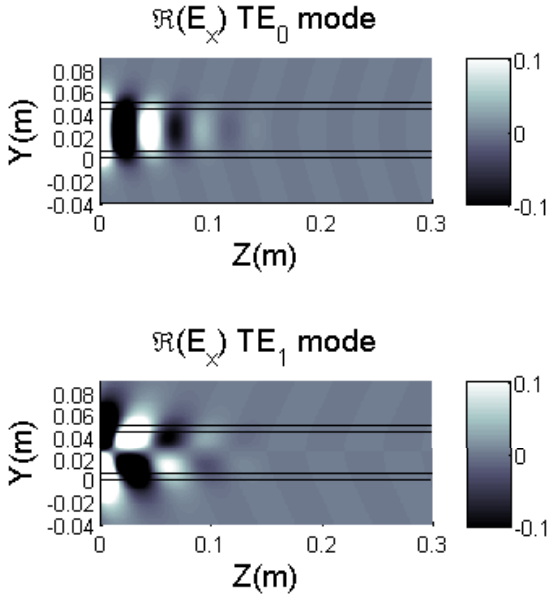

Figure 4.11 Plot of the calculated electric field using the TxM method. TE_0 mode (Top). TE_1 mode (Bottom).

antennas. The two antennas were glued together using silicone adhesive. The permittivity of the cured silicone ($\varepsilon_r = 2.5$) was measured using the HP85070B dielectric measurement probe. The role of this silicone layer was twofold, first to keep the antenna array in place and second to isolate the feeding network from the lossy medium. The layout of the fabricated antennas is shown in Figure 4.15(a) along with a picture of the antenna array in Figure 4.15(b), which is fabricated again on a Rogers 6010 substrates. The measured and simulated S_{11} parameter of the antenna patch elements is shown in Figure 4.16. The differences between measured and simulated data can be explained again from the absence of the cables and connectors in the CST simulation and possible measurement errors in the glycerine permittivity values. Finally, the H_x field in the plane $x = 0$ is plotted in Figure 4.17, where we can see how the two TM modes propagating in the waveguide are correctly excited by modifying the phase shift between the antennas.

In both cases, the fields are only plotted in the x=0 plane, where only the field components of the 2D TE and TM modes are present due to symmetry. In other words, the cross polarization generated by the SWL is negligible. The cross polarization components will increase as we move away from this plane both in the TE and TM cases.

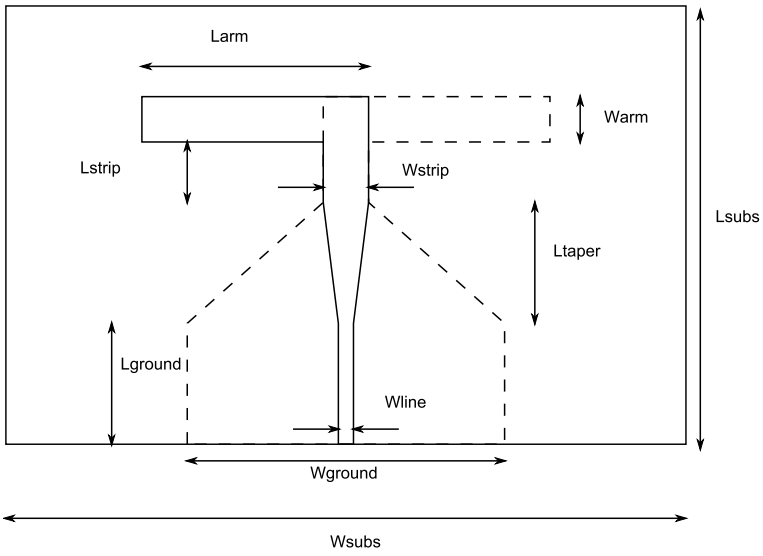

(a)

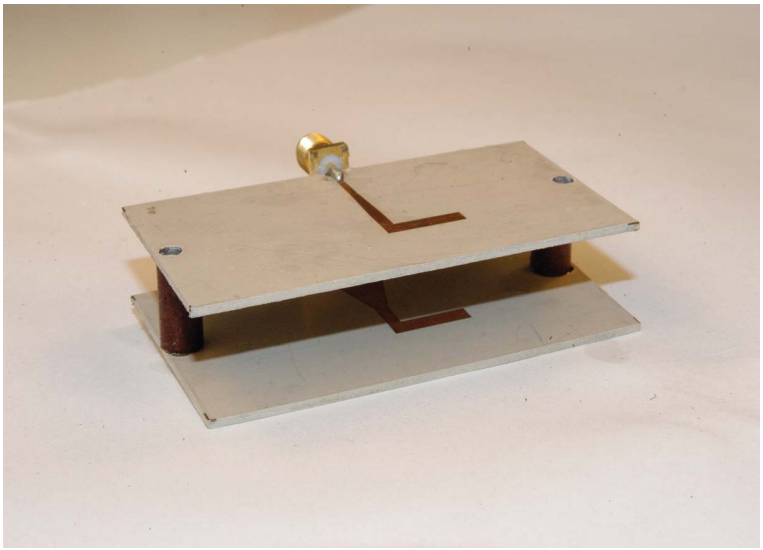

(b)

Figure 4.12 Fabricated dipole antenna. (a) Schema of the fabricated antenna. (b) Photograph of the fabricated antenna. The dimensions of the antenna are : $W_{line} = 1.2mm$, $W_{ground} = 8.4mm$, $L_{ground} = L_{taper} = 10mm$, $W_{strip} = 2mm$, $L_{strip} = 5mm$, $W_{arm} = 3mm$, $L_{arm} = 12.5mm$, $W_{subs} = 68mm$ and $L_{subs} = 40mm$.

4.3.3 Scattered field measurements

The test configuration shown in Figure 4.9 shows the position of the measurement probes above and below of the dielectric plates. The goal now is to examine the perturbation or scattered field produced by a scattering object placed inside the dielectric waveguide. The fields propagating in the waveguide modes follow an exponential decay in the air region and

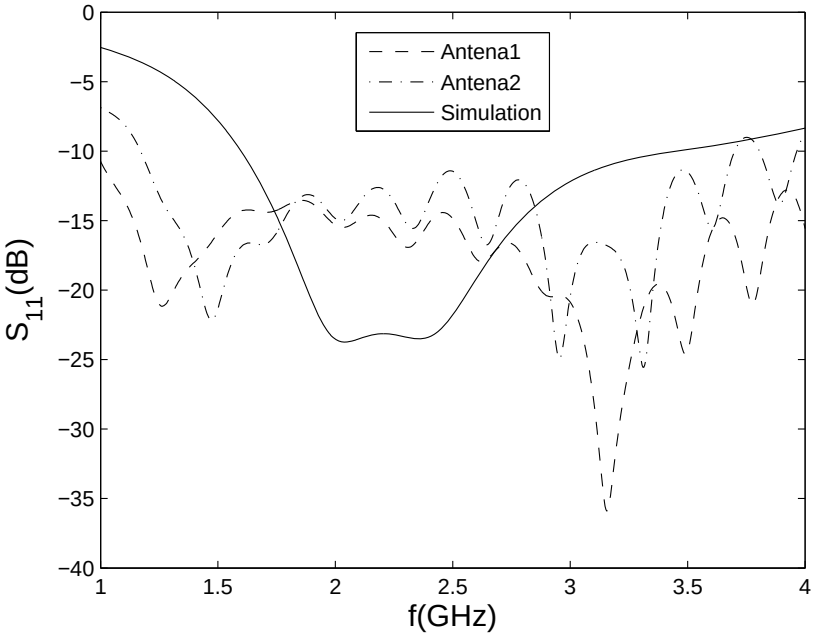

Figure 4.13 Plot of the measured and simulated S_{11} parameter of the dipole antenna array.

thus attenuate very rapidly in the y direction. This phenomena which is of interest for our application, since the field is confined in the region of interest, poses some difficulties for the measurement system. The measurement of propagating surface waves has already been treated in the litterature. Classical scanning near-field probes such as a small loop (Schultz *et al.* (2003)) or a vertical monopole (Freundorfer *et al.* (2006)) have been used. In these cases, a small probe is scanned on top of the waveguide and the fields are proportional to the S_{21} parameter between the transmitting antenna and the output of the probe which is measured using a vector network analyzer (VNA). The probe is normally connected to the VNA using a coaxial cable which can affect the measurement due to the bending of the cable or currents induced in the outer conductor exposed to the measured field. Some of these problems can be reduced using some kind of calibration procedure, for instance, in (Freundorfer *et al.* (2006)) time gating is used to reduce the effects of the cable bending in the measurement of the surface wave pattern.

Another possibility is to use an indirect measurement technique such as the MST already introduced in this chapter. The optically modulated probe, previously introduced in Section 4.2 was set to measure the electric field just above the developed phantom, as shown in Figure 4.10. It consists in a plexyglass container filled with glycerine, where the SWL is fixed at $z = -75mm$ using nylon screws and two small supports made of plexyglass. The OUT is an air-filled tube of radius 8 mm located approximately at $z = -40mm$ and $y =$

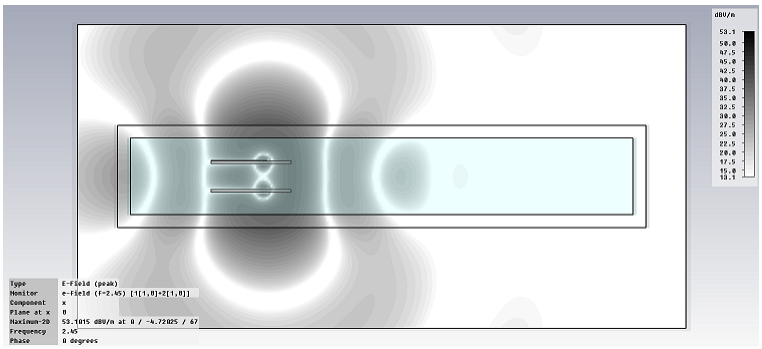

(a)

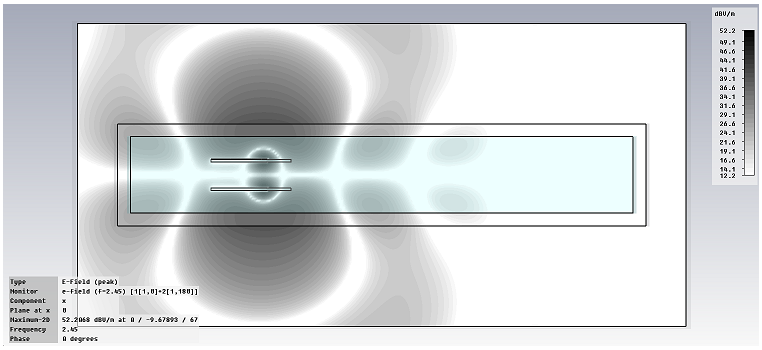

(b)

Figure 4.14 E_x calculated using CST at $x = 0$ plane. (a) TE_0 mode. (b) TE_1 mode.

$11mm$. The scattered field produced by this object was measured along the z direction in the $x = 0$ plane. For each case, the scattered field is obtained as a substracion of two separate sets of measurements with (E_{total}) and without (E_{inc}) the presence of the tube, i.e. $E_{scat} = E_{total} - E_{inc}$. Each component of the electric field can be measured by orienting the dipole of the MST probe in the desired direction. In the TE case, the x component of the electric field was measured, whereas in the TM case E_z was measured. A bi-static MST setup was be used in order to increase the dynamic range in the measurement (Bolomey et Gardiol (2001)). In such a case, the trasmitter is connected to the SWL array and the fields scattered by the MST probe are collected by an auxiliary antenna (collector), which was implemented with an open ended WR284 metallic waveguide. The collector is connected to a homodyne receiver that measures the amplitude and phase of the modulated field (Memarzadeh-Tehran *et al.* (2010)).

The different modes are selected by applying a phase shift between the antennas of the SWL array, which was previously obtained by changing the excitation signal to the port in CST in Section 4.3.2. In practice, the 0^o and 180^o phase shifts are obtained by changing the input in a rat-race coupler. The measured scattered fields both in amplitude and phase for the

different cases are shown in Figure 4.18 to 4.21 for the TE and TM cases respectively, and for the two different modes in both cases. The simulated results performed in CST Microwave Studio are also included in the graphs. As it can be seen from the figures, the presence of the air-filled tubes near $z = -40mm$ can be detected in the scattered field amplitude. Moreover, the measurements agree quite well with the simulations, where the shape of the curves is almost the same without any further calibration process appart from a data normalization, in three of the four cases except for the TE_0 case. This disagreement can be due to many factors, since this is a complicated measurement configuration. One possible explanation, comes from the field distribution created by the SWL. As it can be seen in Figure 4.14(a), the maximum of the field distribution of the mode is located in the middle of the slab and the scatterer is located near the top plate where the field is weaker. This is confirmed by the fact that the measurements for $z > 0$ are buried in noise. On the other hand, some energy from the SWL is radiated and not coupled into the dielectric waveguide, making the incident field to be more intense in the measurement region than in the region where the scatterer is present. These two facts together will make the field scattered from this mode weaker compared to the incident field at the measurement line. Moreover, a big difference is also obtained compared to the other three cases, where we can observe a 10dB difference in the scattered field level compared to the other measured modes. As a matter of fact, a small error in the positioning of the probe will create a large error in the scattered field which is obtained as the difference of two measurements. Such errors have also been reported in a similar measurement setup for the detection of immersed objects in water (Duchêne *et al.* (2004)).

4.4 Conclusion

In this chapter, we have shown the improved design of a light-modulated MST probe. The impact of the tuning network incorporated with the modulated load was investigated by measuring the frequency response of the probe. The bandwidth was increased from 46% to more than 100% compared to the probe proposed in (Memarzadeh-Tehran (2010)). Noninvasiveness of the probe, resulting in more accurate measurements, was improved by fabricating it on a perforated substrate. Performance of the developed probe was assessed by scanning the transverse E-field distribution near a 50- microstrip transmission line at several frequencies. By comparing the measured results to simulations, the accuracy of the probe and the benefit of the tuning network on the frequency response were confirmed.

In the second part of the chapter, we have presented for the first time, the implementation of a dielectric waveguide configuration for the MT problem. Different practical issues associated with this configuration have been addressed. First, it has been shown how different

modes can be launched inside the dielectric waveguide using an array of SWL for both the TE and TM modes. A phantom representing the waveguide configuration consisting in a sealed plexyglass container filled with glycerine has been developed. It has also been shown that a near-field measurement system based on the MST is capable of measuring the scattered field produced by an object inserted in the dielectric waveguide. Moreover, a good agreement between the measured and simulated fields was obtained in three of the cases considered. Finally, it should be pointed out that quantitative reconstructions using the measured data would require an appropriate calibration method of the scattered fields in order to consider the differences between the 2D model and the 3D measured fields as it will be detailed in the next chapter.

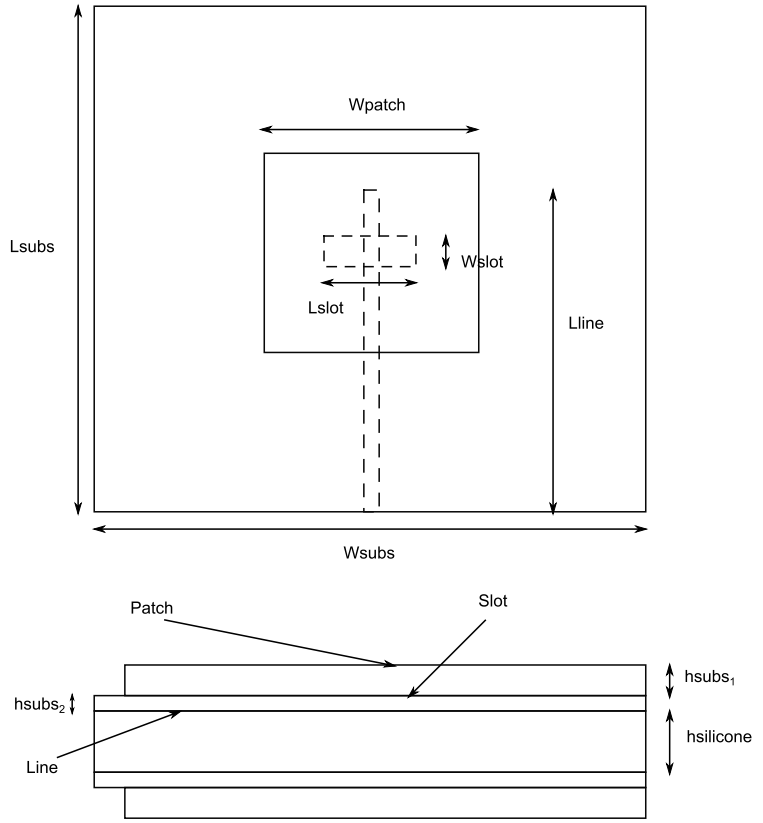

(a)

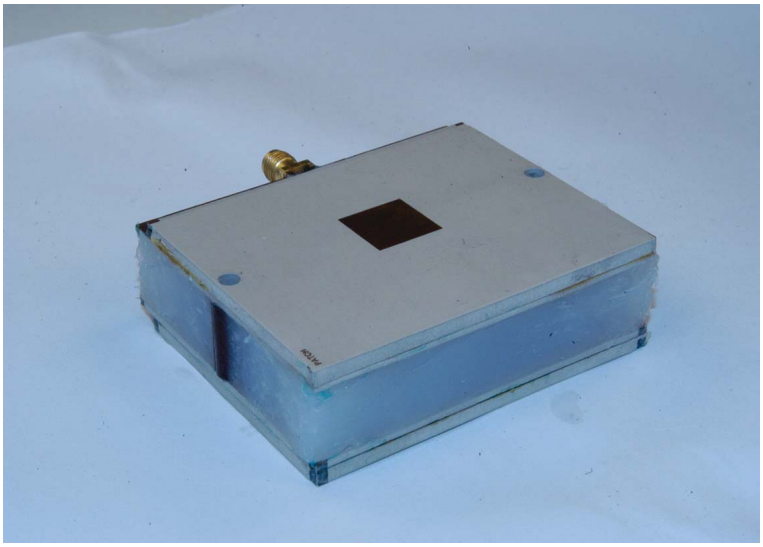

(b)

Figure 4.15 Fabricated patch antenna. (a) Schema of the fabricated antenna. (b) Photograph of the fabricated antenna. The dimensions of the antenna are : $W_{line} = 1.1mm$, $L_{line} = 30mm$, $L_{stub} = 8mm$, $W_{slot} = 2mm$, $L_{slot} = 12mm$, $W_{subs} = 68mm$, $L_{subs} = 60mm$, $h_{subs_1} = 2.54mm$, $h_{subs_2} = 1.27mm$ and $h_{silicone} = 10mm$.

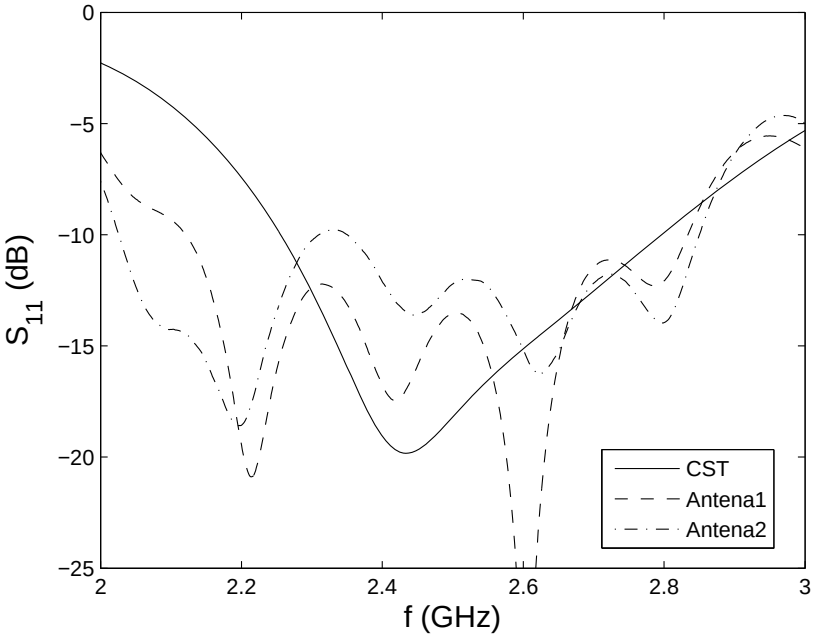

Figure 4.16 Plot of the measured and simulated S_{11} parameter of the patch antenna array.

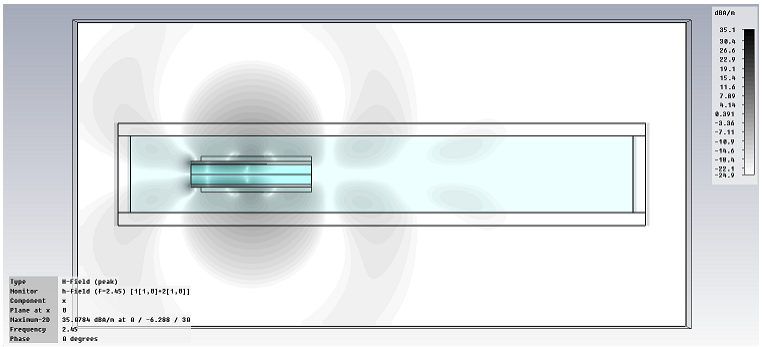

(a)

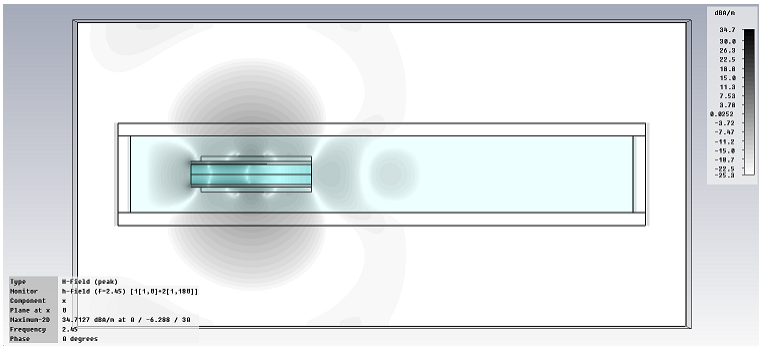

(b)

Figure 4.17 H_x calculated using CST at $x = 0$ plane. (a) TM_0 mode. (b) TM_1 mode.

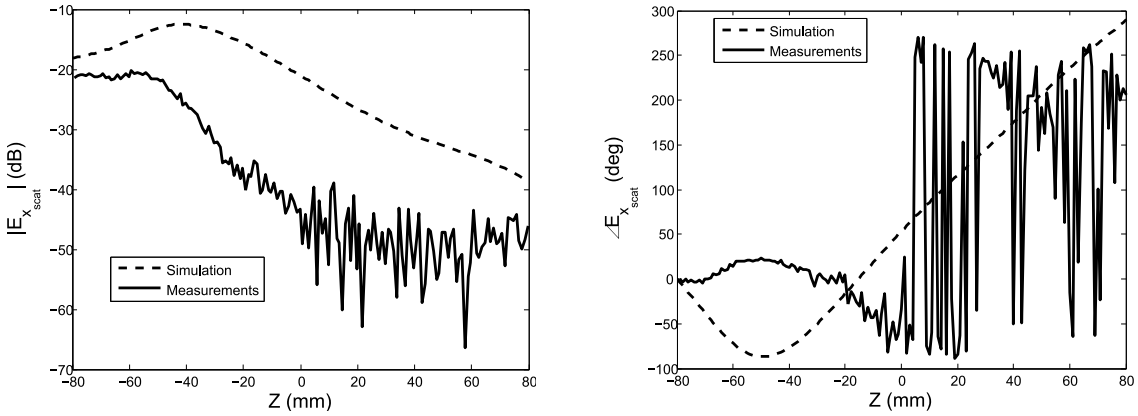

(a) (b)

Figure 4.18 Measured and simulated scattered fields for the TE_0 mode. (a) Magnitude. (b) Phase.

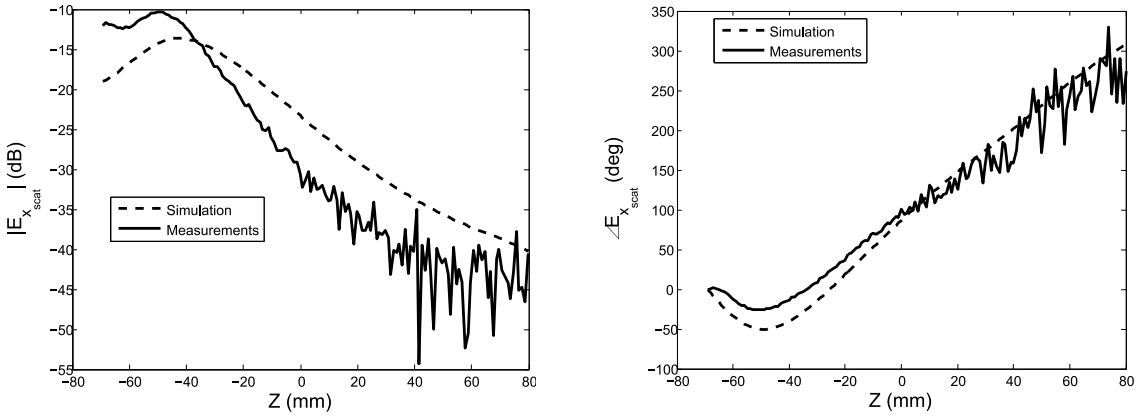

(a) (b)

Figure 4.19 Measured and simulated scattered fields for the TE_1 mode. (a) Magnitude. (b) Phase.

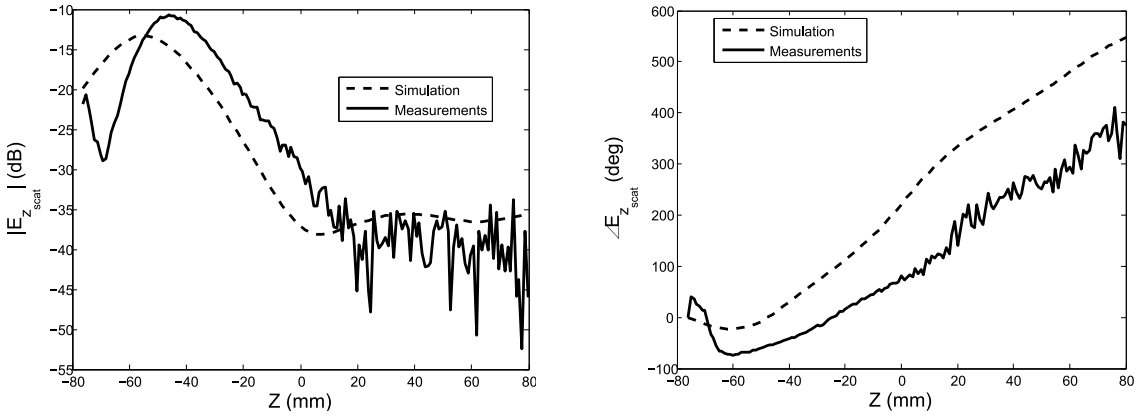

(a) (b)

Figure 4.20 Measured and simulated scattered fields for the TM_0 mode. (a) Magnitude. (b) Phase.

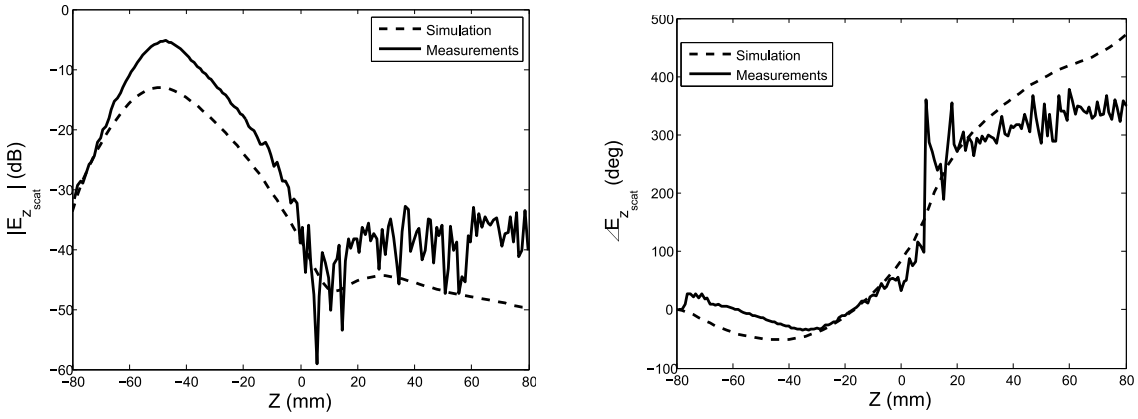

(a) (b)

Figure 4.21 Measured and simulated scattered fields for the TM_1 mode. (a) Magnitude. (b) Phase.

CHAPTER 5

Experimental imaging results on different Microwave Tomography configurations

5.1 Introduction

In this chapter, quantitative imaging results for the different MT configurations proposed in Chapters 3 and 4 will be presented. In all the cases we will assume a 2D TM illumination for quasi-2D objects. This case of MT is commonly found in the literature since it greatly simplifies the reconstruction algorithm for solving the inverse problem. However, this simplification of the inversion problem also has some drawbacks since the reconstructions suppose infinite objects that are treated as 2D problems, while the OUT and the associated measured scattered fields are essentially 3D quantities. From this point it is clear that some calibration of the scattered field is absolutely needed in these cases. Different techniques for data calibration will be discussed in section 5.2. After that we will present quantitative imaging results both for the waveguide and camera configurations in sections 5.3 and 5.4.

5.2 Data calibration

The first step to accomplish a sucessful reconstruction of the spatial electrical properties of an OUT is to obtain a good fitting between the measured scattered fields and the numerical model used in the reconstruction algorithm. The 2D TM numerical model is implemented using the simple discretization presented in Section 2.1.2. On the other hand, the measured fields are 3D and the Green's function expression is different than in the 2D case. Different calibration techniques are available in the literature and will be briefly discussed here.

The first method consists in applying a constant correction factor to the measured scattered field (Franchois *et al.* (1998)). This simple calibration only serves to correct the different source power in the numerical model and in the measurement. The constant can be computed by minimizing the quadratic error between the measured ($\mathbf{y_{meas}}$) and computed ($\mathbf{y_{comp}}$) incident field at the receivers position :

$$K = min_K ||\mathbf{y_{comp}} - K\mathbf{y_{meas}}||^2 \tag{5.1}$$

$$K = \frac{\mathbf{y_{meas}}^{\dagger}\mathbf{y_{comp}}}{||\mathbf{y_{meas}}||^2} \tag{5.2}$$

Where $\mathbf{y_{comp}}$ and $\mathbf{y_{meas}}$ are the computed and measured incident field vector respectively. Symbol † indicate the transpose conjugate since the field vectors and the constant K are complex quantities. The calibrated field is finally obtained as $\mathbf{y_{cal}} = K\mathbf{y_{meas}}$. The same procedure can be done using the scattered field produced by a reference object (Jofre *et al.* (1990)).

In the second method, the calibration coefficient is now a matrix ($N \times M$), where each of N receiver position has an independent correction factor for the M illumination conditions. The technique was first proposed in (Meaney *et al.* (1998a)), and further used in other MT systems (Fhager *et al.* (2006); Henriksson *et al.* (2010); Gilmore *et al.* (2010)). As originally presented, at each point the measured scattered field is multiplied by a complex factor which is the ratio between the measured and computed incident field :

$$\mathbf{E^s_{cal}} = \mathbf{E^s_{meas}} \frac{\mathbf{E^i_{comp}}}{\mathbf{E^i_{meas}}} \tag{5.3}$$

However, more recently it has been shown that better results can be obtained by using the scattered field from a reference object (Litman *et al.* (2010); Mojabi *et al.* (2011)). Also, calibration from one or several reference objects is commonly used in the calibration of polarimetric radars or radar cross section measurement facilities (Whitt *et al.* (1991); Bradley *et al.* (2005)). Typically, a metallic or dielectric cylinder is used as the reference object, since an analytical solution of the scattered field from this object is available (Balanis (1989)). In this case, equation 5.3 is changed to :

$$\mathbf{E^s_{cal}} = \mathbf{E^s_{meas}} \frac{\mathbf{E^{ref}_{comp}}}{\mathbf{E^{ref}_{meas}}} \tag{5.4}$$

Where $\mathbf{E^{ref}_{comp}}$ and $\mathbf{E^{ref}_{meas}}$ are the computed and measured complex scattered field from the reference object.

5.3 Quantitative imaging for the waveguide configuration

5.3.1 Phantom design

The test fixture for the waveguide configuration is now updated for quantitative imaging applications. The new developed structure is shown in Figure 5.1, and a schematic view is also shown in Figure 5.2. Four antennas are placed inside the plexyglass container in order to increase the number of independent illuminations. The phantom is placed vertically, in order to simplify the placement of the scatterers at precise positions. As it can be seen in the figure, the scatterers consist in plastic tubes which are filled with different liquid mixtures.

In the experiment, the phantom is filled with glycerin ($\varepsilon_r = 7.17$ and $\sigma = 0.51 S/m$)

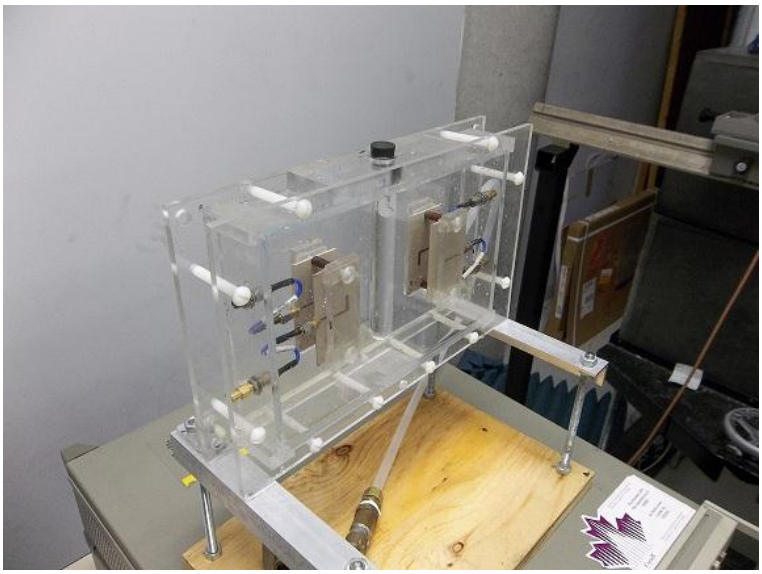

Figure 5.1 Picture of the modified phantom for quantitative imaging using the waveguide configuration.

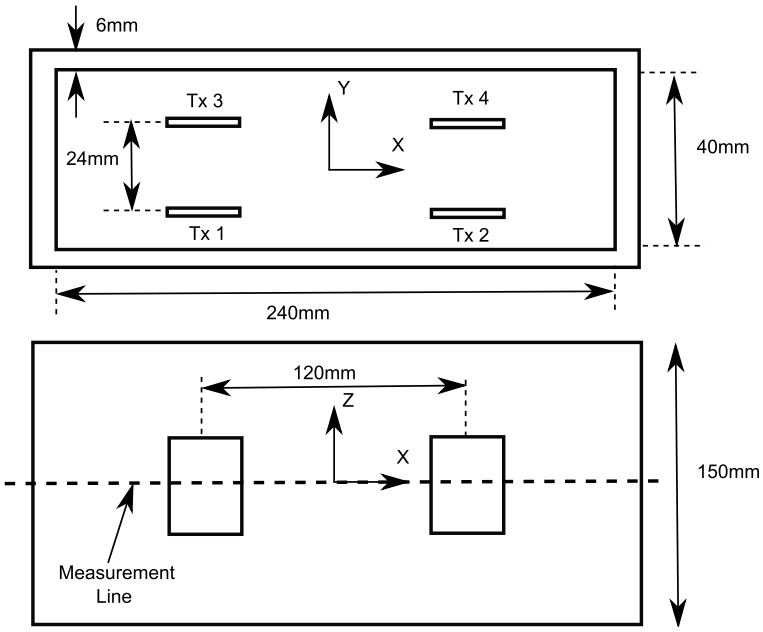

Figure 5.2 Dimensions of the modified phantom.

and liquid mixtures of glycerin and water are used in the tubes for providing different levels of contrast. The permittivity measurements for the different mixtures are shown in Figures 5.3(a) and 5.3(b), and the precise values at the operation frequency of 2.45GHz are shown in Table 5.1.

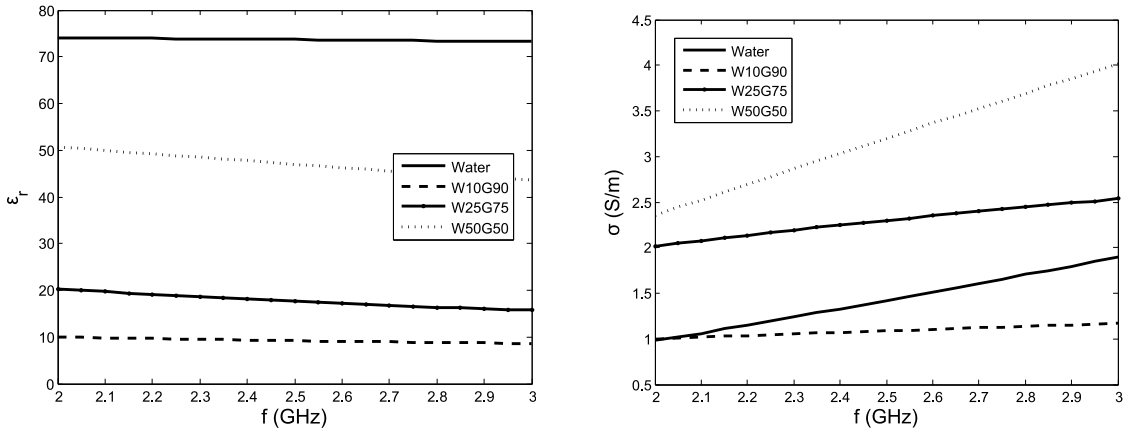

(a) (b)

Figure 5.3 Measured properties of the different liquid mixtures used in the experiment. (a) Relative permittivity. (b) Conductivity. Acronyms WxGy indicate a volume percentage of $x\%$ in water and $y\%$ in glycerin.

Table 5.1 Electrical properties and constrasts of the different liquid mixtures.

Mixture	ε_r	$\sigma(S/m)$	$\Re(\chi)$	$\Im(\chi)$
Water	73.7	1.38	6.78	-3.19
50% Water 50% Glyc	47.32	3.1	4.92	-0.45
25% Water 75% Glyc	17.83	2.27	1.68	0.62
10% Water 90% Glyc	9.24	1.08	0.35	0.25

5.3.2 Modulated scattering technique vs direct near-field measurements

In the previous chapter we presented the development of a NF probe based on the MST principle. This probe was used in the preliminary validation of the waveguide configuration and good agreement between the measured and simulated results was obtained. However, in this section we are interested in quantitative imaging of elongated objects,where the inverse problem is treated as a 2D TM case. In such a situation, the non-invasive property of an optically modulated MST probe may become unnecessary since a calibration procedure is used. The MST based measurement will be compared against a classical near-field measurement probe.

An schematic of the measurement MST setup is shown in Figure 5.4(a) and Figure 5.5(a) shows the optically modulated probe installed to measure the scattered field produced by a tube placed in the middle of the phantom. As it can be seen from the figure, one of

the dipole antennas is excited and the field is scattered by the probe and collected by an open-ended waveguide (WR284) in a bistatic configuration. The probe and the collector are scanned together along the measurement line, previously defined in Figure 5.2. The effect of moving together both the probe and the collector reduces the impact on this latter in the measurement (Bolomey et Gardiol (2001)). The modulated field is then measured using an homodyne receiver, which downconverts the modulated signal and separates it into its in-phase (I) and quadrature (Q) components at the modulation frequency. The two components are then measured alternatively using a Lock-in-Amplifier (LIA).

On the other hand, Figure 5.5(b) shows the probe used in the direct near-field measurement approach. In this case, the probe is a small dipole excited through a marchand balun and connected to the measurement system using a coaxial cable (Elasoued (2004)). The measurement configuration is shown in Figure 5.4(b), in this case the measurement is performed using a VNA (HP 8753D) and collecting the transmission parameter (S_{21}) between the transmitting antenna and the probe.

The scattered field is in general a low pass function (Bucci et Franceschetti (1989)), and its Fourier transform can be exploited to estimate the SNR in the measurement (Litman *et al.* (2010)). In order to compare the direct and indirect measurement techniques, the average spectrum amplitude is computed for the two different systems for the scattered field produced by a cylinder filled with a mix of 25% water and 75% glycerin as shown in Figure 5.6. The Fourier Transform of the scattered field for each one of the four illuminations is computed and the amplitude spectrum average of all the illuminations is plotted in the figure. The SNR can be estimated as the "sidelobe" ratio, since the high-frequency components must be due to the noise. As it can be seen from the figure, the SNR is approximately 5 dB higher in the case of the direct measurement (28 vs 33 dB). This enhancement in the SNR is due to several factors. First, in the measurement principle of the MST the signal is re-radiated from the probe to the collector and some additional losses are introduced in this process. Secondly to the design of the receiver equipment in the case of the indirect technique, where the overall noise figure of the circuit could be enhanced. In the case of the MST technique, the receiver is a custom-made homodyne receiver connected to a LIA and in the direct measurement a commercial VNA is used. Moreover, in order to increase the SNR in the measurement, the time constant of the low pass filter inside the LIA has to be set to a high value to increase the averaging in the instrument. This fact makes the measurement using the LIA considerably time consuming compared to a VNA based system, where the averaging is performed much faster. For these reasons, the direct near-field measurement system will be used in the remaining measurements of this chapter.

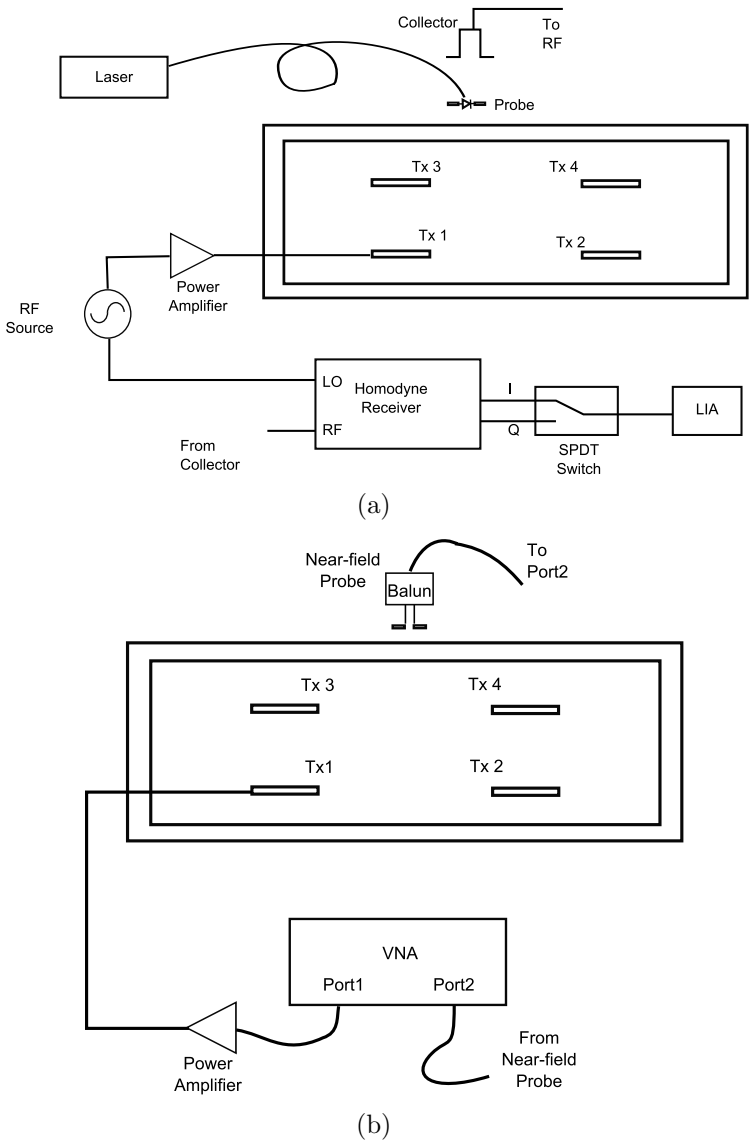

Figure 5.4 Schematic view of the different measurement procedures. (a) Bistatic MST measurement setup. (b) Direct near-field measurement setup using VNA.

5.3.3 Reconstruction results

In this section, we will try to obtain quantitative images of a scatterer placed inside the waveguide from measurements of its scattered field. The scatterer is a cylinder of radius 8mm filled with different mixtures of water and glycerin, at two different positions, $(x = 0, y = 0)$ and $(x = 0, y = 10mm)$ with respect to the axis defined in Figure 5.2. The scattered field is obtained from the substraction of two separate measurements, one without the object and another one with the object present. The measurement was repeated for each of the transmitters and the different liquid concentrations. Finally the measured scattered field is

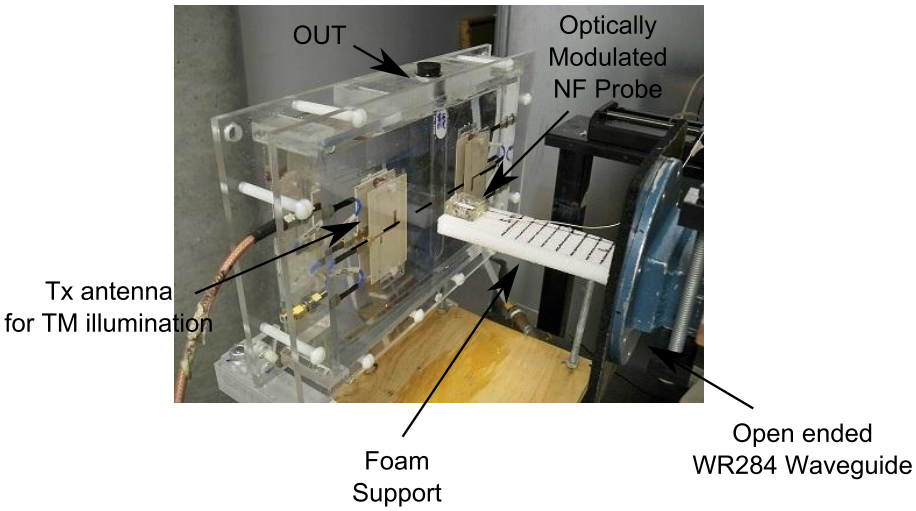

(a)

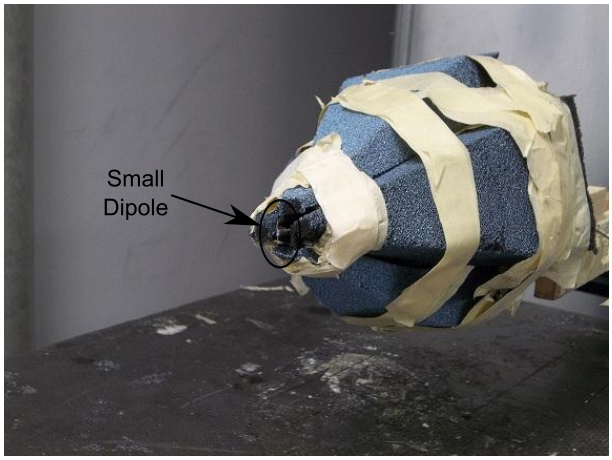

(b)

Figure 5.5 Photograph of the different measurement procedures. (a) MST probe and open waveguide collector placed near the phantom. (b) Near-field measurement probe with absorber to minimize the effect of the balun and coaxial cable on the measurement.

calibrated using equation 5.4, where the reference object is the cylinder filled with a mixture of 50% water and 50% glycerine. The scattered field distributions, both in magnitude and phase, are plotted in Figure 5.7 for the calibrated measurements and the obtained results from the MoM numerical model. Four different cases are plotted in the figure, two different liquid concentrations (50% water/25% glycerine and 10% water/90% glycerine) and the two positions of the cylinder previously defined. The field is measured by scanning the probe to a total of 81 positions from $x = -40mm$ to $x = 40mm$ with a stepsize of 1mm. The results are plotted sequentially for each one of the four transmitters, this is, the results for the first transmitter correspond to the 81 first points in the graph, the second 81 points correspond

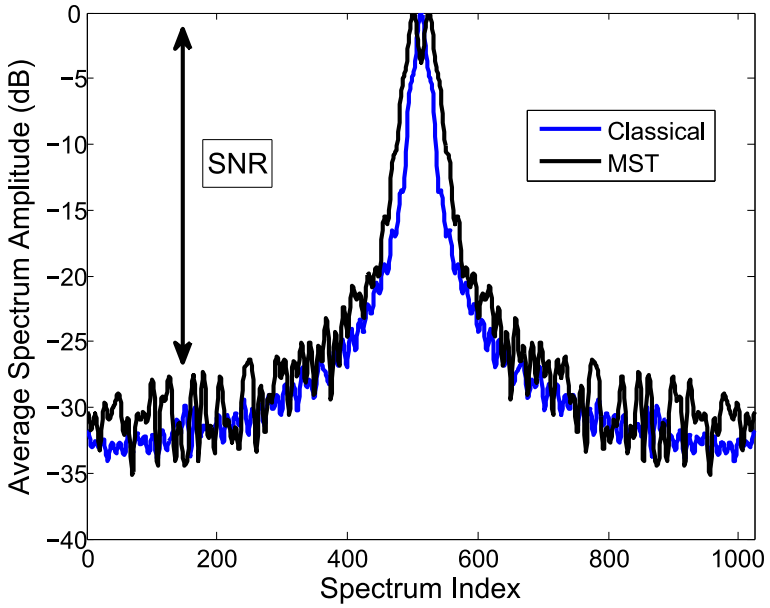

Figure 5.6 Comparison of the SNR of the two measurement systems from the average amplitude spectrum (FFT with 1024 samples).

to the second transmitter and so on.

Several facts can be extracted from Figure 5.7. First of all, in the case of 10% water/90% glycerine the contrast is very small and the level of scattered field is not high enough to allow a correct measurement. Second, we can see in Figures 5.7(a) and 5.7(b) that there is a very good agreement between the numerical model and the calibrated results for the first two transmitters, however, this is not the case for the third and fourth transmitters. The explanation for this phenomena can be understood looking at a plot of the incident field obtained using CST Microwave Studio from the two different type of transmitters in Figure 5.8. Figure 5.8(a) represents the incident field created by the second transmitter antenna at the plane $z = 0$, whereas Figure 5.8(b), represents the field for the fourth transmitter. In the case of the fourth transmitter, the incident field is higher in the measurement positions (identified by a dashed line) than in the reconstruction region (identified by the black contour of a square), this fact will produce a very weak scattering from the object where at the same time the incident field is very high at the receiver positions. Since the scattered field is measured as the difference between two measurements, with and without the scatterer, a small error in any of these measurements will produce a huge error in the measured scattered field (Duchêne *et al.* (2004)). This effect can be very well appreciated in Figure 5.7(a), where the scattered field is much weaker from the last two illuminations and a large difference is observed between the measured results and the numerical model.

The reconstructed images obtained from the calibrated measurements are shown in Fi-

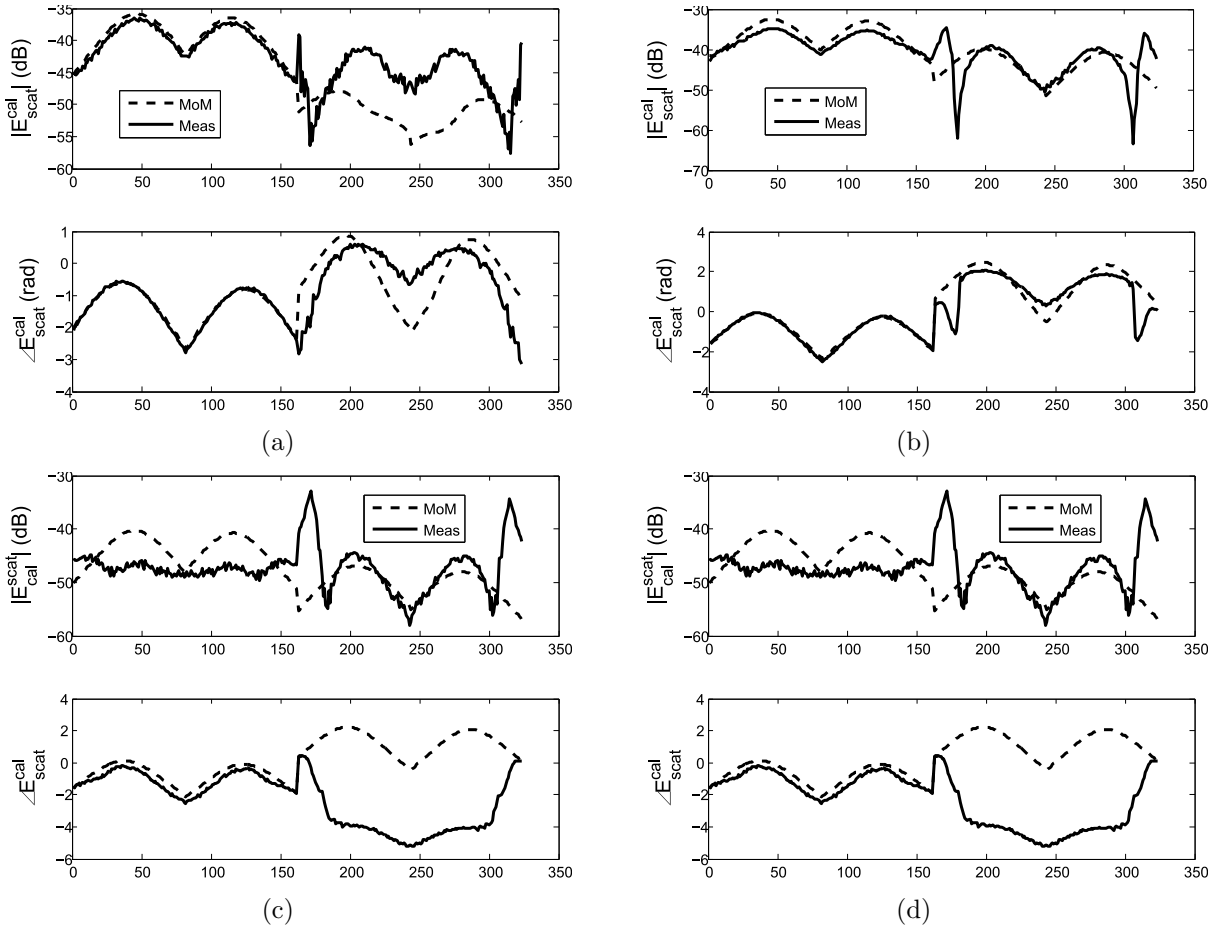

Figure 5.7 Plots of the scattered field for the different cases for both the calibrated measurements and numerical model solutions . (a) 25%Water/75%Glycerine scatterer located at $x = 0$, $y = 0$. (b) 25%Water/75%Glycerine scatterer located at $x = 0$, $y = 10mm$. (c) 10%Water/90%Glycerine scatterer located at $x = 0$, $y = 0$. (d) 10%Water/90%Glycerine scatterer located at $x = 0$, $y = 10mm$

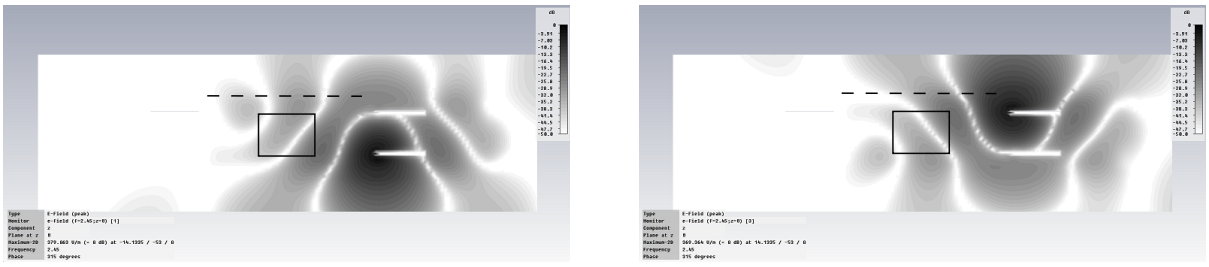

Figure 5.8 Simulation of the incident field using CST Microwave Studio. (a) Transmitter 2. (b) Transmitter 4.

gures 5.9 to 5.12. In all the cases, the first row presents the permittivity and conductivity of the original object, the second row represents the reconstructed results obtained from synthetically generated data (numerical model with added gaussian noise) and the third row represents the reconstructed results from the calibrated measured data. In Figures 5.9 and 5.10, the measured reconstructed results are obtained using only the measured fields from the two first transmitters, where a good agreement between the calibrated measurements and the numerical model was obtained. On the other hand, in Figures 5.11 and 5.12, the measured reconstructed results are obtained mixing the calibrated data for the first two transmitters with synthetic data for the other two transmitters. Also the MSE of the different reconstructions is shown in Table 5.2.

In all the cases, the reconstructions performed using synthetically generated data are included to show the limit of the proposed configuration. As it can be seen from the figures, in all the cases the object can at least be inferred from the images, however, with only two illuminations there is not enough information for a good reconstruction of the object. When the number of illuminations is increased, the quantitative reconstructions for the two positions of the object are significantly enhanced.

Table 5.2 MSE of the different reconstructions.

Case	Measured data	Synthetic data
$x = 0$ $y = 0$ 2Tx	0.6543	0.5366
$x = 0$ $y = 10$ 2Tx	0.6726	0.4097
$x = 0$ $y = 0$ 4Tx	0.3138	0.1831
$x = 0$ $y = 10$ 4Tx	0.3988	0.1733

5.4 Quantitative imaging for the camera configuration

In this section the effect of breast compression in Microwave Tomography (MT) for breast cancer detection is analyzed experimentally on a simplified phantom. For this purpose, the same inhomogeneous scatterer has been reconstructed using two phantoms representing two different levels of compression in a camera configuration. The developed phantom, based on some mechanical properties of breast tissues is presented, as well as, the measurement procedure. The imaging capabilities of the camera configuration are briefly analyzed in order to quantify the effect of number of transmitters and receivers on the quality of the reconstructed images. Finally, the quality of the measurements and the reconstructed images from the two phantoms are compared in terms of the Signal to Noise Ratio (SNR) and the Mean

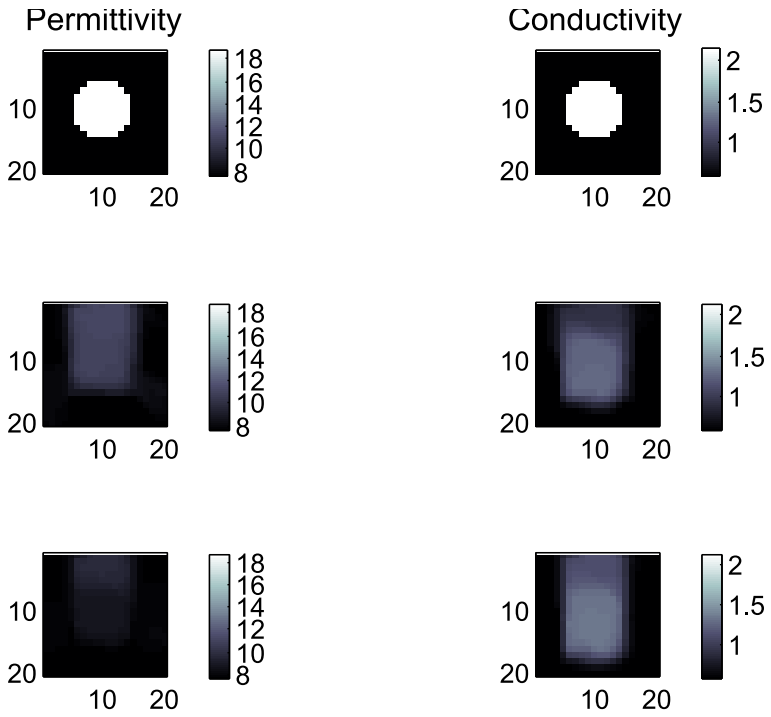

Figure 5.9 Reconstructed images for the scatterer placed at $x = 0$ and $y = 0$ from the measurements of only two transmitters. Top : Original image. Middle : Reconstructions using synthetic data. Bottom : Reconstructions using measured data.

Square Error (MSE) respectively. The content of most of this section is adapted from a paper submitted to IEEE Antennas and Wireless Propagation Letters.

5.4.1 Introduction

The main objective of this paper is to prove experimentally the conclusions presented in Chapter 3, where it was shown that using breast compression, the Rx antennas can be placed closer to the OUT and the quality of the reconstructed images, and consequently the probability of detecting tumors, can be greatly improved. The phantom has been developed from the simplified mechanical assumption that the glandular tissue is stiffer than the fatty tissue (Kellner *et al.* (2007)) and thus the compression will produce a deformation of the latter while the former remains more or less unchanged. On the other hand, other studies suggest that both types of tissue present a similar value of the Young Modulus (Samani *et al.* (2003)). These studies have been performed in the framework of the small deformations used in elastography. This is not the case in the levels of compression used in mammography and therefore a mechanical modelling able to handle large deformations and the expected non-linearity in the mechanical behavior should be used in future studies.

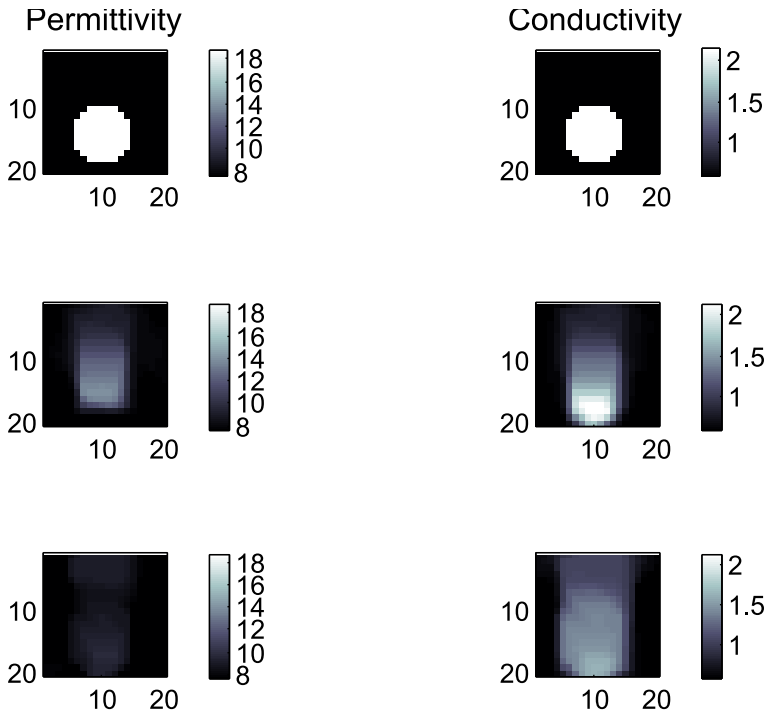

Figure 5.10 Reconstructed images for the scatterer placed at $x = 0$ and $y = 10$ from the measurements of only two transmitters. Top : Original image. Middle : Reconstructions using synthetic data. Bottom : Reconstructions using measured data.

The developed phantom is shown in Fig. 5.13(a). It consists of two different plexyglass containers of the same height and width, but with different thicknesses in order to represent two different levels of compression. The dimensions of the phantoms are given in the caption of Fig. 5.13. The height of the phantom is assumed long enough compared to the phantom-to-antenna distances to allow a 2D reconstruction. The inhomogeneous scatterer that will be reconstructed, is a combination of two plexyglass cylinders. The phantom is filled with glycerin ($\epsilon_r = 7.17$ and $\sigma = 0.51 S/m$), whereas the plexyglass cylinders are filled with different mixtures of glycerin and water. For the measurements on the two phantoms, the scatterers will remain at the same $y = 0$ position, while the reconstruction region will be changed in order to maintain the same area and make a fair comparison between the two levels of compression.

A schematic view of the measurement setup is shown in Fig. 5.13(b). A quasi-yagi antenna, mounted on a translation stage, is used to illuminate the phantom. The translation stage allows to create the desired number of independent illuminations. The scattered fields transmitted through the phantom are measured in two different measurements, with and without the OUT, using a small dipole near-field probe. The measurement probe is scanned through the x axis, using a second translation stage. Finally, the vector network analyzer mea-

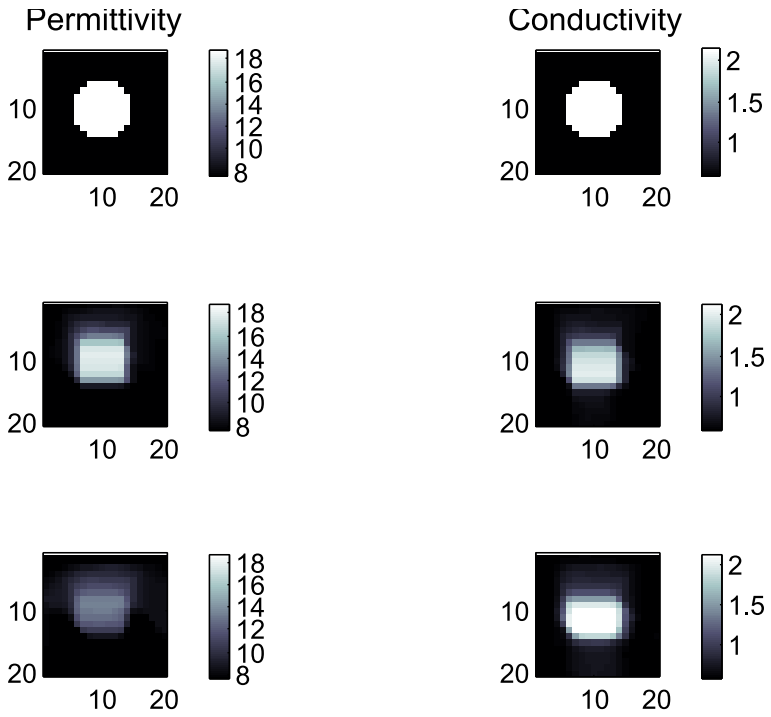

Figure 5.11 Reconstructed images for the scatterer placed at $x = 0$ and $y = 0$ from the measurements of two transmitters plus the other two measurements obtained from synthetic data. Top : Original image. Middle : Reconstructions using only synthetic data. Bottom : Reconstructions using measured and synthetic data.

suring the transmission from the antenna to the near-field probe, as well as the translation stages, are controlled from a PC using Labview.

5.4.2 Properties of the imaging configuration

In this section, the different parameters that come into play in this camera configuration will be analyzed. An schematic view of a 2D cut of one of the phantoms used in this study is shown in Figure 5.14, where the different variables analyzed are shown. The phantom is the smallest one of the two described in the previous section ($W = W_2$) using the two cylinders as OUT filled with a mixture of glycerine and water (25% Water and 75% Glycerine, $\epsilon_r = 17.83$ and $\sigma = 2.269 S/m$). A series of reconstructions using synthetically generated measurements are performed on the phantom and the obtained images are compared in terms of the MSE. Where MSE is defined as $\Delta x = \|x - x_0\|^2 / \|x_0\|^2$, in which x_0 and x are the original and reconstructed spatial distributions of the contrast respectively.

The two parameters analyzed in the study are the number of Tx that generate the required independent illuminations (N_{tx}) and the distance between the Rx and the OUT ($D_{Ph-to-Rx}$), while the other parameters shown in Figure 5.14 are kept fixed during the study. $D_{Ph-to-Tx}$

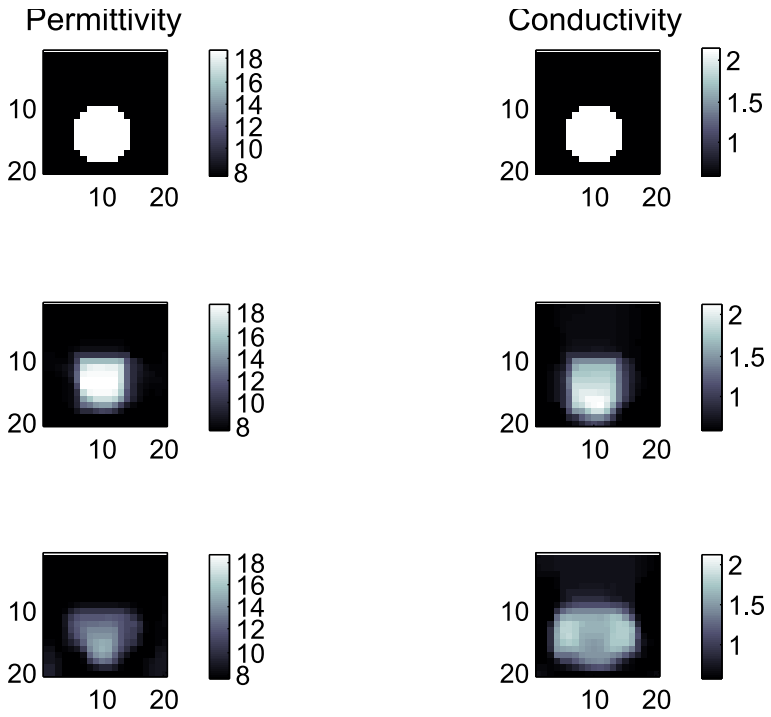

Figure 5.12 Reconstructed images for the scatterer placed at $x = 0$ and $y = 10$ from the measurements of two transmitters plus the other two measurements obtained from synthetic data. Top : Original image. Middle : Reconstructions using only synthetic data. Bottom : Reconstructions using measured and synthetic data.

and d_{tx} are set to 10mm and a total of 120 measurement points, with a stepsize (d_{rx}) of 1mm between them is used in the reconstructions. The imaging region D consists of 60 by 20 pixels with a discretization step of 2mm. Only the region inside the plexyglass enclosure is considered in the reconstruction. The information about the inhomogeneous background composed of the air region, plexyglass plates and glycerin is included in the Green's function and incident field used in the CSI algorithm, where these quantities are computed numerically, as previously explained in Section 3.4.

The MSE of the reconstructions from synthetically generated data for different values of N_{tx} and $D_{Ph-to-Rx}$ are plotted in Figure 5.15, while the images resulting from the reconstructions are included in Figure 5.16 and 5.17 for illustrating the enhancement in the quality of the images. The results show the enhancement of the reconstructed image quality as the N_{tx} is increased, however there is a limit under which the MSE does not decrease significantly. A clearly visible enhancement of the quality of the reconstructed image was obtained when N_{tx} augmented from 3 to 11 , but this enhancement was less pronounced between 11 to 21. Further increments in the value of N_{tx} reduced the MSE, however almost no enhancement could be visually appreciated. For this reason, the value of N_{tx} for the experimental measurements

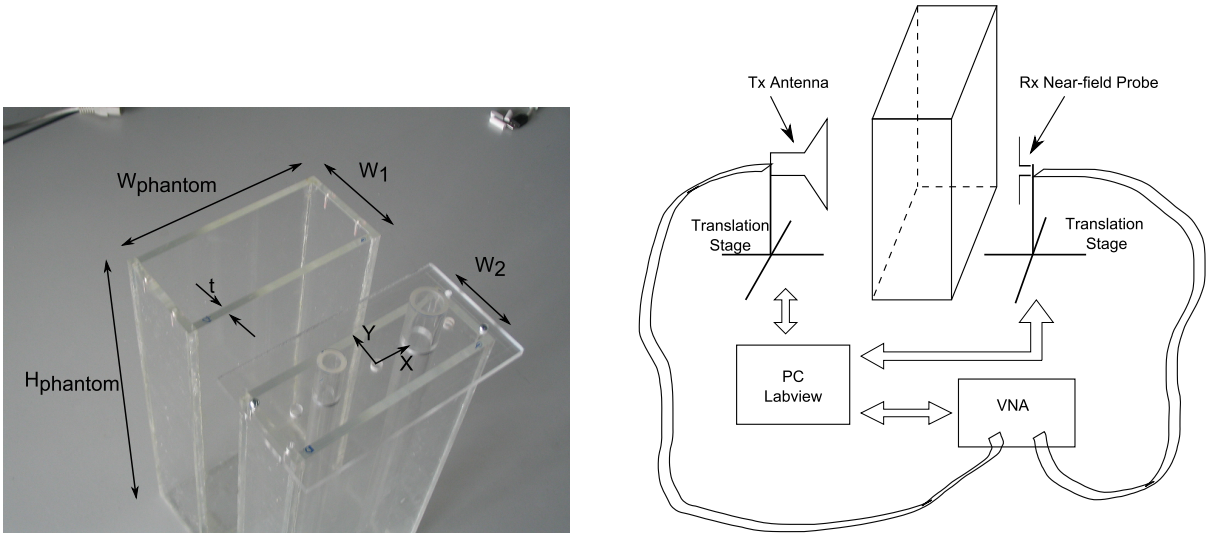

(a) (b)

Figure 5.13 (a) Photograph of the 2 different phantoms. (b) Schematic diagram of the measurement setup. $W_{phantom} = 150mm$, $H_{phantom} = 300mm$, $W_1 = 60mm$, $W_2 = 40mm$, $t = 6mm$. The cylinders have a diameter of 25mm and 15mm respectively and are located at $x = -17.5$, $y = 0$ and $x = 17.5$, $y = 0$.

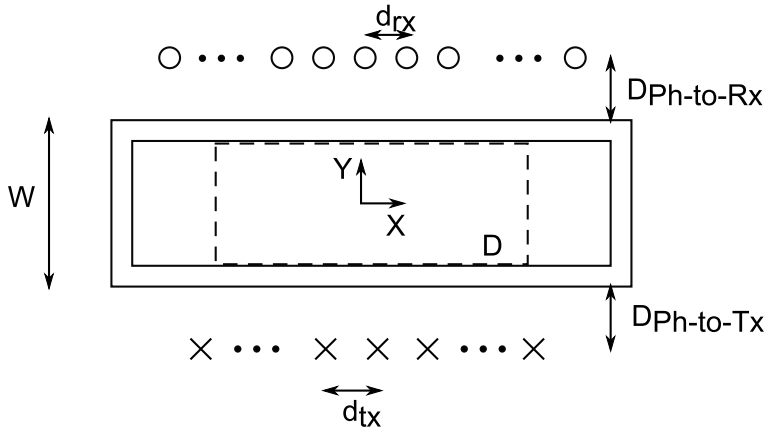

Figure 5.14 Schematic of the different parameters analyzed in the study. $D_{Ph-to-Tx} = d_{tx} = 10mm$, $N_{rx} = 121$, $d_{rx} = 1mm$. The positions of the Txs are symmetrically located with respect to the plane $x = 0$.

will be fixed to 11, since this number represents a trade-off between the quality of the images obtained and the complexity of the setup. Finally, four different values of $D_{Ph-to-Rx}$, namely 20, 10, 5 and 1mm are studied. As it can be seen from the figure, the reconstructions are greatly enhanced when the measurement probes are closer. This was also observed in earlier work on a cylindrical geometry (Fang *et al.* (2006)), and on a similar geometry to the one

considered here in (Barriere (2008)).

5.4.3 Experimental quantitative results

In this section, the results of a series of measurements conducted in the previously introduced phantoms are presented. First of all, the quality of the measurements for the two different phantoms are compared in terms of the SNR. Finally, the reconstructed images obtained from the measured scattered fields are presented and compared for the two different levels of compression.

The immersion medium used in MT is generally lossy (Grzegorczyk *et al.* (2012)), hence, different levels of compression will produce different levels of attenuation and affect the SNR in the camera configuration. An estimate of the SNR in the measurement can be obtained from an average over all the illumination cases of the Fourier transform of the measured scattered fields, since this average amplitude spectrum must be a low-pass function and the high-frequency components are only due to noise (Litman *et al.* (2010)). The Fourier transform of the raw measured scattered fields along the x direction is plotted in Fig. 5.18 for the two different phantoms. A difference of 5dB in the SNR can be observed between the two cases (45dB versus 40dB), showing the effect of the increased losses in the measurements.

Reconstructions of the phantoms are then performed using the previously mentioned 2D CSI algorithm. However, the measurements are performed on finite 3D objects and calibration is needed in order to correct the measured scattered fields to account for the different propagation factors of the 2D and 3D cases. The calibration matrix is obtained based on a reference scattering object (Litman *et al.* (2010); Meaney *et al.* (1998b)), the reference objects are the same cylinders used as OUT filled with a different concentration of glycerine and water. Another important aspect to obtain an accurate reconstruction of the electrical properties of the OUT is to obtain a good modelling of the incident field in the reconstruction region, in our case, the transmitting antenna is modelled as an infinite current source. In this measurement configuration, the inhomogeneous phantom is in the very near-field of the antenna. Therefore, different OUTs may change the radiation behavior of the antenna due to a loading effect. In such conditions, it is not possible to define *a priori* where to place the current source representing the Tx antenna during the inversion process. The position of the current source with respect to the wall of the phantom was determined as the one which minimized the error between the calibrated measured data and the scattered field generated using the MoM code. The agreement between the calibrated measurements and the MoM data, both in magnitude and phase, is shown in Fig. 5.19, where the information for the different Tx positions is plotted sequentially for ease of visualization. A better agreement between the measured and computed data is observed in the case of the thinner phantom.

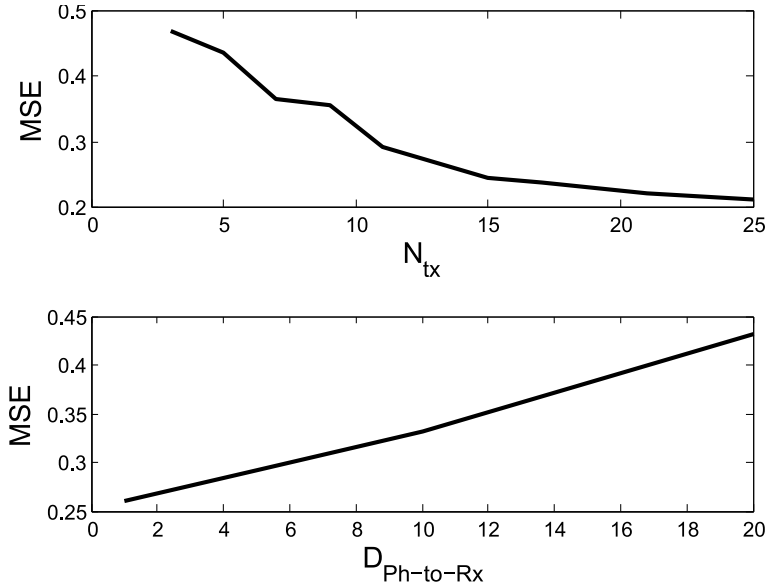

Figure 5.15 Plot of the MSE of the different reconstructions using synthetically generated data with a SNR of 40dB. Top : MSE as a function of the number of Tx in the configuration (N_{tx}) for $D_{Ph-to-Rx} = 10mm$. Bottom : MSE as a function of the distance between the phantom and the receivers in the configuration ($D_{Ph-to-Rx}$) for $N_{tx} = 11$.

Finally the reconstructions of the different OUT are shown in Fig. 5.20 and 5.21 for the 60mm and 40mm thick phantoms respectively. The synthetically generated data for a SNR of 40dB are shown for comparison purposes since they represent the performance of the algorithm in absence of experimental error. Also, the MSE of the four different cases are shown in Table 5.3. As expected, the improvement due to compression is clearly visible in the reconstructed images, qualitatively since the two cylinders can be distinguished in the thinner phantom, and quantitatively since the MSE is greatly reduced in the higher compression case. These measurements were performed with $D_{Ph-to-Rx} = 20mm$. The quality of the reconstructions is possibly affected by the thickness of the plexyglass cylinders.

Table 5.3 MSE of the different reconstructions.

	Measured data	Synthetic data
1 Cylinder 60mm Phantom	0.7071	0.3413
2 Cylinders 60mm Phantom	0.8057	0.4809
1 Cylinder 40mm Phantom	0.4573	0.2204
2 Cylinders 40mm Phantom	0.5703	0.3911

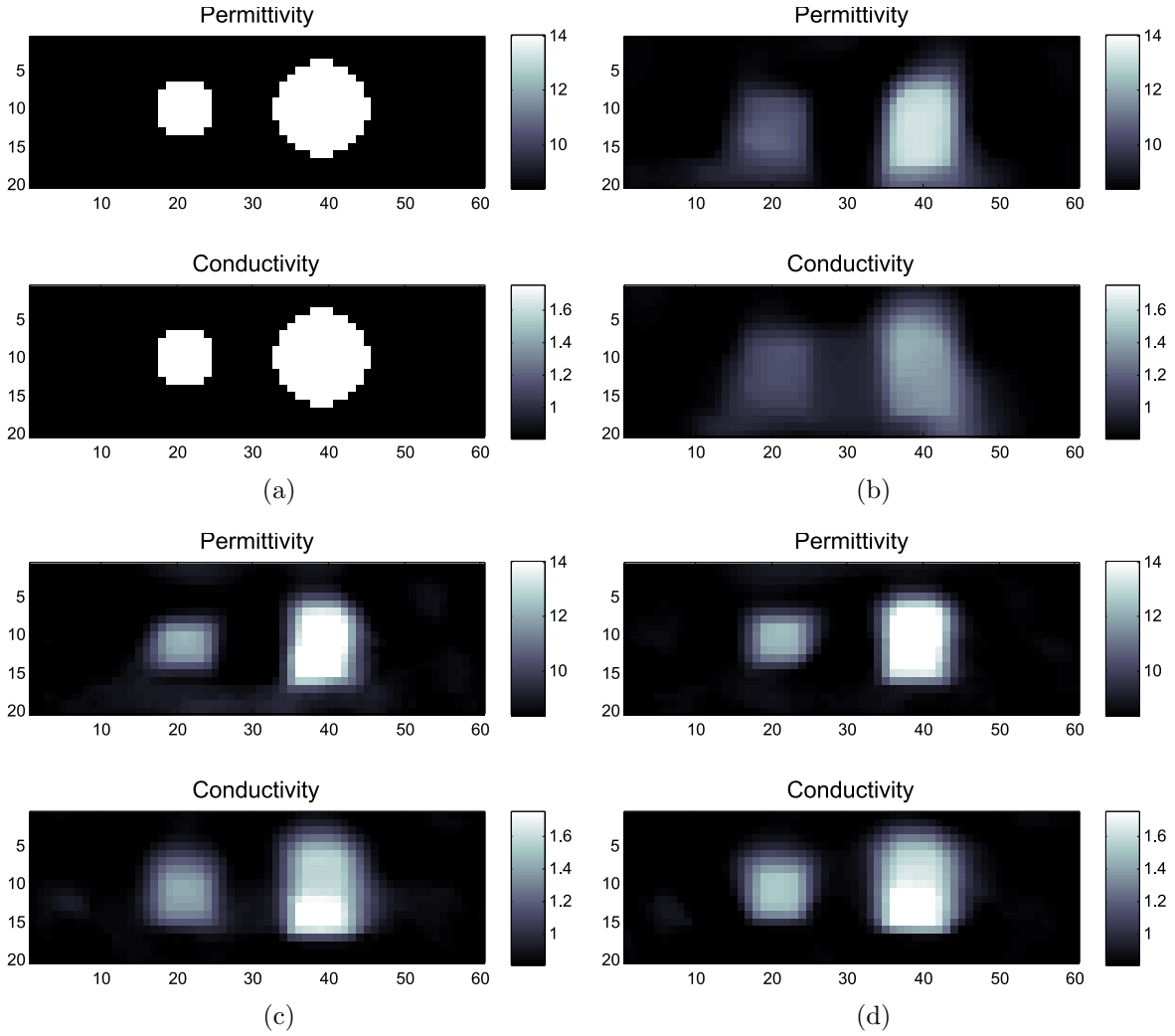

Figure 5.16 Reconstructions for four different values of N_{tx}. (a) Original object. (b) $N_{tx} = 3$. (c) $N_{tx} = 11$. (d) $N_{tx} = 21$.

5.5 Conclusion

In this chapter we have presented some quantitative reconstructions from the previously presented MT configurations for breast cancer detection presented throught this thesis, namely the waveguide and camera configuration. In the case of the waveguide configuration, a comparison between measurements using two different measurement techniques, the MST and the classical direct measurements was performed. It was shown how an enhancement in the SNR in the measurements was obtained by using the classical technique for this particular setup. The reconstructed images obtained from the measurements were not very good for the polarization used, which is consistent with the results presented in chapter 4 were better measured results were obtained using a TM guided mode.

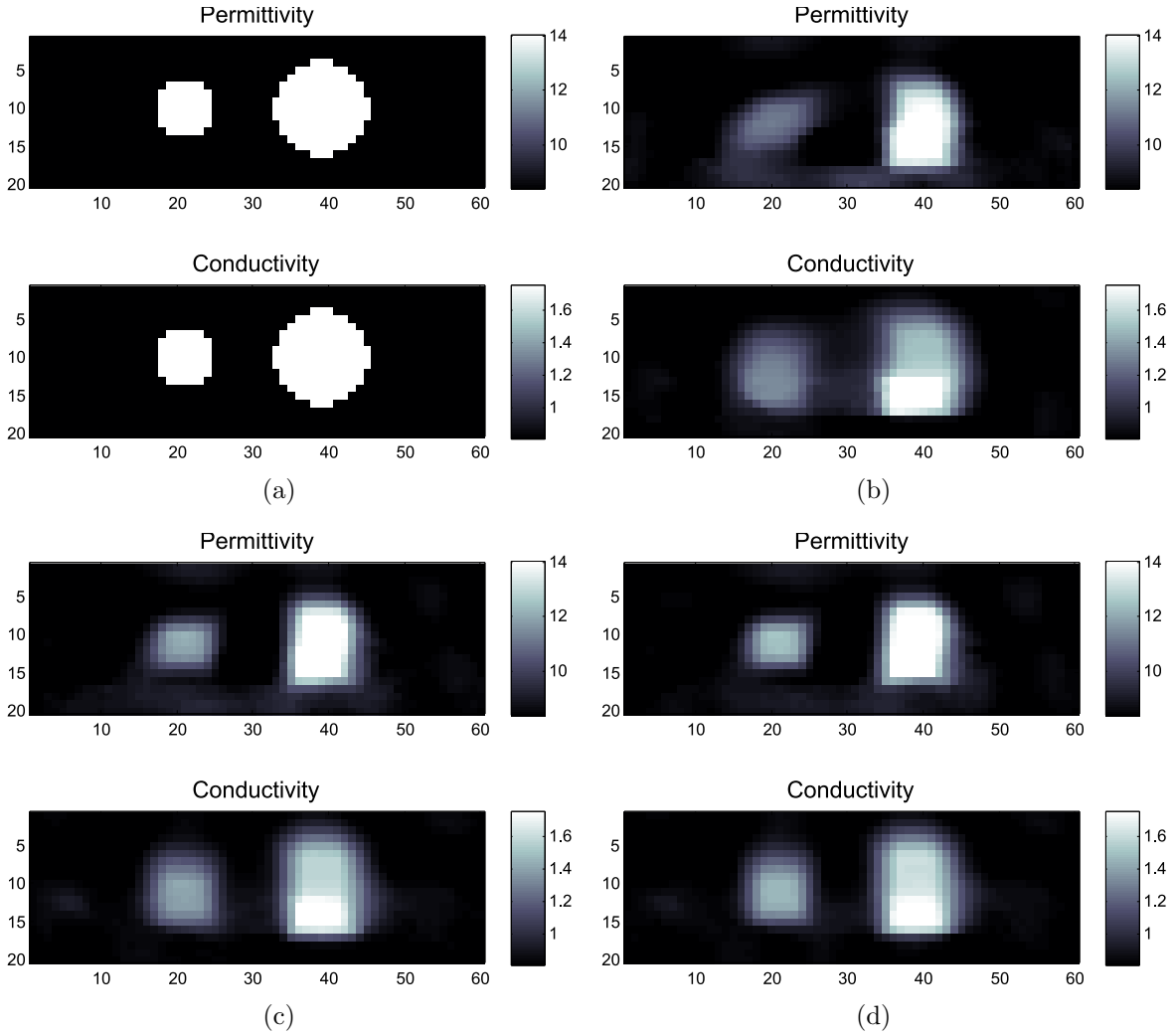

Figure 5.17 Reconstructions for the different positions of the receivers. (a) Original object. (b) $D_{Ph-to-Rx} = 20mm$. (c) $D_{Ph-to-Rx} = 5mm$. (d) $D_{Ph-to-Rx} = 1mm$.

In the case of the camera configuration, we have investigated the effect of breast compression, on very simple phantoms, in MT applied to breast cancer detection using a camera configuration. The developed phantoms, as well as a flexible measurement system based on a near-field measurement probe have been presented. The impact in the reconstructed images quality of the different parameters of the imaging configuration has also been investigated using reconstructions from synthetically generated measurements. As expected, an enhancement in the quality of the reconstructed images from the measured results has been observed in the phantom representing the highest level of compression, since in this case the Rx can be placed closer to the OUT. Finally, it should be pointed out that the camera configuration only measures transmission information, resulting in a limited information for the solution of the inverse problem. It is expected that the quality of the reconstructed results can be

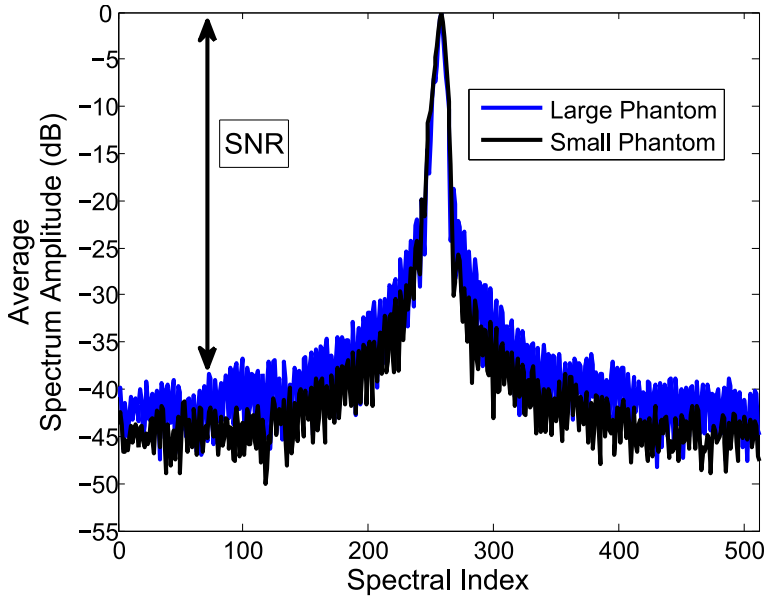

Figure 5.18 Estimation of the SNR of the measurement obtained from the average of a Fourier Transform (FFT with 512 samples) of the raw scattered data for the case of two cylinders filled with 25% Water and 75% Glycerine. Black curve, small compression ($W_1 = 60mm$). Blue curve, high compression ($W_2 = 40mm$).

enhanced by using both reflection and transmission information or by having transmit and receive antennas on both sides of the parallel plates.

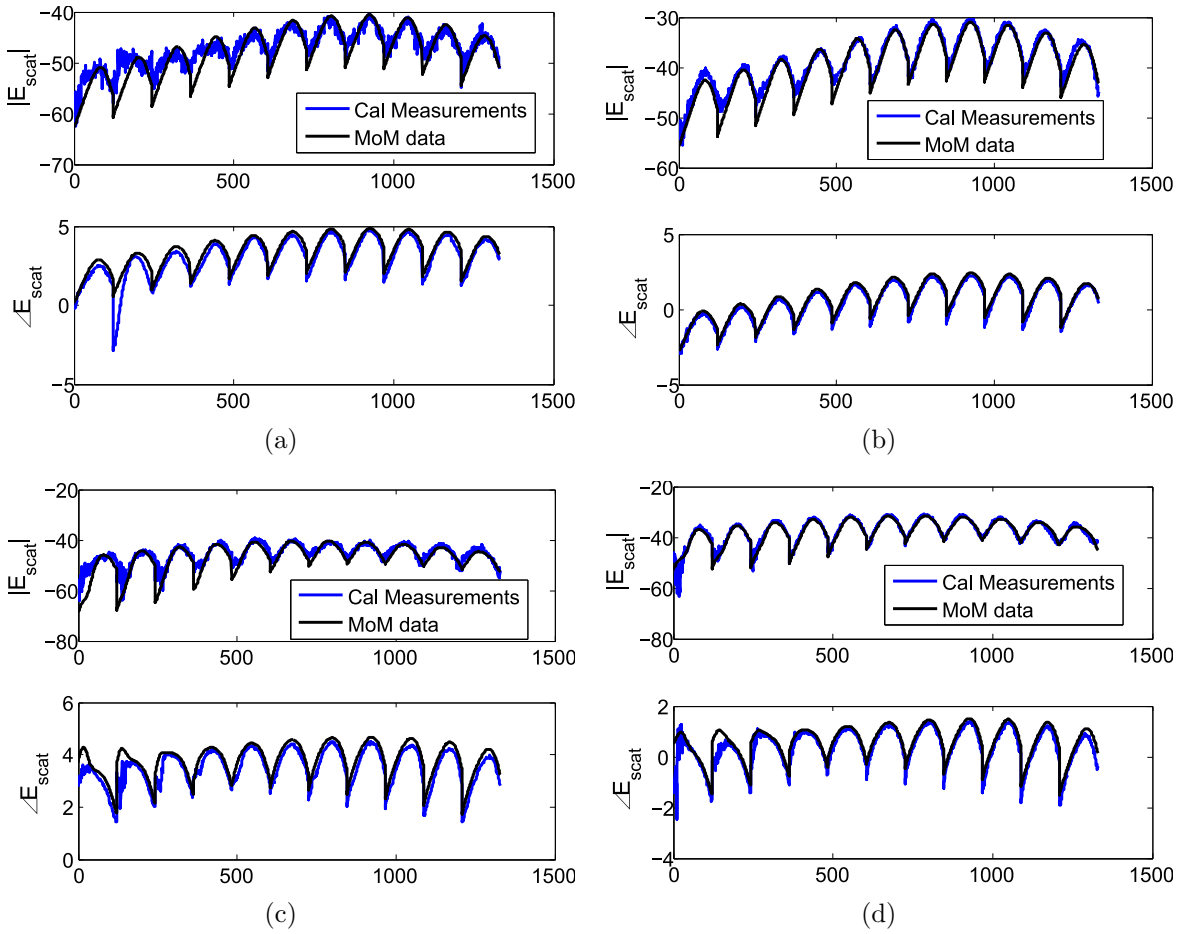

Figure 5.19 Comparison of the calibrated measurements and MoM scattered fields for the four measured cases. (a) 1 cylinder thick phantom. (b) 1 cylinder thin phantom. (c) 2 cylinders thick phantom. (d) 2 cylinders thin phantom.

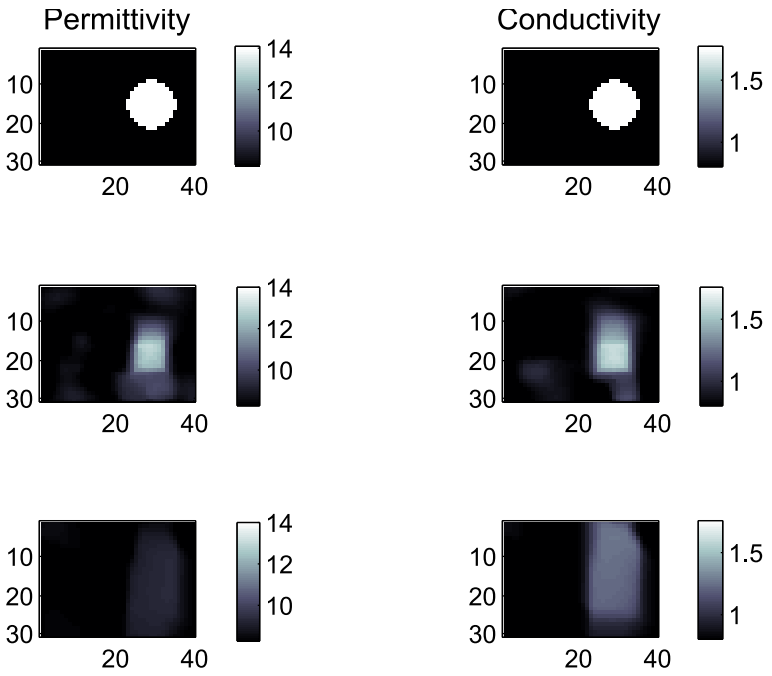

(a)

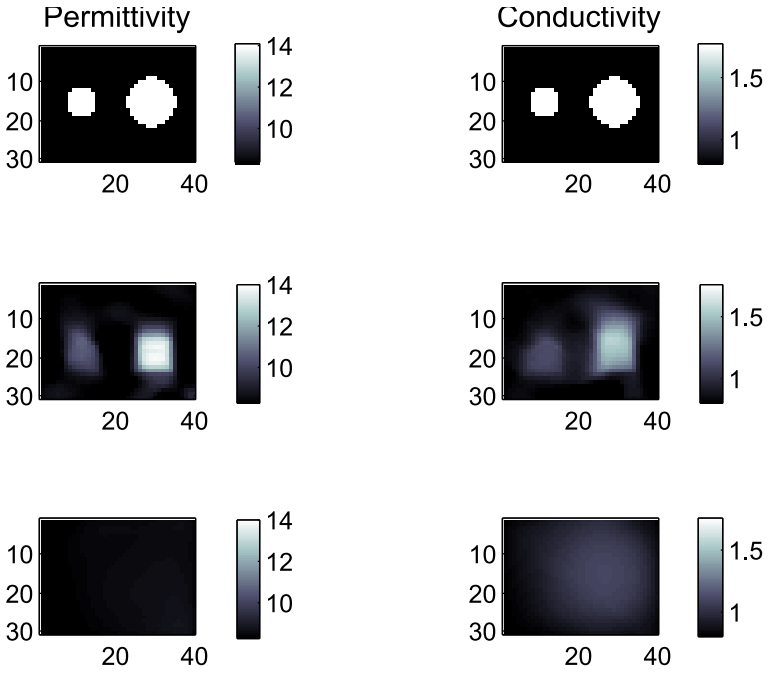

(b)

Figure 5.20 Reconstructed results for the thick phantom ($W = W_1$), each row of the configure contains from top to bottom, the original OUT, the reconstruction using synthetically generated measurements for a SNR of 40dB and the reconstruction from the measured data. (a) 1 Cylinder. (b) 2 Cylinders.

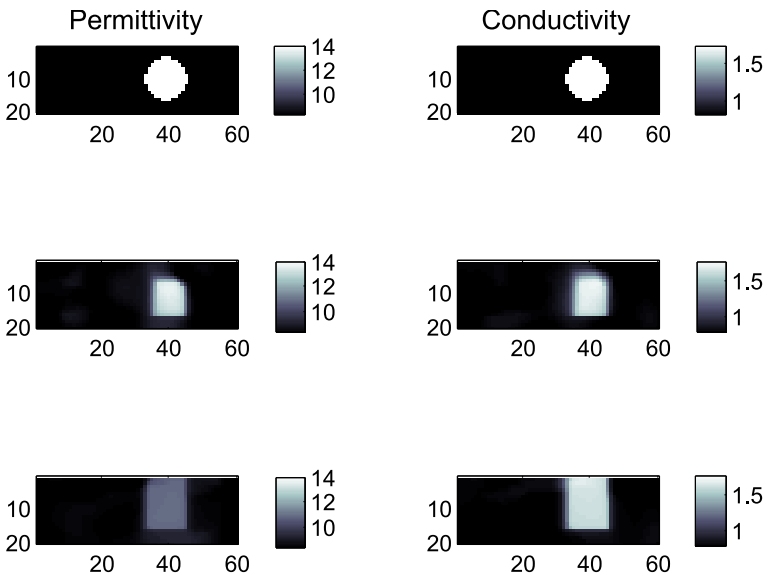

(a)

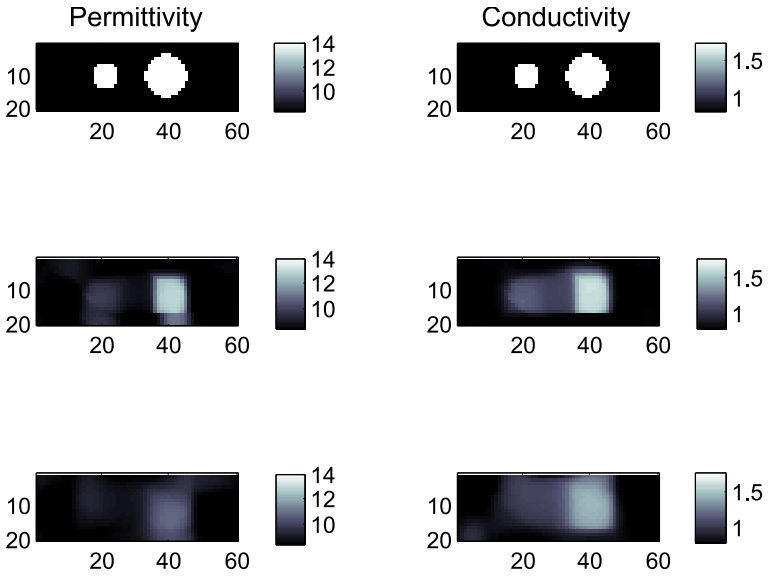

(b)

Figure 5.21 Reconstructed results for the thin phantom ($W = W_2$), each row of the configure contains from top to bottom, the original OUT, the reconstruction using synthetically generated measurements for a SNR of 40dB and the reconstruction from the measured data. (a) 1 Cylinder. (b) 2 Cylinders.

CHAPTER 6

CONCLUSION

6.1 Conclusion

The main objective of this thesis was to study alternative configurations of the MT problem applied to breast cancer detection and to see its impact on the obtained reconstructed images, in order to find an optimum configuration of the Tx and Rx antennas that maximizes the quality of the cited images.

Different configurations based on breast compression were studied in Chapter 3, namely the camera and waveguide configuration, and a rigurous study comparing the performances of compression versus non compression configurations was performed. This study included a simplified analysis of the mechanical deformation of breast tissues under compression. The results of the study showed that an enhancement in the reconstructed images is obtained through compression of the breast. This enhancement is due to the measurement of the evanescent component of the scattered field which attenuates rapidly away from the scatterer. The enhancement of the images was dependent of the SNR in the system, and it was found in our particular case that a SNR of 20 dB or more was needed to have a better result than one obtained using a classical circular MT configuration.

The configurations based on breast compression requires the measurement of the scattered fields very close to the OUT. This represents a challenge since the scattered fields are very weak compared to the incident or total field, moreover the antenna itself used for the measurement and the associated cables to connect to the measurement equipment, can disturb the quantity to be measured. For this purpose, a measurement system based on the modulated scattering technique using optically modulated probes was developed in (Memarzadeh-Tehran (2010)). In the first part of Chapter 4, a wideband optically modulated near-field probe is presented. Using the new design, the bandwidth of the probe was increased from 46% to more than 100%, having a usable bandwidth from 1.1GHz to 3.6GHz. Moreover, the implementation of the probe in a perforated alumina substrate, reduced the potential invasiveness of the probe. In the second part of Chapter 4, the optical MST system is used in a preliminar validation of the waveguide configuration. A fixture made of plexyglass was constructed, where different liquids can be introduced inside to simulate different matching liquids or parts of the human breast. In our case, glycerine was used in the experiment and two different modes can propagate inside this dielectric waveguide for both the TE and TM mode. Two different

different feed structures capable of launching TE and TM modes in the dielectric waveguide by using an array of two printed antennas were designed. Antipodal dipole antennas are used in the case of the TE modes and patch antennas in the case of the TM modes. It was shown that by changing the phase shift between the antennas different modes can be launched in the waveguide. Finally, the scattered field produced by an air-filled tube was measured for the different modes and different polarizations and a good agreement between the measured and simulated results was obtained.

Quantitative imaging using the proposed planar configurations was explored in Chapter 5 for both the waveguide and camera configurations. A modified fixture was constructed for quantitative imaging using the waveguide configuration, in order to increase the number of independent illuminations. The measurements where performed both using a classical near-field probe and the optically modulated system, and it was found out that classical near-field measurements using a VNA can provide better measurements in terms of the SNR when the same power level is applied to the Tx antenna. On the other hand, since calibration of the scattered field measurements is needed in order to use 2D reconstruction algorithms, the non-invasiveness property of the modulated approach loses some of its advantages. Quantitative images of very simple scatterers were obtained for the TE polarization, which corresponds to a scalar 2D TM case in the inverse scattering notation. The position of the scatterers was succesfully obtained in the reconstructed images, however, some problems related to the calibration and signal level from one of the modes were identified and were consistent with the problems encountered in the preliminar validation of the configuration. On the other hand, the camera configuration was used to test the effect of breast compression experimentally. For this purpose, two different phantoms representing two different levels of compression were constructed and measured. The results showed the advantage of breast compression in the case of this configuration, both in terms of the SNR in the measurements, as well as, in terms of the quality of the reconstructed images.

6.1.1 Contributions of this thesis

The main contributions of the author of this thesis can be summarized as :

- A rigurous study of the effect of breast compression in the quality of reconstructed images in MT applied to breast cancer detection, presented in Chapter 3. The study takes also into account, in a simplified manner, the mechanical deformation of breast tissues under compression. The results of the study showed which conditions allow the obtention of enhanced reconstructed images using this approach and some guidelines for the implementation of practical fixtures.
- An efficient way to attack the problem of an inhomogeneous background resulting

from compression configurations, in which, the homogeneous Green's function approach would require a huge overhead in the computations required both in the direct and inverse scattering problem. The derivation of this inhomogeneous Green's function is summarized in Section 3.4. This approach also allows the introduction of *a priori* information directly in the Green's function of the problem.

- A procedure to model near-field probes based on the modulated scattering technique using full-wave commercially available simulators. This procedure was used in the design of an enhanced optically modulated scattering probe for near-field measurements in order to reduce the perturbation effect of the probe on the measurements.
- The practical implementation of the dielectric waveguide configuration, including the design of a test fixture, surface wave launchers and the validation using very simple scatterers detailed in Section 4.3.
- Measured quantitative images for both the waveguide and camera configurations in simplified phantoms.
- An experimental validation of the effect of breast compression using the camera configuration in a simplified phantom.

6.1.2 List of publications

Journal Papers

1. A. Diaz-Bolado, P.A. Barriere, J.J. Laurin, "Study of Microwave Tomography Measurement Setup Configurations for Breast Cancer Detection based on Breast Compression," in preparation.
2. A. Diaz-Bolado, H. Memarzadeh-Tehran, J.J. Laurin, "Practical implementation of a Dielectric Waveguide Configuration for Microwave Tomography applied to Breast Cancer Detection," submitted to IEEE Transactions on Microwave Theory and Techniques.
3. A. Diaz-Bolado, J.J Laurin, " Experimental Validation of the Effect of Compression on simplified Phantoms in Microwave Tomography applied to Breast Cancer Detection, " IEEE Antennas and Wireless Propagation Letters. To appear in 2013.
4. H. Memarzadeh-Tehran, A. Diaz-Bolado, J.J. Laurin, R. Kashyap,"Bandwidth Improvement in a Resonant Optical MST-Probe Applicable to Near-Field Imaging," IEEE Antennas and Wireless Propagation Letters, vol. 10, pp. 411-414, 2011.

Peer-reviewed Conference Papers

1. A. Diaz-Bolado, T. Henriksson, P.A. Barriere, H. Memarzadeh-Tehran, N. Joachimowicz, C. Conessa, A. Joisel, B. Duchene, J.J. Laurin and J.C. Bolomey,"Towards a Pla-

nar Microwave Tomography System for Early Stage Breast Cancer Detection," *XXX URSI General Assembly*, Istambul, Turkey, August, 2011.

2. A. Diaz-Bolado, P.A. Barriere, J.J. Laurin,"On the Effect of Breast Compression and Measurement Setup Configuration in Microwave Tomography for Breast Cancer Detection ," *IEEE AP-S symposium*, Spokane, U.S.A, July 3-9, 2011. (Selected finalist for the Student Paper Competition)
3. A. Diaz-Bolado and J.J. Laurin,"A New Configuration for Enhancing Contrast in Microwave Tomography Applied to Breast Cancer Detection," *USNC-URSI National Radio Science Meeting*, San Diego, U.S.A, July 5-12, 2008.

6.2 Future Work

In this section, we will propose some future directions that would complete or continue the work presented in this thesis.

Measurement Configurations

In this work, several new configurations for the measurement setup in MT for breast cancer detection have been presented. The waveguide configuration has shown a great potential, however some drawbacks have been identified during this thesis. An interesting alternative could be to substitute the material of the compression plates from dielectric to metallic. In such a case, the dielectric waveguide becomes a parallel-plate waveguide also capable of guiding different TE and TM modes. This new configuration can present several advantages, such as, the reduction of noise and perturbations from the surrounding environment, thus increasing the SNR and an increased confinement of the field in the region of interest.

A preliminar version of an array of active vertical probes to be used in a parallel plate waveguide was developed in our research group. A photograph of the developed prototype is shown in Figure 6.1. It consists in a series of monopoles, fabricated from the inner conductor of a coaxial cable, each probe is then connected to a low noise amplifier (LNA). A total of eight probes was fabricated, where the eight outputs were combined using two 4 :1 Wilkinson combiners and an additional stage of a 2 :1 combiner. The signal from each one of the probes was selected by switching on and off the bias of the amplifiers.

Another interesting characteristic of this configuration, is that only the normal component of the scattered field excites the probes due to the proximity of the metallic plats of the waveguide. This fact is an advantage compared to open configurations, where in the case of 2D TE or 3D formulation of the inverse scattering problem, there is a need to measure multiple polarizations of the scattered field in order to capture all of the information from

the OUT. This advantage should be verified using an inversion code capable of handling one of the cited formulations, as well as, an electromagnetic code that takes into account the particularities of the configuration.

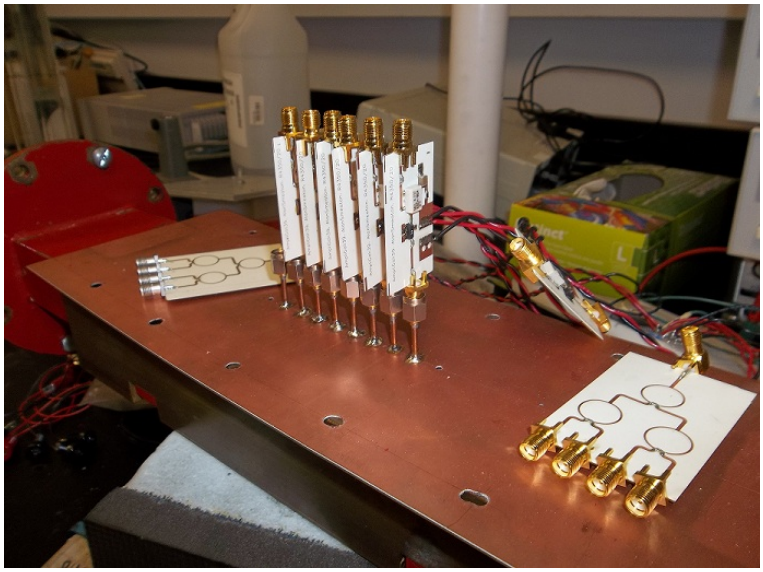

Figure 6.1 Photograph of the developed array of active probes mounted on a WR-284 metallic waveguide.

Finally, the configurations studied in this thesis considered the illumination of the OUT using a series of Tx antennas and the measurement of the scattered fields using an array of near-field probes. Another interesting approach that could be envisaged is the implementation of a planar array of Tx/Rx antennas that could have the advantage of breast compression shown in this thesis, combined with a complete multistatic setup provided by the flexibility of the Tx/Rx array.

Reconstruction Algorithms

In this thesis, the inversion algorithm presented in (Barriere *et al.* (2011)) and based in the well known CSI formulation has been used for obtaining all the reconstruction results. The algorithm is implemented for the scalar single frequency 2D TM case, however, in order to prove the validity of the MT technique in a clinical breast cancer detection application, a 3D multifrequency version of the algorithm should be implemented. In a 3D case, the complexity of the inverse scattering problem increases a lot, due to the increase in the number of unknowns of the problem, as well as, the vectorial nature of the electromagnetic fields. There exists in the literature different attempts to improve the efficiency of the inversion algorithms, such as the reduction of the number of unknowns of the problem using patient

specific basis functions (Winters *et al.* (2009)) or alternative formulations (Barriere (2008)). Moreover, other electromagnetic computational techniques such as the Multilevel Fast Multipole technique (Song *et al.* (1997)) in the case of the MoM can be used to accelerate the resolution of the forward scattering problem and thus enhance the efficiency of the inversion algorithms.

On the other hand, the configurations presented in this work were designed in order to be compatible with the geometry of a standard X-ray mammography setup. A combined approach of both techniques should be implemented in the inversion algorithm. For this purpose there exists different possibilities, the mammography resulting images can be used as *a priori* information in the form of an initial guess for the inversion, it can be used as an inhomogeneous background where the *a priori* information is included in the Green's function and incident field of the problem or we can think of an hybrid inversion algorithm which takes into account the physics of both techniques.

REFERENCES

ABDUL-RAZZAK, M., HARDWICK, B., HEY-SHIPTON, G., MATTHEWS, P., MONSON, J. et KESTER, R. (1987). Microwave thermography for medical applications. *Physical Science, Measurement and Instrumentation, Management and Education - Reviews, IEE Proceedings A*, 134, 171 –174.

ABUBAKAR, A., VAN DEN BERG, P. M. et MALLORQUI, J. J. (2002). Imaging of biomedical data using a multiplicative regularized contrast source inversion method. 50, 1761–1771.

ADLER, A. et GUARDO, R. (1996). Electrical impedance tomography : regularized imaging and contrast detection. *Medical Imaging, IEEE Transactions on*, 15, 170 –179.

ALEXOPOULOS, N., KATEHI, P. et RUTLEDGE, D. (1983). Substrate optimization for integrated circuit antennas. *Microwave Theory and Techniques, IEEE Transactions on*, 31, 550 –557.

ALI, M. et MOGHADDAM, M. (2010). 3d nonlinear super-resolution microwave inversion technique using time-domain data. *Antennas and Propagation, IEEE Transactions on*, 58, 2327 –2336.

AMINEH, R., MOUSSAKHANI, K., XU, H., DADASH, M., BASKHAROUN, Y., LIU, L. et NIKOLOVA, N. (2011a). Practical issues in microwave raster scanning. *Antennas and Propagation (EUCAP), Proceedings of the 5th European Conference on*. 2901 –2905.

AMINEH, R. K., RAVAN, M., TREHAN, A. et NIKOLOVA, N. K. (2011b). Near-field microwave imaging based on aperture raster scanning with tem horn antennas. 59, 928–940.

ASHTARI, A., NOGHANIAN, S., SABOUNI, A., ARONSSON, J., THOMAS, G. et PISTORIUS, S. (2010). Using a priori information for regularization in breast microwave image reconstruction. 57, 2197–2208.

BALANIS, C. A. (1989). *Advanced Engineering Electromagnetics*. Wiley.

BARBER, D. C. et BROWN, B. H. (1984). Applied potential tomography. *Journal of Physics E : Scientific Instruments*, 17, 723.

BARDATI, F. et IUDICELLO, S. (2008). Modeling the visibility of breast malignancy by a microwave radiometer. *Biomedical Engineering, IEEE Transactions on*, 55, 214 –221.

BARRIERE, P. A. (2008). *Developpement d'algorithmes d'inversion rapides et propositions relatives a la configuration du montage de mesures dans un contexte de Tomographie Micro-ondes appliquee a la detection du cancer du sein*. Thèse de doctorat, Ecole Polytechnique de Montreal.

BARRIERE, P.-A., IDIER, J., GOUSSARD, Y. et LAURIN, J.-J. (2007). 3-term optimization criterion for faster inversion in microwave tomography. *Biomedical Imaging : From Nano to Macro, 2007. ISBI 2007. 4th IEEE International Symposium on*. 225 –228.

BARRIERE, P.-A., IDIER, J., LAURIN, J.-J. et GOUSSARD, Y. (2011). Contrast source inversion method applied to relatively high contrast objects. *Inverse Problems*, 27, 075012.

BAZERGUI, A., BUI-QUOC, T., BIRON, A., MCINTIYRE, G. et LABERGE, C. (1993). *Resistance des Materiaux*. Editions de l'Ecole Polytechnique de Montreal.

BINDU, G., LONAPPAN, A., THOMAS, V., HAMSAKKUTTY, V., AANANDAN, C. K. et MATHEW, K. T. (2004). Microwave characterization of breast-phantom materials. *Microwave and Optical Technology Letters*, 43, 506–508.

BOAS, D., BROOKS, D., MILLER, E., DIMARZIO, C., KILMER, M., GAUDETTE, R. et ZHANG, Q. (2001). Imaging the body with diffuse optical tomography. *Signal Processing Magazine, IEEE*, 18, 57 –75.

BOLOMEY, J.-C. et GARDIOL, F. E. (2001). *Engineering Applications of the Modulated Scattering Technique*. Artech House.

BRADLEY, C., COLLINS, P., FORTUNY-GUASCH, J., HASTRITER, M., NESTI, G., TERZUOLI, A.J., J. et WILSON, K. (2005). An investigation of bistatic calibration techniques. *Geoscience and Remote Sensing, IEEE Transactions on*, 43, 2185 – 2191.

BUCCI, O. et FRANCESCHETTI, G. (1989). On the degrees of freedom of scattered fields. *Antennas and Propagation, IEEE Transactions on*, 37, 918 –926.

BUCCI, O. M., CROCCO, L. et ISERNIA, T. (1999). Improving the reconstruction capabilities in inverse scattering problems by exploitation of close-proximity setups. *J. Opt. Soc. Am. A*, 16, 1788–1798.

BUCCI, O. M., CROCCO, L., ISERNIA, T. et PASCAZIO, V. (2001). Subsurface inverse scattering problems : quantifying, qualifying, and achieving the available information. 39, 2527–2538.

CARR, K. (1989). Microwave radiometry : its importance to the detection of cancer. *Microwave Theory and Techniques, IEEE Transactions on*, 37, 1862 –1869.

CCS (2011). Breast cancer statistics at a glance.

CHATTERJEE, A., KEMPEL, L. et VOLAKIS, J. (1998). *Finite Element Method Electromagnetics :Antennas, Microwave Circuits, and Scattering Applications*. Wiley-IEEE Press.

CHEW, W. et WANG, Y. (1990). Reconstruction of two-dimensional permittivity distribution using the distorted born iterative method. *Medical Imaging, IEEE Transactions on*, 9, 218 –225.

CHEW, W. C. (1999). *Waves and Fields in Inhomogeneous Media*. Wiley-IEEE Press.

CHOI, M. H., KAO, T.-J., ISAACSON, D., SAULNIER, G. et NEWELL, J. (2007). A reconstruction algorithm for breast cancer imaging with electrical impedance tomography in mammography geometry. *Biomedical Engineering, IEEE Transactions on*, 54, 700 –710.

CRADDOCK, I. J., KLEMM, M., LEENDERTZ, J., PREECE, A. W. et BENJAMIN, R. (2008). Development and application of a uwb radar system for breast imaging. *Proc. Loughborough Antennas and Propagation Conf. LAPC 2008*. 24–27.

CRADDOCK, I. J., PREECE, A., LEENDERTZ, J., KLEMM, M., NILAVALAN, R. et BENJAMIN, R. (2006). Development of a hemi-spherical wideband antenna array for breast cancer imaging. *Proc. First European Conf. Antennas and Propagation EuCAP 2006*. 1–5.

CROCCO, L. et LITMAN, A. (2009). On embedded microwave imaging systems : retrievable information and design guidelines. *Inverse Problems*, 25, 065001.

CROTEAU, J., SILL, J., WILLIAMS, T. et FEAR, E. (2009). Phantoms for testing radar-based microwave breast imaging. *Antenna Technology and Applied Electromagnetics and the Canadian Radio Science Meeting, 2009. ANTEM/URSI 2009. 13th International Symposium on*. 1 –4.

CST (2011). *CST Studio Suite Online Help*.

DIAZ-BOLADO, A., BARRIERE, P.-A. et LAURIN, J.-J. (2011a). On the effect of breast compression and measurement setup configuration in microwave tomography for breast cancer detection. *IEEE International Symposium on Antennas and Propagation (APSURSI)*. 714 –717.

DIAZ-BOLADO, A., HENRIKSSON, T., BARRIERE, P.-A., MEMARZADEH-TEHRAN, H., JOACHIMOWICZ, N., CONESSA, C., JOISEL, A., DUCHENE, B., LAURIN, J.-J. et BOLOMEY, J.-C. (2011b). Towards a planar microwave tomography system for early stage breast cancer detection. *XXXth URSI General Assembly and Scientific Symposium*. 1 –4.

DIAZ-BOLADO, A. et LAURIN, J.-J. (2008). A new configuration for enhancing contrast in microwave tomography applied to breast cancer detection. *USNC-URSI National Radio Science Meeting, San Diego, U.S.A.*

DONG, Q., ZHAN, H. et RAPPAPORT, C. (2007). Efficient 3d finite difference frequency-domain modeling of scattering in lossy half-space geometries. 1789 –1792.

DUCHÊNE, B., JOISEL, A. et LAMBERT, M. (2004). Nonlinear inversions of immersed objects using laboratory-controlled data. *Inverse Problems*, 20, S81.

ELASOUED, R.A., L. J.-J. G. Y. (2004). Design and characterization of a broadband near-field probe. *ANTEM 2004*.

ELEFTHERIADES, G. et QIU, M. (2002). Efficiency and gain of slot antennas and arrays on thick dielectric substrates for millimeter-wave applications : a unified approach. *Antennas and Propagation, IEEE Transactions on*, 50, 1088 – 1098.

FANG, Q., CARP, S., SELB, J., BOVERMAN, G., ZHANG, Q., KOPANS, D., MOORE, R., MILLER, E., BROOKS, D. et BOAS, D. (2009). Combined optical imaging and mammography of the healthy breast : Optical contrast derived from breast structure and compression. *IEEE Transactions on Medical Imaging*, 28, 30 –42.

FANG, Q., MEANEY, P. M. et PAULSEN, K. D. (2006). Singular value analysis of the jacobian matrix in microwave image reconstruction. 54, 2371–2380.

FANG, Q., MEANEY, P. M. et PAULSEN, K. D. (2010). Viable three-dimensional medical microwave tomography : Theory and numerical experiments. 58, 449–458.

FATEMI, M., MANDUCA, A. et GREENLEAF, J. (2003). Imaging elastic properties of biological tissues by low-frequency harmonic vibration. *Proceedings of the IEEE*, 91, 1503 – 1519.

FEAR, E., HAGNESS, S., MEANEY, P., OKONIEWSKI, M. et STUCHLY, M. (2002). Enhancing breast tumor detection with near-field imaging. *IEEE Microwave Magazine*, 3, 48 –56.

FEAR, E., MEANEY, P. et STUCHLY, M. (2003). Microwaves for breast cancer detection ? *Potentials, IEEE*, 22, 12 – 18.

FHAGER, A., HASHEMZADEH, P. et PERSSON, M. (2006). Reconstruction quality and spectral content of an electromagnetic time-domain inversion algorithm. 53, 1594–1604.

FHAGER, A., KOSTER, J., RUBAEK, T. et PERSSON, M. (2011). Modeling and reconstruction in a 3d microwave imaging system. *General Assembly and Scientific Symposium, 2011 XXXth URSI*. 1 –4.

FHAGER, A., MCKELVEY, T. et PERSSON, M. (2010). Stroke detection using a broadband microwave antenna system. *Antennas and Propagation (EuCAP), 2010 Proceedings of the Fourth European Conference on*. 1 –3.

FHAGER, A. et PERSSON, M. (2011). A microwave measurement system for stroke detection. *Antennas and Propagation Conference (LAPC), 2011 Loughborough*. 1 –2.

FOX, C. J., MEANEY, P. M., L., P. et PAULSEN, K. D. (2008). Characterization of a monopole antenna in a lossy medium for microwave breast computed tomography. *International Journal of Antennas and Propagation*, 9.

FRANCHOIS, A., JOISEL, A., PICHOT, C. et BOLOMEY, J.-C. (1998). Quantitative microwave imaging with a 2.45-ghz planar microwave camera. *IEEE Transactions on Medical Imaging*, 17, 550 –561.

FRANZA, O., JOACHIMOWICZ, N. et BOLOMEY, J.-C. (2002). Sics : a sensor interaction compensation scheme for microwave imaging. 50, 211–216.

FREUNDORFER, A., BEKHEIT, M. et ANTAR, Y. (2006). Measurements of a compact surface wave launcher array with application to single frequency beam steering leaky wave antennas. *Microwave Conference, 2006. APMC 2006. Asia-Pacific*. 824 –827.

GABRIEL, C., GABRIEL, S. et CORTHOUT, E. (1996a). The dielectric properties of biological tissues : I. literature survey. *Physics in Medicine and Biology*, 41, 2231.

GABRIEL, S., LAU, R. W. et GABRIEL, C. (1996b). The dielectric properties of biological tissues : Ii. measurements in the frequency range 10 hz to 20 ghz. *Physics in Medicine and Biology*, 41, 2251.

GABRIEL, S., LAU, R. W. et GABRIEL, C. (1996c). The dielectric properties of biological tissues : Iii. parametric models for the dielectric spectrum of tissues. *Physics in Medicine and Biology*, 41, 2271.

GAO, C. et XIANG, X.-D. (1998). Quantitative microwave near-field microscopy of dielectric properties. *Review of Scientific Instruments*, 69, 3846–3851.

GHASR, M. T., ABOU-KHOUSA, M. A., KHARKOVSKY, S., ZOUGHI, R. et POMMERENKE, D. (2008). A novel 24 ghz one-shot, rapid and portable microwave imaging system. *Proc. IEEE Instrumentation and Measurement Technology IMTC 2008*. 1798–1802.

GILMORE, C., MOJABI, P., ZAKARIA, A., OSTADRAHIMI, M., KAYE, C., NOGHANIAN, S., SHAFAI, L., PISTORIUS, S. et LOVETRI, J. (2010). A wideband microwave tomography system with a novel frequency selection procedure. 57, 894–904.

GRZEGORCZYK, T., MEANEY, P., KAUFMAN, P., DI FLORIO-ALEXANDER, R. et PAULSEN, K. (2012). Fast 3-d tomographic microwave imaging for breast cancer detection. *Medical Imaging, IEEE Transactions on*, 31, 1584 –1592.

HARRINGTON, R. F. (1968). *Field Computation by Moment Method*. McMillan.

HENRIKSSON, T., JOACHIMOWICZ, N., CONESSA, C. et BOLOMEY, J.-C. (2010). Quantitative microwave imaging for breast cancer detection using a planar 2.45 ghz system. *IEEE Transactions on Instrumentation and Measurement*, 59, 2691 –2699.

HENRIKSSON, T., KLEMM, M., GIBBINS, D., LEENDERTZ, J., HORSEMAN, T., PREECE, A., BENJAMIN, R. et CRADDOCK, I. (2011). Clinical trials of a multistatic uwb radar for breast imaging. *Antennas and Propagation Conference (LAPC), 2011 Loughborough*. 1 –4.

JOFRE, L., HAWLEY, M., BROQUETAS, A., DE LOS REYES, E., FERRANDO, M. et ELIAS-FUSTE, A. (1990). Medical imaging with a microwave tomographic scanner. *Biomedical Engineering, IEEE Transactions on*, 37, 303 –312.

JOINES, W. T., ZHANG, Y., LI, C. et JIRTLE, R. L. (1994). The measured electrical properties of normal and malignant human tissues from 50 to 900 mhz. *Medical Physics*, 21, 547–550.

KELLNER, A., NELSON, T., CERVINO, L. et BOONE, J. (2007). Simulation of mechanical compression of breast tissue. *IEEE Trans. Biomed. Eng*, 54, 1885 –1891.

KIM, Y. J., JOFRE, L., DE FLAVIIS, F. et FENG, M. (2003). Microwave reflection tomographic array for damage detection of civil structures. *Antennas and Propagation, IEEE Transactions on*, 51, 3022 – 3032.

KLEISMIT, R., KAZIMIERCZUK, M. et KOZLOWSKI, G. (2006). Sensitivity and resolution of evanescent microwave microscope. *IEEE Transactions on Microwave Theory and Techniques*, 54, 639 – 647.

KLEMM, M., CRADDOCK, I., LEENDERTZ, J., PREECE, A. et BENJAMIN, R. (2009a). Radar-based breast cancer detection using a hemispherical antenna array-experimental results. *IEEE Trans. Antennas Propag.*, 57, 1692 –1704.

KLEMM, M., LEENDERTZ, J., GIBBINS, D., CRADDOCK, I., PREECE, A. et BENJAMIN, R. (2009b). Microwave radar-based breast cancer detection : Imaging in inhomogeneous breast phantoms. *Antennas and Wireless Propagation Letters, IEEE*, 8, 1349 –1352.

KLEMM, M., LEENDERTZ, J., GIBBINS, D., CRADDOCK, I., PREECE, A. et BENJAMIN, R. (2010). Microwave radar-based differential breast cancer imaging : Imaging in homogeneous breast phantoms and low contrast scenarios. *Antennas and Propagation, IEEE Transactions on*, 58, 2337 –2344.

LARSEN, L. E. et JACOBI, J. H. (1979). Microwave scattering parameter imagery of an isolated canine kidney. *Medical Physics*, 6, 394–403.

LARSEN, L. E. et JACOBI, J. H. (1985). *Medical applications of microwave imaging*. IEEE Press.

LAZEBNIK, M., MADSEN, E. L., FRANK, G. R. et HAGNESS, S. C. (2005). Tissue-mimicking phantom materials for narrowband and ultrawideband microwave applications. *Phys Med Biol*, 50, 4245–4258.

LAZEBNIK, M., MCCARTNEY, L., POPOVIC, D., WATKINS, C. B., LINDSTROM, M. J., HARTER, J., SEWALL, S., MAGLIOCCO, A., BOOSKE, J. H., OKONIEWSKI, M. et HAGNESS, S. C. (2007a). A large-scale study of the ultrawideband microwave dielectric properties of normal breast tissue obtained from reduction surgeries. *Physics in Medicine and Biology*, 52, 2637.

LAZEBNIK, M., POPOVIC, D., MCCARTNEY, L., WATKINS, C. B., LINDSTROM, M. J., HARTER, J., SEWALL, S., OGILVIE, T., MAGLIOCCO, A., BRESLIN, T. M., TEMPLE, W., MEW, D., BOOSKE, J. H., OKONIEWSKI, M. et HAGNESS, S. C. (2007b). A large-scale study of the ultrawideband microwave dielectric properties of normal, benign and malignant breast tissues obtained from cancer surgeries. *Physics in Medicine and Biology*, 52, 6093.

LAZEBNIK, M., WATKINS, C. B., HAGNESS, S. C., BOOSKE, J. H., POPOVIC, D., MCCARTNEY, L., OKONIEWSKI, M., LINDSTROM, M. J., BRESLIN, T. M., HARTER, J., SEWALL, S., TEMPLE, W., MEW, D., MAGLIOCCO, A. et OGILVIE, T. (2007c). The dielectric properties of normal and malignant breast tissue at microwave frequencies : analysis, conclusions, and implications from the wisconsin/calgary study. *Proc. IEEE Antennas and Propagation Society Int. Symp.* 2172–2175.

LI, D., MEANEY, P. M., RAYNOLDS, T., PENDERGRASS, S. A., FANNING, M. W. et PAULSEN, K. D. (2004). Parallel-detection microwave spectroscopy system for breast imaging. *Review of Scientific Instruments*, 75, 2305–2313.

LI, X., HAGNESS, S. C., VAN VEEN, B. D. et VAN DER WEIDE, D. (2003). Experimental investigation of microwave imaging via space-time beamforming for breast cancer detection. *Proc. IEEE MTT-S Int. Microwave Symp. Digest.* vol. 1, 379–382.

LITMAN, A., GEFFRIN, J.-M. et TORTEL, H. (2010). On the calibration of a multistatic scattering matrix measured by a fixed circular array of antennas. *Progress In Electromagnetics Research*, 110, 1–21.

MASHAL, A., SITHARAMAN, B., LI, X., AVTI, P. K., SAHAKIAN, A. V., BOOSKE, J. H. et HAGNESS, S. C. (2010). Toward carbon-nanotube-based theranostic agents for microwave detection and treatment of breast cancer : Enhanced dielectric and heating response of tissue-mimicking materials. 57, 1831–1834.

MEANEY, P., FANNING, M., LI, D., POPLACK, S. et PAULSEN, K. (2000). A clinical prototype for active microwave imaging of the breast. *IEEE Trans. Microw. Theory Tech*, 48, 1841 – 1853.

MEANEY, P., PAULSEN, K. et CHANG, J. (1998a). Near-field microwave imaging of biologically-based materials using a monopole transceiver system. *Microwave Theory and Techniques, IEEE Transactions on*, 46, 31 –45.

MEANEY, P. M., PAULSEN, K. D. et CHANG, J. T. (1998b). Near-field microwave imaging of biologically-based materials using a monopole transceiver system. 46, 31–45.

MEMARZADEH-TEHRAN, H. (2010). *Non-Invasive Near-Field measurement setup based on Modulated Scatterer Technique applied to Microwave Tomography.* Thèse de doctorat, Ecole Polytechnique de Montreal.

MEMARZADEH-TEHRAN, H., DIAZ-BOLADO, A., LAURIN, J.-J. et KASHYAP, R. (2011). Bandwidth improvement in a resonant optical mst-probe applicable to near-field imaging. *Antennas and Wireless Propagation Letters, IEEE*, 10, 411 –414.

MEMARZADEH-TEHRAN, H., LAURIN, J.-J. et KASHYAP, R. (2010). Optically modulated probe for precision near-field measurements. *IEEE Transactions on Instrumentation and Measurement*, 59, 2755 –2762.

MICHALSKI, K. et MOSIG, J. (1997). Multilayered media green's functions in integral equation formulations. *Antennas and Propagation, IEEE Transactions on*, 45, 508 –519.

MIGA, M., PAULSEN, K., LEMERY, J., EISNER, S., HARTOV, A., KENNEDY, F. et ROBERTS, D. (1999). Model-updated image guidance : initial clinical experiences with gravity-induced brain deformation. *IEEE Transactions on Medical Imaging*, 18, 866 –874.

MOJABI, P., GILMORE, C., OSTADRAHIMI, M., ZAKARIA, A. AN JEFFREY, I., LOVETRI, J., PISTORIUS, S. et SHAFAI, L. (2011). Reduction of modelling error in microwave tomography : a review. *URSI National Radio Science Meeting, Spokane, WA, USA*.

MOSIG, J. R. et ITOH, T. (1989). Integral equation Technique. *Numerical Techniques for Microwave and Millimeter Wave Passive Structures*, Wiley. 133–214.

NCRP (2004). A guide to mammography and other breast imaging procedures. Rapport technique 149, National Council on Radiation Protection and Measurements (NCRP).

NOCEDAL, J. et WRIGHT, S. (2006). *Numerical Optimization*. Springer.

OMRANE, B. (2005). *Modelisation electromagnetique et technique de regularization adaptees a la Tomographie Micro-ondes de structures dielectriques realisee a l'aide de mesures en champ proche*. Mémoire de maîtrise, Ecole Polytechnique de Montreal.

OMRANE, B., GOUSSARD, Y. et LAURIN, J.-J. (2011). Constrained inverse near-field scattering using high resolution wire grid models. *Antennas and Propagation, IEEE Transactions on*, 59, 3710 –3718.

OMRANE, B., LAURIN, J.-J. et GOUSSARD, Y. (2006). Subwavelength-resolution microwave tomography using wire grid models and enhanced regularization techniques. 54, 1438–1450.

OSTADRAHIMI, M., MOJABI, P., GILMORE, C., ZAKARIA, A., NOGHANIAN, S., PISTORIUS, S. et LOVETRI, J. (2011). Analysis of incident field modeling and incident/scattered field calibration techniques in microwave tomography. *Antennas and Wireless Propagation Letters, IEEE*, 10, 900 –903.

OSTADRAHIMI, M., MOJABI, P., NOGHANIAN, S., SHAFAI, L., PISTORIUS, S. et LOVETRI, J. (2012). A novel microwave tomography system based on the scattering probe technique. *Instrumentation and Measurement, IEEE Transactions on*, 61, 379 –390.

PARKER, K., GAO, L., LERNER, R. et LEVINSON, S. (1996). Techniques for elastic imaging : a review. *Engineering in Medicine and Biology Magazine, IEEE*, 15, 52 –59.

PASTORINO, M. (2010). *Microwave Imaging*. Wiley.

PAULSEN, K. et MEANEY, P. (1999). Nonactive antenna compensation for fixed-array microwave imaging. i. model development. *IEEE Transactions on Medical Imaging*, 18, 496 –507.

PERKONS, A. F., QIAN, Y. et ITOH, T. (1998). Tm surface-wave power combining by a planar active-lens amplifier. 46, 775–783.

PERKONS, A. R. et ITOH, T. (1997). Te surface wave power combining by a planar 10-element active lens amplifier. *Proc. IEEE MTT-S Int. Microwave Symp. Digest*. vol. 2, 691–694.

PODILCHAK, S., FREUNDORFER, A. et ANTAR, Y. (2009). Surface-wave launchers for beam steering and application to planar leaky-wave antennas. *Antennas and Propagation, IEEE Transactions on*, 57, 355 –363.

POPOVIC, D., MCCARTNEY, L., BEASLEY, C., LAZEBNIK, M., OKONIEWSKI, M., HAGNESS, S. C. et BOOSKE, J. H. (2005). Precision open-ended coaxial probes for in vivo and ex vivo dielectric spectroscopy of biological tissues at microwave frequencies. 53, 1713–1722.

PORTER, E., FAKHOURY, J., OPRISOR, R., COATES, M. et POPOVIC, M. (2010). Improved tissue phantoms for experimental validation of microwave breast cancer detection. *Antennas and Propagation (EuCAP), 2010 Proceedings of the Fourth European Conference on*. 1 –5.

POULOS, A., MCLEAN, D., RICKARD, M. et HEARD, R. (2003). Breast compression in mammography : How much is enough ? *Australasian Radiology*, 47, 121–126.

PRESS, W. H., TEUKOLSKY, S. A., VETTERLING, W. T. et FLANNERY, B. P. (1988). *Numerical Recipes in C : The art of Scientific Computing*. Cambridge University Press.

RICHMOND, J. (1965). Scattering by a dielectric cylinder of arbitrary cross section shape. *Antennas and Propagation, IEEE Transactions on*, 13, 334 – 341.

SAMANI, A., BISHOP, J., LUGINBUHL, C. et PLEWES, D. B. (2003). Measuring the elastic modulus of ex vivo small tissue samples. *Physics in Medicine and Biology*, 48, 2183.

SCHLERETH, K.-H. et TACKE, M. (1990). The complex propagation constant of multilayer waveguides : an algorithm for a personal computer. *IEEE Journal of Quantum Electronics*, 26, 627 –630.

SCHULTZ, J. W., HOPKINS, E. J. et KUSTER, E. J. (2003). Near-field probe measurements of microwave scattering from discontinuities in planar surfaces. 51, 2361–2368.

SEMENOV, S., BULYSHEV, A., SOUVOROV, A., NAZAROV, A., SIZOV, Y., SVENSON, R., POSUKH, V., PAVLOVSKY, A., REPIN, P. et TATSIS, G. (2000). Three-dimensional microwave tomography : experimental imaging of phantoms and biological objects. *Microwave Theory and Techniques, IEEE Transactions on*, 48, 1071 –1074.

SEMENOV, S., SVENSON, R., BULYSHEV, A., SOUVOROV, A., NAZAROV, A., SIZOV, Y., PAVLOVSKY, A., BORISOV, V., VOINOV, B., SIMONOVA, G., STAROSTIN, A., POSUKH, V., TATSIS, G. et BARANOV, V. (1999). Three-dimensional microwave tomography : experimental prototype of the system and vector born reconstruction method. *Biomedical Engineering, IEEE Transactions on*, 46, 937 –946.

SEMENOV, S., SVENSON, R., POSUKH, V., NAZAROV, A., SIZOV, Y., BULYSHEV, A., SOUVOROV, A., CHEN, W., KASELL, J. et TATSIS, G. (2002). Dielectrical spectroscopy of canine myocardium during acute ischemia and hypoxia at frequency spectrum from 100 khz to 6 ghz. *Medical Imaging, IEEE Transactions on*, 21, 703 –707.

SHEA, J., KOSMAS, P., HAGNESS, S. et VAN VEEN, B. (2009). Contrast-enhanced microwave breast imaging. *Antenna Technology and Applied Electromagnetics and the Canadian Radio Science Meeting, 2009. ANTEM/URSI 2009. 13th International Symposium on*. 1 –4.

SILL, J. M. et FEAR, E. C. (2005). Tissue sensing adaptive radar for breast cancer detection - experimental investigation of simple tumor models. 53, 3312–3319.

SINKUS, R., TANTER, M., BERCOFF, J., SIEGMANN, K., PERNOT, M., ATHANASIOU, A. et FINK, M. (2008). Potential of mri and ultrasound radiation force in elastography : Applications to diagnosis and therapy. *Proceedings of the IEEE*, 96, 490 –499.

SMITH, G. (1981). Analysis of miniature electric field probes with resistive transmission lines. *Microwave Theory and Techniques, IEEE Transactions on*, 29, 1213 – 1224.

SONG, J., LU, C.-C. et CHEW, W. C. (1997). Multilevel fast multipole algorithm for electromagnetic scattering by large complex objects. *Antennas and Propagation, IEEE Transactions on*, 45, 1488 –1493.

SONG, L.-P. et LIU, Q. H. (2005). A new approximation to three-dimensional electromagnetic scattering. 2, 238–242.

SORRENTINO, R. (1989). The transverse resonance technique. *Numerical Techniques for Microwave and Millimeter-Wave Passive Structures*, Wiley-Interscience.

SOUBRET, A., RIPOLL, J. et NTZIACHRISTOS, V. (2005). Accuracy of fluorescent tomography in the presence of heterogeneities :study of the normalized born ratio. *Medical Imaging, IEEE Transactions on*, 24, 1377 –1386.

STANG, J. P. (2008). *A 3D Active Microwave Imaging System for Breast Cancer Screening.* Thèse de doctorat, Duke University.

STUTZMAN, W. L. et THIELE, G. A. (1998). *Antenna Theory and Design.* Wiley & Sons.

SUZUKI, E., ARAKAWA, S., TAKAHASHI, M., OTA, H., ARAI, K. et SATO, R. (2008). Visualization of poynting vectors by using electro-optic probes for electromagnetic fields. *Instrumentation and Measurement, IEEE Transactions on*, 57, 1014 –1022.

TAFLOVE, A. et HAGNESS, S. C. (2005). *Computational Electrodynamics : The Finite-Difference Time-Domain Method 3rd Ed.* Artech House.

TAI, C. T. (1994). *Dyadic Green Functions in Electromagnetic Theory.* Institute of Electrical & Electronics Engineers.

TARNUS, R., DÉROBERT, X. et PICHOT, C. (2004). Multifrequency microwave tomography between boreholes. *Microwave and Optical Technology Letters*, 42, 4–8.

TRUCHETTI, L. (2005). *Etude d'une approche nouvelle pour la Tomographie Micro-ondes et son application au Cancer du Sein.* Mémoire de maîtrise, Ecole Polytechnique de Montreal.

VAN DEN BERG, P. et ABUBAKAR, A. (2002). Inverse scattering and its applications to medical imaging and subsurface sensing. *Radio Sci. Bull*, 13–26.

VISSER, T., BLOK, H. et LENSTRA, D. (1995). Modal analysis of a planar waveguide with gain and losses. *Quantum Electronics, IEEE Journal of*, 31, 1803 –1810.

WHITT, M., ULABY, F., POLATIN, P. et LIEPA, V. (1991). A general polarimetric radar calibration technique. *Antennas and Propagation, IEEE Transactions on*, 39, 62 –67.

WILLIAMS, T. C., BOURQUI, J., CAMERON, T. R., OKONIEWSKI, M. et FEAR, E. C. (2011). Laser surface estimation for microwave breast imaging systems. 58, 1193–1199.

WINTERS, D., SHEA, J., KOSMAS, P., VAN VEEN, B. et HAGNESS, S. (2009). Three-dimensional microwave breast imaging : Dispersive dielectric properties estimation using patient-specific basis functions. *Medical Imaging, IEEE Transactions on*, 28, 969 –981.

WINTERS, D. W., VAN VEEN, B. D. et HAGNESS, S. C. (2006). Uwb microwave imaging for breast cancer detection : an algorithm for estimating the breast surface. *Proc. IEEE Antennas and Propagation Society Int. Symp. 2006.* 267–270.

XU, M. et WANG, L. (2002). Time-domain reconstruction for thermoacoustic tomography in a spherical geometry. *Medical Imaging, IEEE Transactions on*, 21, 814 –822.

XU, Y. et WANG, L. (2003). Effects of acoustic heterogeneity in breast thermoacoustic tomography. *Ultrasonics, Ferroelectrics and Frequency Control, IEEE Transactions on*, 50, 1134 –1146.

ZASTROW, E., DAVIS, S. K., LAZEBNIK, M., KELCZ, F., VAN VEEN, B. D. et HAGNESS, S. C. (2008). Development of anatomically realistic numerical breast phantoms with accurate dielectric properties for modeling microwave interactions with the human breast. 55, 2792–2800.

ZENG, X., FHAGER, A., LINNER, P., PERSSON, M. et ZIRATH, H. (2011). Experimental investigation of the accuracy of an ultrawideband time-domain microwave-tomographic system. *Instrumentation and Measurement, IEEE Transactions on*, 60, 3939 –3949.

ZHAO, M., SHEA, J., HAGNESS, S., VAN DER WEIDE, D., VAN VEEN, B. et VARGHESE, T. (2008). Numerical study of microwave scattering in breast tissue via coupled dielectric and elastic contrasts. *Antennas and Wireless Propagation Letters, IEEE*, 7, 247 –250.

ZHU, G., ORESHKIN, B., PORTER, E., COATES, M. et POPOVIC, M. (2009). Numerical breast models for commercial fdtd simulators. *Proc. 3rd European Conf. Antennas and Propagation EuCAP 2009*. 263–267.

ZHURBENKO, V. (2008). *Design of Microwave Camera for Breast Cancer Detection*. Thèse de doctorat, Technical University of Denmark.

ZHURBENKO, V., RUBAEK, T., KROZER, V. et MEINCKE, P. (2010). Design and realisation of a microwave three-dimensional imaging system with application to breast-cancer detection. *IET Microwaves, Antennas & Propagation*, 4, 2200–2211.

ZURCHER, J. et GARDIOL, F. E. (1995). *Broadband Patch Antennas*. Artech House.

ZWAMBORN, P. (1991). *Scattering by Objects with Electric Contrast*. Thèse de doctorat, Technische Universiteit Delft.

ANNEX A

Inverse problem solution using the CSI method

A.1 AR-CSI algorithm description

A variation of the well known CSI method proposed in (Barriere *et al.* (2011)) was used through this thesis. This modified version of the CSI algorithm tries to solve some defficiencies of the MR-CSI algorithm that are detailed in the previously mentioned reference. The main difference between this implementation and the previously presented MR-CSI method is the structure of the cost function to be minimized and the computation of the parameters of the algorithm. The minimization criteria now has the form :

$$F(X,W) = F_1 + \lambda F_2 + \lambda_r F_r \tag{A.1}$$

$$F_1(W) = \sum_{i=1}^{M} ||y_i - G_o w_i||^2 \tag{A.2}$$

$$F_2(X,W) = \sum_{i=1}^{n} ||X(E_i^{inc} + G_c w_i) - w_i||^2 \tag{A.3}$$

$$F_r = \frac{\Delta^2}{S} \sum_{p=1}^{n} \sqrt{|\nabla x_p^k|^2 + (\delta)^2} \tag{A.4}$$

In this approach the parameters of the algorithm are fixed for all the iterations and need to be previously determined depending on the object to be reconstructed or the measurement configuration. This approach might appear cumbersome compared to an algorithm with automatic parameter adjustment, however this approach is very common in the inverse problem literature. Additionally, the additive regularization provides an additional parameter, λ_r, to help in an accurate reconstruction of the OUT.

The minimization of the criteria shown in A.1 is made using a non-linear conjugate gradient (CG) algorithm (Nocedal et Wright (2006)). In this case the minimization of the criteria is simultaneously carried for both the contrast and the currents, whereas, in MR-CSI the criteria is first minimized for the currents and then for the contrast. This simultaneous optimization of the two physically different quantities leads to a problem when optimizing the criteria. This inconvenient is solved by using a preconditioner when computing the descent directions (Barriere *et al.* (2011)), the preconditioner used is the diagonal of the Hessien of the

criteria F, H_W and H_X for the Hessian related to the currents and contrast respectively. The conjugate gradient algorithm requires the computation of the gradient referred to the minimization variable. In our case this includes $\nabla_W F = -G_o^\dagger(y - G_o W) + \lambda(XG_c - I)^\dagger(XE - W)$ and $\nabla_X F = \lambda E^\dagger(XE - W) + \lambda_r D^\dagger DX$. Where $\dagger$ indicates transpose conjugate and D is a tridiagonal matrix that calculates the difference of pixel p with the neighbours in the x and y directions as required by 2.30. Taking all of this into account, the iterative algorithm is summarized in Algorithm 1.

Algorithm 1 AR-CSI algorithm

$g_W \leftarrow \nabla_W$
$g_X \leftarrow \nabla_X$
$P_W \leftarrow H_W^{-1}$
$P_X \leftarrow H_X^{-1}$
$p_W \leftarrow -P_W g_W$
$p_X \leftarrow -P_X g_X$
for $k = 0 \rightarrow n_{itt}$ **do**
  $\alpha \leftarrow \min_{\alpha} F(X + \alpha p_X, W + \alpha p_W)$
  $W \leftarrow W + \alpha p_W$
  $X \leftarrow X + \alpha p_X$
  $g_W^{old} \leftarrow g_W, g_X^{old} \leftarrow g_X,$
  $g_W \leftarrow \nabla_W, g_X \leftarrow \nabla_X$
  $P_W \leftarrow H_W^{-1}, P_X \leftarrow H_X^{-1}$
  $\beta^{PR} \leftarrow \frac{g_W^\dagger(P_W(g_W - g_W^{old})) + g_X^\dagger(P_X(g_X - g_X^{old}))}{g_X^{old\dagger} P_X g_x^{old} + g_W^{old\dagger} P_W g_W^{old}}$
  $p_W \leftarrow -P_W g_W + \beta p_W$
  $p_X \leftarrow -P_X g_X + \beta p_X$
end for

The algorithm starts initializing the descent directions and an iterative process starts until the required condition has been fulfilled, either the decreasing of the gradient or the maximum number of iterations. First, the optimum step α is found by minimization of the criteria $F(X+\alpha p_X, W+\alpha p_W)$, which turns out to be a third degree polynomial in α (Barriere *et al.* (2011)). The optimum value is found by setting $F'(\alpha) = 0$ and finding the roots of the resulting polynomial. The values of X and W are updated using the calculated α value and the descent directions, p_W and p_X. The gradients and the preconditioner are updated and the new descent direction is computed using the Polak-Ribiere formula for β. Finally it should be noted that the CG algorithm is usually defined for real quantities, whereas in our case, both the contrast and the currents are complex quantities. In that case, the complex quantities are replaced by a real value representation (Barriere *et al.* (2011)).

ANNEX B

Mode calculation in a multilayer lossy dielectric waveguide

Dielectric waveguide (DW) analysis is commonly found in most classical electromagnetic books (Balanis (1989)). However, the analysis of multilayer DW with gain and losses is commonly analyzed in optics. The analysis is usually done using the transmission matrix (TxM) method (Schlereth et Tacke (1990)) or the scattering matrix (SM) method (Visser *et al.* (1995)). The TxM method is simpler, however it may become numerically unstable for certain cases (Visser *et al.* (1995)). In our analysis we will use the TxM method since it is easier to implement and it was found to be stable in the particular examples used in this project.

B.1 Transmission matrix method

Here, we will follow the development discussed in (Schlereth et Tacke (1990)). Only the TE case is shown since no major changes are needed for the calculation of the TM case. We have to solve the Helmholtz equation B.1, where wave propagation is taken along the z direction, as it can be seen in figure B.1 and the structure in the x direction is supposed to be infinite. In order to not confuse the terms TE and TM, here these terms are defined referred to the direction of propagation inside the waveguide (i.e. z axis in this case) as it is commonly used in the literature. On the other hand when referring to a 2D scattering problem, TM or TE are defined with respect to the infinite dimension of the object (i.e. x axis in this case).

$$\frac{\partial^2}{\partial y^2} E_{xm}(y,z) - ({k_z}^2 - {k_0}^2 {\varepsilon_m}^2) = E_{xm}(y,z) \tag{B.1}$$

First, a general solution for the electric field is proposed for all the layers (B.2).

$$E_{xm}(y) = A_m e^{\gamma_m (y - y_m)} + B_m e^{-\gamma_m (y - y_m)} \tag{B.2}$$

Where $\gamma_m = \sqrt{{k_z}^2 - {k_0}^2 {\varepsilon_m}^2}$ is the complex propagation constant and A_m are the complex field coefficients in the layer m. Then, boundary conditions are applied along the y direction at each interface for the electric field and its derivative. Developing these two equations and arranging into a matrix formulation, we obtain :

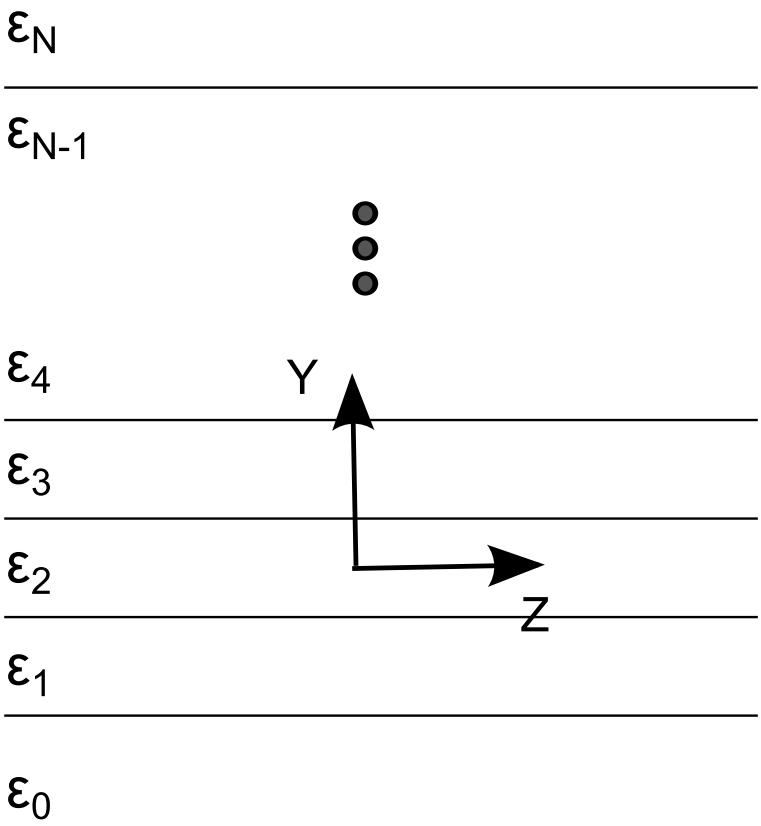

Figure B.1 Schema for the calculation of the modes in a multilayer waveguide

$$\begin{bmatrix} A_{m+1} \\ B_{m+1} \end{bmatrix} = T_m \begin{bmatrix} A_m \\ B_m \end{bmatrix} \tag{B.3}$$

Where T_m represents the transformation of the coefficients between layer m and m+1, which is called the transmission matrix of the waveguide. T_m can be obtained as :

$$T_m = \begin{bmatrix} \frac{e^{\delta_m}}{2}(1+\frac{\gamma_m}{\gamma_{m+1}}) & \frac{e^{-\delta_m}}{2}(1-\frac{\gamma_m}{\gamma_{m+1}}) \\ \frac{e^{\delta_m}}{2}(1-\frac{\gamma_m}{\gamma_{m+1}}) & \frac{e^{-\delta_m}}{2}(1+\frac{\gamma_m}{\gamma_{m+1}}) \end{bmatrix} \tag{B.4}$$

Where $\delta_m = \gamma_m d_m$ and d_m represents the thickness of the m-th layer. The electric field has to be evanescent in the air layers for $x \to \pm\infty$. Hence one of the coefficients in each of the layers has to be zero. Making an appropriate choose of signs, we have that $B_1 = 0$ and $A_N = 0$. Since the two layers are related by $T_{WG} = \prod_{m=1}^{N} T_m$, we can obtain from (B.5) a transcendental equation. From (B.5) we know that $t_{11}A_{11} = 0$ and since $A_{11} \neq 0$, we obtain the transcendental equation $t_{11}(k_z) = 0$.

$$T_{WG}\begin{bmatrix} A_1 \\ 0 \end{bmatrix} = \begin{bmatrix} t_{11} & t_{12} \\ t_{21} & t_{22} \end{bmatrix}\begin{bmatrix} A_1 \\ 0 \end{bmatrix} = \begin{bmatrix} 0 \\ B_N \end{bmatrix} \tag{B.5}$$

Finally, a root-finding algorithm is applied to find the propagating TE modes. The layers have complex permittivity. For this reason the solution algorithm is taken in two steps. First, the lossless case is solved using a standard root-finding algorithm such as bisection or Newton. Then this solution is used as a guess for another root-finding algorithm, Muller's method (Press *et al.* (1988)), which is able to search for a solution in the complex plane.

B.2 Application example

As an example, the case of a glycerin layer (ε_r=6.28, σ=0.43 s/m) is solved. This layer is compressed between two dielectric layers (ε_r=2.56, σ=0.0051 s/m), and the other two layers on top and bottom of those later ones being air. The operation frequency is 2.45 GHz. Air layers are infinite and the thickness of the dielectric layers and the glycerin layer is 6.35mm and 38mm, respectively. The propagation constants of the two propagating modes are shown in table B.1. The position of the roots in the real axis and in the complex plane is shown in figure B.2. Finally a plot of the electric fields inside the waveguide is shown in figure B.3.

Table B.1 Propagation constants of the TE modes in glycerine.

	α	β
TE_0	273dB/m	81.31 rad/m
TE_1	279dB/m	120.57 rad/m

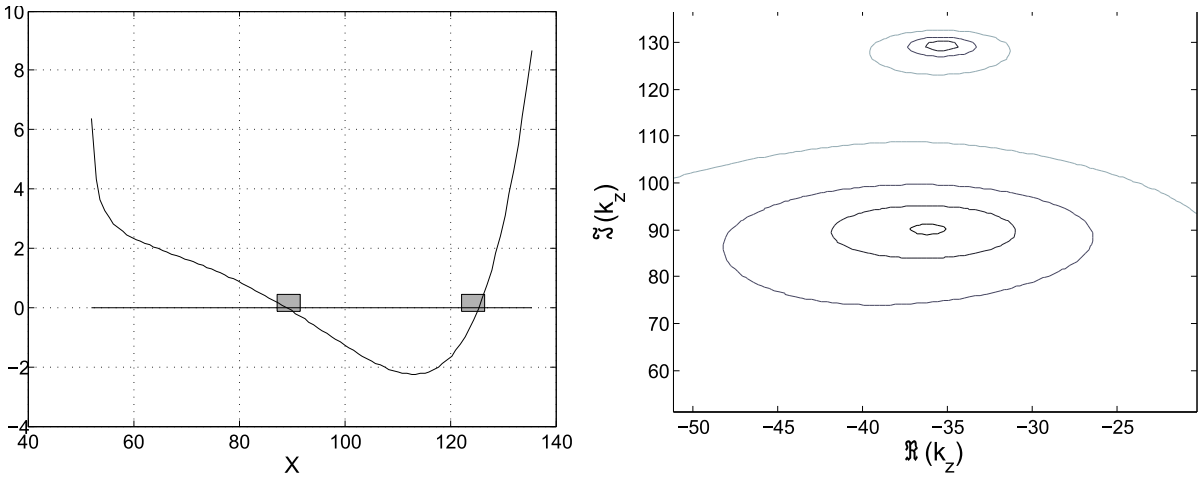

(a) (b)

Figure B.2 Root position in the real axis (a) and in the complex plane (b)

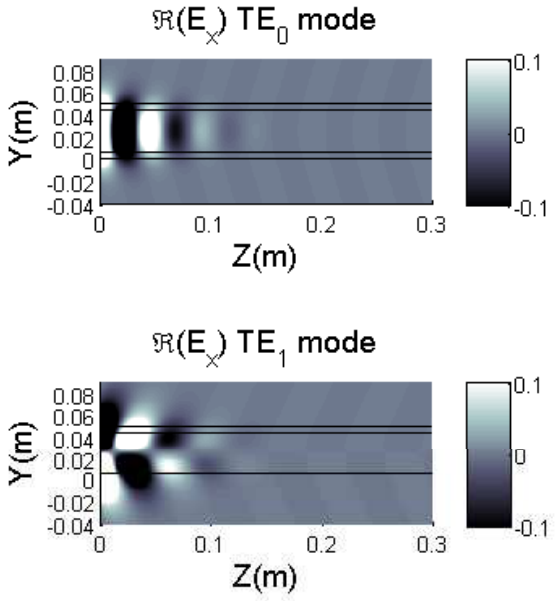

Figure B.3 Fields computed using the transmission matrix approach for a glycerine slab.